공학박사학위논문

장수거북의 종방향 릿지:
유체역학적 역할과 컨셉카 디자인 응용

Longitudinal ridges on a leatherback turtle: hydrodynamic role and application to concept-car design

2017 년 8 월

서울대학교 대학원

기계항공공학부

방 경 태

장수거북의 종방향 릿지:
유체역학적 역할과 컨셉카 디자인 응용

Longitudinal ridges on a leatherback turtle: hydrodynamic role and application to concept-car design

지도교수 최 해 천

이 논문을 공학박사 학위논문으로 제출함

2017 년 7 월

서울대학교 대학원

기계항공공학부

방 경 태

방경태의 공학박사 학위논문을 인준함

2017 년 7 월

위 원 장 : 김 호 영

부위원장 : 최 해 천

위 원 : 방 현 민

위 원 : 최 정 암

위 원 : 김 대 겸

Longitudinal ridges on a leatherback turtle: hydrodynamic role and application to concept-car design

Kyeongtae Bang
Department of Mechanical & Aerospace Engineering
Seoul National University

Abstract

Leatherback sea turtles (*Dermochelys coriacea*) are known to have a superior diving ability and be highly adapted to pelagic swimming. They have five longitudinal ridges on their carapace and these ridges are one of remarkable morphological features distinguished from other marine turtles. Although it was conjectured that these ridges might be an adaptation for flow control, no rigorous study has been performed to understand their hydrodynamic roles.

Therefore, to elucidate the hydrodynamic role of these ridges in the leatherback turtle swimming, in Part I, I model a carapace with and without the ridges by using three dimensional surface data of a stuffed leatherback turtle in the National Science Museum, Korea. The experiment is conducted in a wind tunnel in the ranges of the real leatherback turtle's Reynolds number (Re) and angle of attack (α). The ridges are slightly misaligned to the streamlines around the body to generate streamwise vortices, and suppress flow separation on the carapace, resulting in enhanced hydrodynamic performances during different modes of swimming. At high negative angles of attack and relatively low swimming

speed corresponding to a vigorous swimming condition of hatchlings, the ridges significantly decrease the drag and increase the lift. At high positive angles of attack and relatively high swimming speed that represents the conditions of ascending swimming of adults, the ridges enhance the lift and lift-to-drag ratio while increasing the drag. This study is the first experimental demonstration that the longitudinal ridges on the carapace of leatherback sea turtle, which are locally misaligned to the streamlines around the body, suppress flow separation on the carapace by generating streamwise vortices. These results suggest that shapes of some morphological features of living creatures, like the longitudinal ridges of the leatherback turtles, need not be streamlined for excellent hydro- or aerodynamic performances, contrary to our common physical intuition.

From this conceptual approach, in Part II, I develop a newly-designed concept car model which has the longitudinal ridges on the surface and investigate the aerodynamic performance of the concept model. At zero yaw angle, the drag coefficient of the concept model is about 5% lower than that of the base model (Hyundai motors). To understand the effect of side wind on the aerodynamic characteristics of the model, I also consider non-zero yaw angles (γ=0°-30°) and measure the drag and side forces. At non-zero yaw angles, the drag coefficient on the concept model is lower by upto 13% than that of the base model, and the side force coefficient on the concept model is lower by upto 20% compared to that of the base model. These results support that, unless the yaw angle is very large, the aerodynamic effects of the concept design in terms of drag and side forces are still similar to those of zero yaw angle. Flow-field analysis shows that the ridges on the concept model generate streamwise vortices, and suppress flow separation on the rear slanted surface, resulting in the drag reduction of

the concept model.

Keywords: leatherback turtle, ridge, streamwise vortex, hydrodynamics, bio-mimetic flow control, concept car, lift, drag

Student number: 2011-22888

Contents

List of Figures

Part I. Hydrodynamic role of longitudinal ridges in a leatherback turtle swimming

Figure

Part II. Development of a bio-mimetic concept car design with low aerodynamic drag

Figure

Nomenclature

Roman Symbols

A_f	frontal area of the model
A_p	planform area of the model
B	buoyancy force
C_D	drag coefficient
C_L	lift coefficient
C_S	side force coefficient
D	drag force
F_h	horizontal force
F_v	vertical force
g	gravitational acceleration
h	height of the model
L	lift force
l	length of the model
m	body mass
Re	Reynolds number
Re_h	Reynolds number based on the model height
u	streamwise velocity
U_0	free-stream velocity
V_O	body volume
v	vertical velocity
w	spanwise velocity
x, y, z	cartesian coordinate with the origin at the center of the model

	trailing edge
	in Part I
	Cartesian coordinate with the origin at the center of the front edge
	in Part II

Greek Symbols

α	angle of attack
γ	yaw angle
Δ	variation rate
θ	pitching angle
ν	kinematic viscosity
ν_{sea}	kinematic viscosity of sea water
ρ	density of air
ρ	density of sea water
ω_x	streamwise vorticity
ω_z	spanwise vorticity

Abbreviations

DPIV	digital particle image velocimetry
FoV	field of view

Part I

Hydrodynamic role of longitudinal ridges in a leatherback turtle swimming

Chapter 1

Introduction

Leatherback sea turtles (*Dermochelys coriacea*) are known as the largest and heaviest turtle in the earth (Figure 1.1). Despite of their enormous body size, (Figure 1.2) shows that leatherback sea turtles are also known as the fastest swimmer and the deepest diver among marine turtles therefore they are known to have superior diving ability (Lutcavage & Lutz, 1996; Hays, Houghton & Myers, 2004; Reina *et al.*, 2005). They are also known for long-distance migration (Figure 1.3) and considered to be highly adapted to pelagic swimming (Keinath & Musick, 1993; Hays, Houghton & Myers, 2004; Fossette *et al.*, 2010; Block *et al.*, 2011; Shillinger *et al.*, 2011). On the body of leatherback turtles, there are a few remarkable morphological features such as soft carapace, big flippers, and longitudinal carapace ridges that distinguish them from other marine turtles (Eckert *et al.*, 1989). Among these, five longitudinal ridges on their carapace are a notable feature (Figure 1.4). Some conjectured that these ridges represent an evolutionary adaptation for keeping the flow around the body laminar (Deraniyagala, 1936; Hendrickson, 1980). However, no study has been made for their hydrodynamic roles yet. Some of natures morphological features have been shown to provide better aero- and hydrodynamic performances. For example, dorsal and ventral keels of a boxfish generate streamwise vortices, and these vortices are considered to increase the hydrodynamic stability (Bartol *et al.*, 2002, 2003, 2008); tubercles on the leading edge of a humpback whales flipper increase

the lift by generating streamwise vortices and delaying separation (Miklosovic *et al.*, 2004; Fish & Lauder, 2006; Pedro & Kobayashi, 2008); an alula on the leading edge of a birds wing produces a streamwise vortex and increases the lift (Lee *et al.*, 2015); a serrated leading edge of an owls feather also produces streamwise vortices to fly silently (Anders, 2000; Choi *et al.*, 2012); spade-like protrusions on the trailing edge of a dragonfly wing provide an idea for reducing drag on an airfoil with a gurney flap (Bechert, Meyer & Hage, 2000). All of these morphological features are located on the leading edges of the wing and flipper, on the frontal part of the body, and on the trailing edge of the wing. Unlike these morphological features, the longitudinal ridges of a leatherback sea turtle are located along the entire body. In this respect, the hydrodynamic roles of ridges in leatherback turtles swimming should be interesting to investigate. Therefore, in the present study, I investigate their hydrodynamic roles in the conditions that represent the swimming modes of hatchling and adult leatherback turtles.

Prior to investigating the effect of the longitudinal ridges in the leatherback turtles' ecological point of view, it is first necessary to know the behavioral characteristics of leatherback turtles with respect to their stages of growth. Therefore, in Sec. 1.1, diving behaviors of adult leatherback turtles is briefly reviewed and I describe typical diving characteristics and major hydrodynamic issue of adults. In Sec. 1.2, some previous studies about the swimming patterns of hatchling leatherback turtles and I describe representative swimming characteristics and major hydrodynamic issues in hatchlings' swimming. The objectives of this dissertation are given in Sec. 1.3

1.1 Behavioral characteristics of adult leatherback turtles

The diving patterns of leatherback turtles are divided into the V-shaped diving, U-shaped diving, and sub-surface swimming according to the shapes of the diving profile (Eckert, 2002; Reina *et al.*, 2005; Casey *et al.*, 2010; Fossette *et al.*, 2010) (see, for example, Figure 1.5). The V-shaped diving, used for foraging and transit, is a typical diving pattern of adult leatherback turtles(Eckert, 2002; Reina *et al.*, 2005; Casey *et al.*, 2010; Fossette *et al.*, 2010). Breath-hold divers such as leatherback turtles have no buoyancy-control organ and thus experience negative buoyancy in deep water due to the compression of pulmonary air by water pressure (Davis & Weihs, 2007; Fossette *et al.*, 2010). This negative buoyancy enables diving, so their descending swim can be largely energy-efficient (Davis & Weihs, 2007; Fossette *et al.*, 2010). In contrast, they have to actively swim up at high pitch angles (or high angles of attack) during the ascending period to overcome the negative buoyancy (Fossette *et al.*, 2010). Therefore, the hydrodynamic performance in ascending swimming conditions at positive angles of attack can be energetically important for the leatherback turtles.

1.2 Behavioral characteristics of hatchling leatherback turtles

On the other hand, hatchling or juvenile leatherback turtles cannot dive as deep as adults since they cannot hold their breath for a long time due to the low tissue volume for oxygen storage and high mass-specific metabolic rates (Wyneken & Salmon, 1992; Salmon, Jones & Horch, 2004). Therefore, hatchlings swim mainly in shallow water (Salmon, Jones & Horch, 2004). Their swimming patterns are divided into a routine swimming (slow) near the water surface and a vigorous swimming (fast and large energy consuming) underwa-

ter (Davenport, 1987) (see, for example, Figure 1.6). The vigorous swimming is important for hatchlings as it provides a means to overcome positive buoyancy and escape from predators (Davenport, 1987; Bjorndal, Bolten & Chaloupka, 2003). Therefore, the hydrodynamic characteristics during the vigorous swimming (swimming at large negative angles of attack) should also be considered to fully understand the roles of the longitudinal ridges.

1.3 Objectives

The main objectives of the present study are to investigate the hydrodynamic role of longitudinal dorsal ridges in a leatherback turtle swimming and reveal the mechanisms responsible for improvement in hydrodynamic performances of both hatchlings and adults. For these purposes, I constructed carapace models of a leatherback turtle with and without the longitudinal ridges based on a geometric information of a stuffed leatherback turtle at National Science Museum, Daejeon, Korea, and the drag and lift forces on both models are directly measured by varying the Reynolds number and angle of attack. The flow fields near the models are observed using oil-surface visualization and DPIV (Digital particle image velocimetry).

This paper is organized as follows. In Chapter 2, details on the experimental set-up for the force measurement, flow visualization and DPIV measurement are described. In Chapter 3, experimental results of the hydrodynamic role of the ridges with respect to each swimming mode of hatchlings and adults are given and discussed. Investigation about the modifications of flow structures by the ridges are also discussed here. Finally, the summary and concluding remarks are followed in Chapter 4.

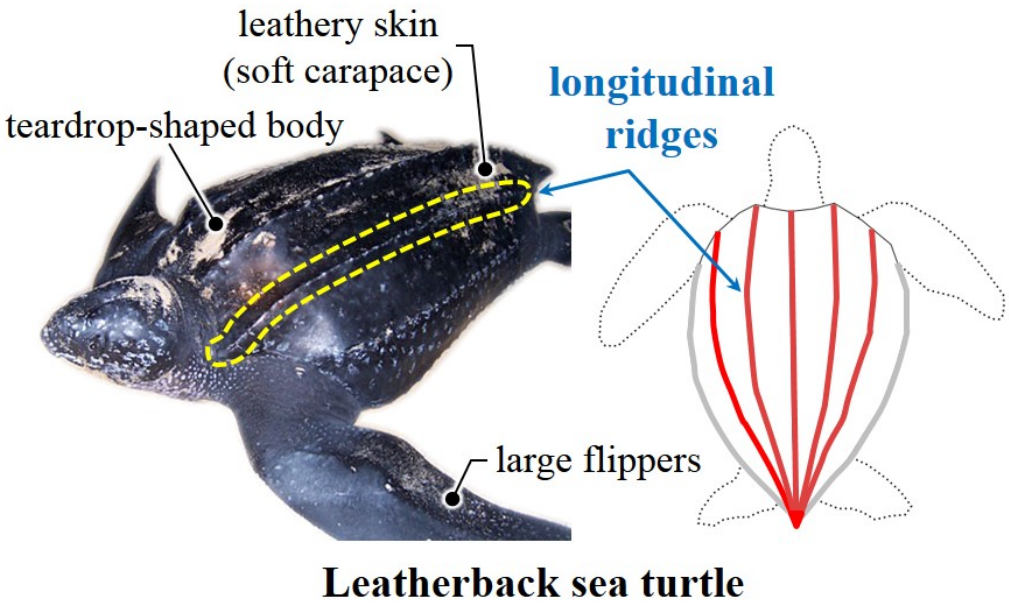

Figure 1.1. Morphological characteristics and longitudinal dorsal ridges of a leatherback sea turtle.

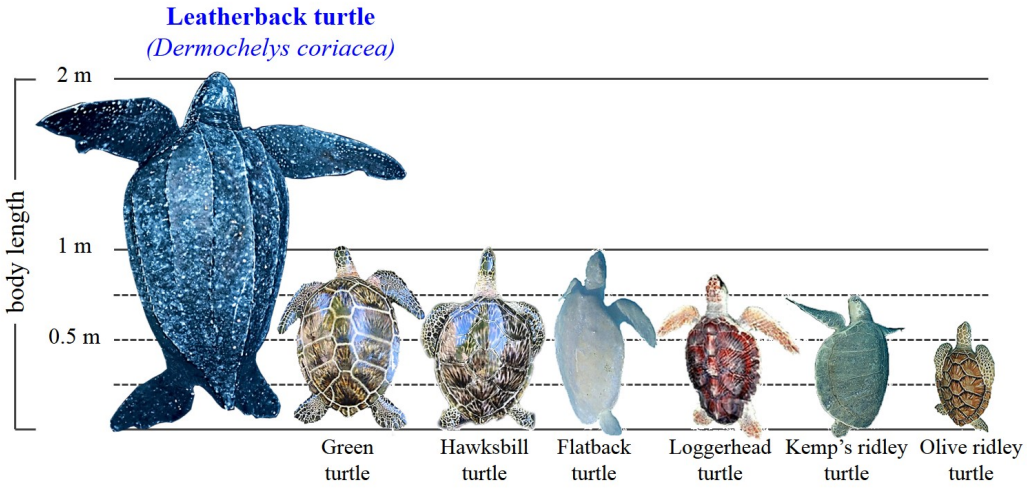

Figure 1.2. Averaged body length of various sea turtles.

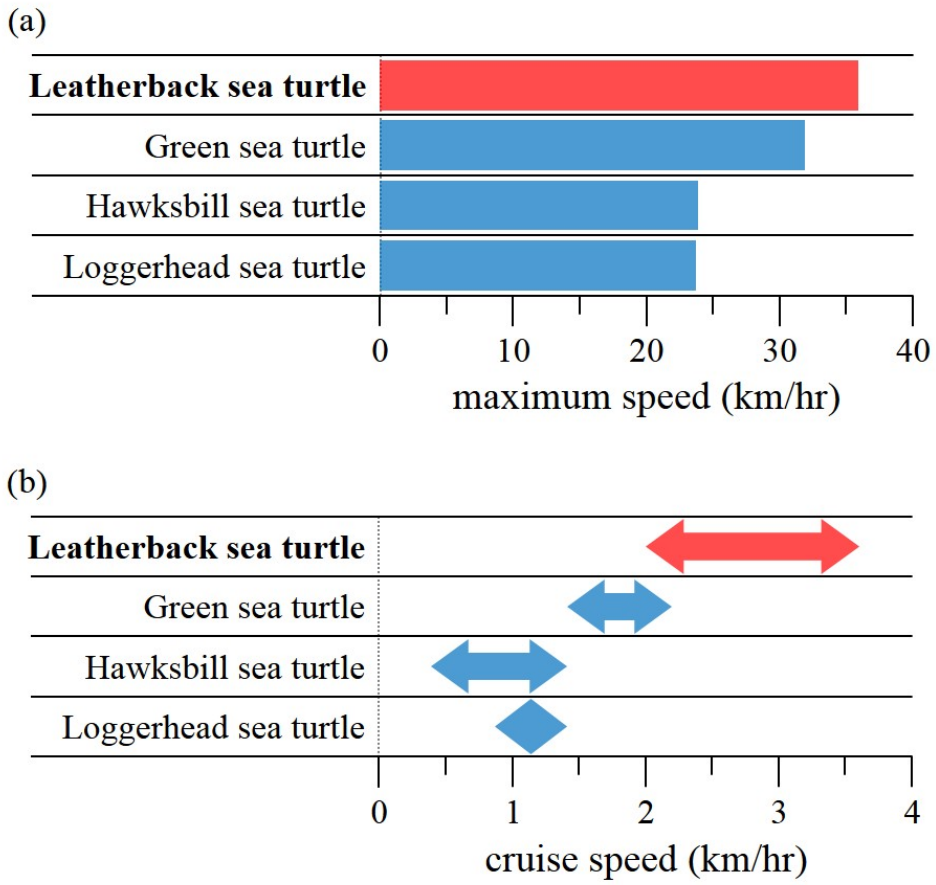

Figure 1.3. (a) Maximum swimming speed of sea turtles (b) Cruise swimming speed variations of sea turtles.

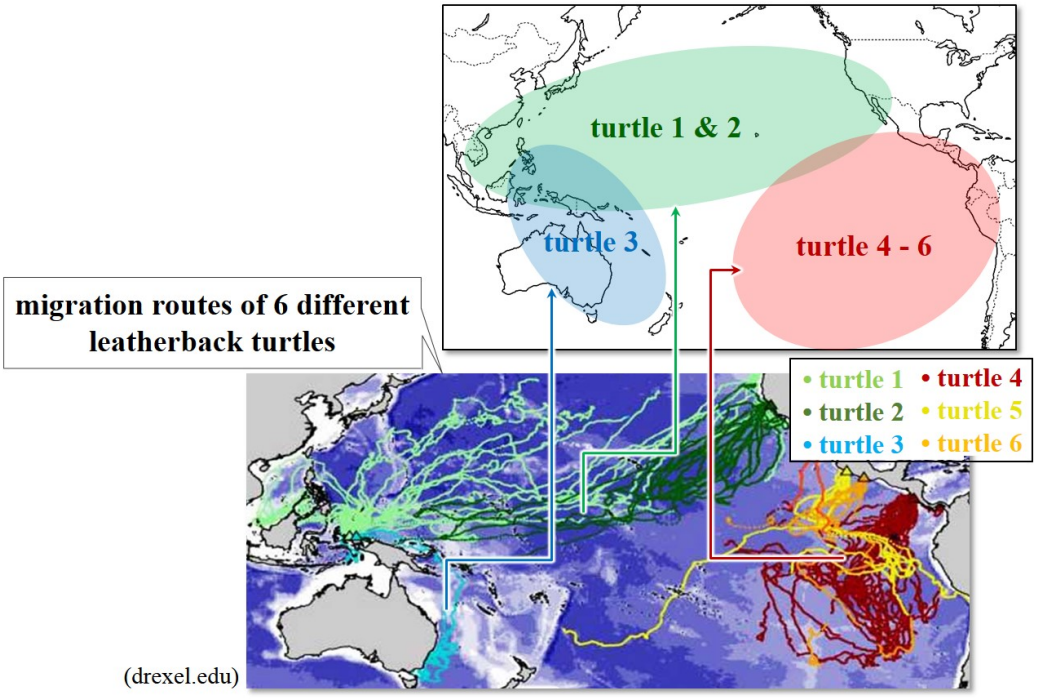

Figure 1.4. Migration routes of leatherback sea turtles.

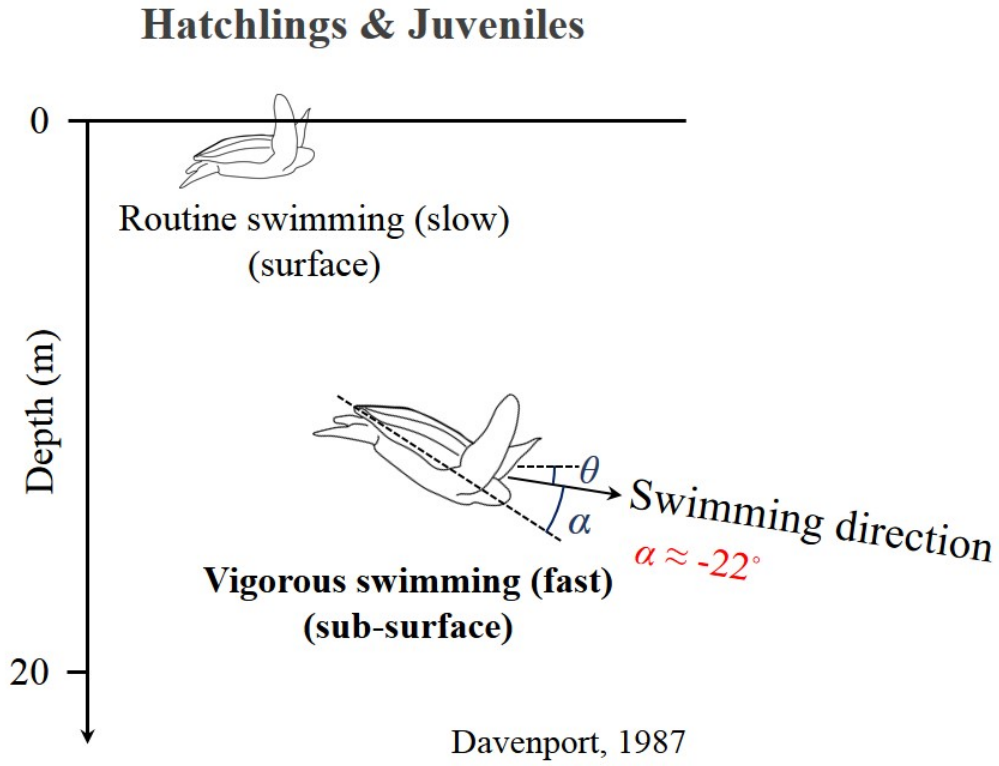

Figure 1.5. Schematic diagram of swimming patterns of hatchling leatherback turtles (Davenport, 1987).

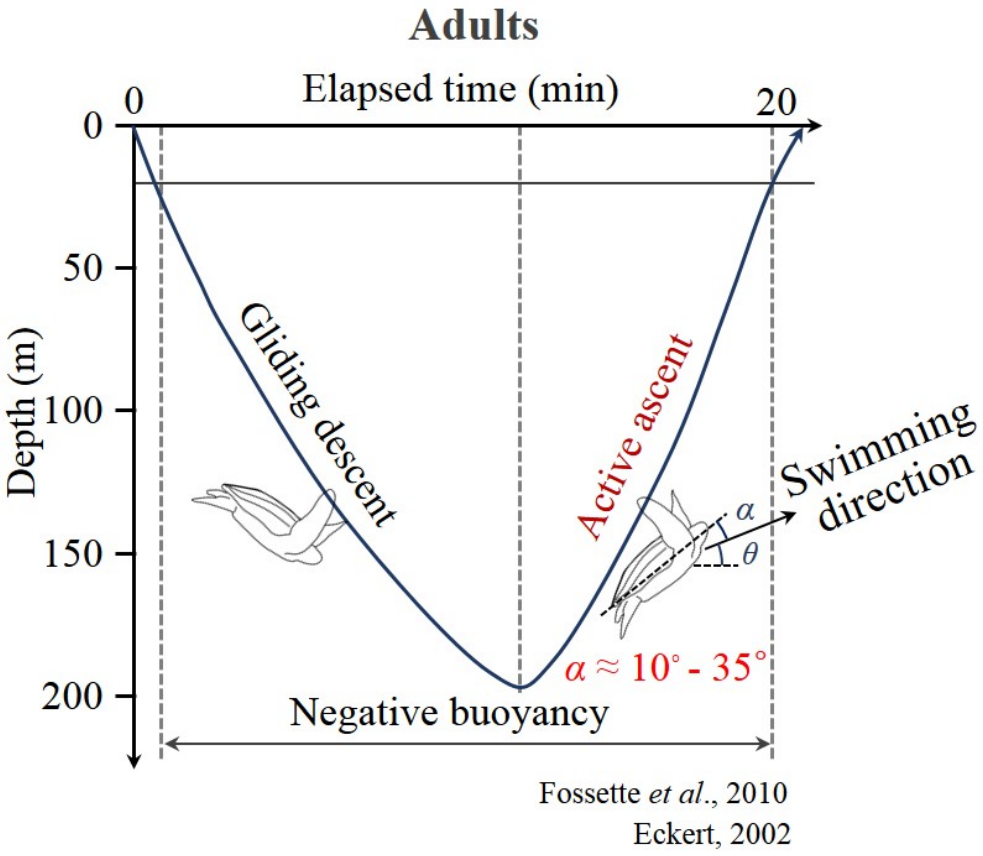

Figure 1.6. Schematic diagram of diving patterns of adult leatherback turtles (Fossette *et al.*, 2010).

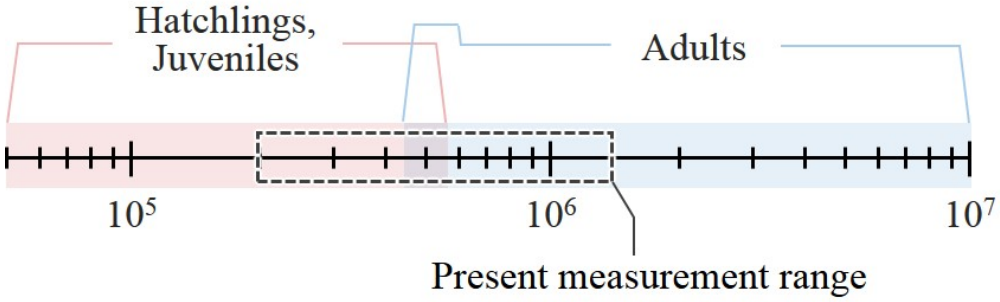

Figure 1.7. Variation of the Reynolds number in leatherback turtle swimming based on the carapace length and different stages of growth. Carapace length of hatchlings is about 24 cm at $Re = 2 \times 10^5$ (Davenport, 1987) and carapace length of adults is about 1 m at $Re = 5 \times 10^5$ (Eckert, 2002). The present measurement range is drawn in dashed gray line.

Chapter 2

Experimental Set-up

To investigate the hydrodynamic role of the longitudinal ridges of a leatherback turtle, a carapace model is constructed based on a three-dimensional surface data of a stuffed leatherback turtle. The three-dimensional forces on both models are directly measured using three force sensors. The flow fields near both models are obtained using a oil-surface visualization method and a DPIV (Digital particle image velocimetry). Sec. 2.1 gives an account of how the leatherback turtle models with and without the ridges are constructed. The experimental set-up for the force measurement and the measurement accuracy are discussed in Sec. 2.2. Detailed descriptions of the oil-surface visualization and the DPIV system are followed in Sec. 2.3. and Sec 2.4, respectively.

2.1 Leatherback turtle models

I constructed a carapace model based on three-dimensional surface data obtained by scanning a stuffed leatherback turtle (carapace length of 1.2 m, adult) at National Science Museum, Daejeon, Korea (Figure 2.1). According to previous observations, leatherback turtles have a relatively narrow range of motion in their neck and thus their head does not noticeably move relative to the carapace during swimming (Davenport, 1987; Oliver *et al.*, 2000). As for fore flippers, leatherback turtles show only synchronous flapping during linear

progression (Renous, Bels & Davenport, 2000; Wyneken, 1996). For this reason, I assumed that the motions of head and flippers do not noticeably affect the flow near the carapace, and thus we eliminated the head and limb parts in the process of constructing a carapace model. The carapace model was constructed such that its shape was similar to the body shape of the stuffed leatherback turtle. First, we measured the profile of the longitudinal ridge at the center ($z = 0$) of the stuffed leatherback turtle, and obtained a smooth profile of the ridge by applying a least square method based on 8^{th}-order polynomials,

$$\begin{aligned} f(x) = &- (1.063883 \times 10^{-17})x^8 + (2.29149 \times 10^{-14})x^7 - (2.01994 \times 10^{-11})x^6 \\ &+ (9.4706 \times 10^{-9})x^5 - (2.57744 \times 10^{-6})x^4 + (4.16672 \times 10^{-4})x^3 \\ &- (4.02333 \times 10^{-2})x^2 + 2.330198x + 8.43726 \end{aligned} \tag{2.1}$$

where $0 \leq x \leq 400$. The spanwise edge of the carapace was located at $g(x) = 1.5029f(x)$ (see Figure 2.2).

The upper surface of the carapace model was divided by three parts in the streamwise direction: $0 \leq x \leq 40$, $40 < x < 80$, $80 \leq x \leq 400$, the carapace has three curved surfaces in the spanwise direction because of the ridges (Figure 2.2(b)), and thus each surface was modeled using a least square method based on 5^{th}-order polynomials:

$$\begin{aligned} y(x,z)/f(x) =& 5.4413(z/f(x))^5 - 8.192(z/f(x))^4 + 3.2192(z/f(x))^3 \\ &+ 0.90984(z/f(x))^2 - 0.805812(z/f(x)) + 1, \\ &for 0 \leq z/f(x) \leq 0.6595 \end{aligned} \tag{2.2}$$

$$
\begin{aligned}
y(x,z)/f(x) = &-9.06338(z/f(x))^5 + 47.32(z/f(x))^4 - 97.136(z/f(x))^3 \\
&+ 98.2152(z/f(x))^2 - 49.6478(z/f(x)) + 10.9469, \\
&for 0.6595 < z/f(x) \leq 1.2511
\end{aligned}
\tag{2.3}
$$

$$
\begin{aligned}
y(x,z)/f(x) = &-3284.22(z/f(x))^5 + 22372.098(z/f(x))^4 - 60931.94(z/f(x))^3 \\
&+ 82938.25(z/f(x))^2 - 56421.49(z/f(x)) + 15347.283, \\
&for 1.2511 < z/f(x) \leq 1.5029
\end{aligned}
\tag{2.4}
$$

For $0 \leq x \leq 40$, a smooth surface without the ridges was constructed using an ellipse following the body shape of the stuffed leatherback turtle:

$$
\begin{aligned}
y(x,z)/f(x) = &0.8925\sqrt{1 - 0.44275(z/f(x))^2} \\
&for 0 \leq z/f(x) \leq 1.5029
\end{aligned}
\tag{2.5}
$$

For $40 < x < 80$, a surface shape of the carapace from smooth (y_2, z_2) to curved (y_1, z_1) surface was constructed using a weighting factor between these two surfaces:

$$
\begin{aligned}
y &= y_2 + (y_1 - y_2)\log_2 \frac{x}{40} \\
z &= z_2 + (z_1 - z_2)\log_2 \frac{x}{40}
\end{aligned}
\tag{2.6}
$$

Here, (y_1, z_1) was first obtained for $40 < x < 80$ using Eq. (2.3-2.5), and then (y_2, z_2) was obtained from

$$
\begin{aligned}
y_1/f(x) =& 0.8925(1-0.44275(z_2/f(x))^2)^{1/2}(1-2.8355\frac{z_2/f(x)-z_1/f(x)}{z_2/f(x)} \\
y_2/f(x) =& 0.8925\sqrt{1-0.44275(z_2/f(x))^2}
\end{aligned}
\tag{2.7}
$$

The lower surface of the stuffed leatherback turtle was modeled using an ellipse:

$$
\begin{aligned}
y(x,z)/f(x) =& -0.5\sqrt{1-0.44275(z/f(x))^2} \\
& for 0 \leq x \leq 400, 0 \leq z/(f(x) \leq 1.5029
\end{aligned}
\tag{2.8}
$$

As I show in this paper, I observe that a separation bubble exists in the front part of the carapace surface at the swimming mode of active ascent (Figure 3.20, 21). Therefore, I made another set of carapace models including the head part by scanning a leatherback turtles head (Figure 2.9), to see how the head affects the flow over the carapace. The length of the carapace model (l) was 400 mm, which was 1/3 scale of the carapace of the stuffed leatherback turtle. We also constructed a carapace model without the ridges (i.e. smooth surface model) for comparison by keeping the frontal (A_f) and planform (A_p) areas the same as those of the model with the ridges. In my analysis, I also assumed that hatchlings and adults are geometrically similar (Prange, 1976). Thus, I used same carapace models to investigate the hydrodynamic roles of the ridges for different swimming modes of both hatchlings and adults, although the present carapace models were constructed from the geometric information of an adult leatherback turtle.

2.2 Force measurements

The lift (L) and drag (D) forces on the carapace models with and without the ridges were measured in a wind tunnel. Various Reynolds numbers (Re) and angles of attack (α) were chosen considering the swimming conditions of both hatchling and adult leatherback turtles (Figure 1.5, 1.6). The angles of attack (angle between the swimming direction and the body alignment) considered were -22° $-$ 22°, and the Reynolds numbers ($Re = U_0 l/\nu$) were 0.2 1.2 $\times$ 10^6, where U_0 is the free-stream velocity, l is the model length, and ν is the kinematic viscosity of air. The lift (L), drag (D) and side (S) forces on both models were measured simultaneously with three load cells (A&D LCB03-015M for the lift force and A&D LCB03-006M for the drag force and A&D LCB03-003M for the side force) (Figure 2.7). Resolutions of these three load cells were 0.015 N 0.006 N and 0.003 N with maximum capacities of 150 N, 60 N and 30 N, respectively. The signals from these load cells were digitized by an A/D converter (PXI-6259, National Instruments Co.) and sampled for 60 s at a rate of 10 kHz to obtain the mean value. The repeatability errors of force measurements were within 2%. The lift (C_L) and drag (C_D) coefficients were defined as $C_L = L/(0.5\rho U_0^2 A_p)$, $C_D = D/(0.5\rho U_0^2 A_p)$, $C_S = S/(0.5\rho U_0^2 A_p)$ respectively, where ρ is the air density, and A_p is the planform area of the model at $\alpha = 0°$. The carapace model was fixed using a strut which was directly mounted to the load cells (Figure 2.5). The wind tunnel used was a closed-type wind tunnel (Gottingen type) whose test section size was 900 mm $\times$ 900 mm. The blockage ratios due to the model were about 2.6% and 4.1% for $\alpha = 0°$ and $\alpha = 22°$, respectively. To minimize the disturbance from the strut, its cross-section was designed to be an ellipse with a ratio of major to minor axis of 2. The height of the strut was adjusted to locate the carapace model at the center

of the wind tunnel. The force on the isolated strut was measured separately and used for correction from those measured with the model. In the presence of ocean current or during turning motion of a turtle, the swimming direction does not coincide with the freestream direction. This effect was examined by considering the yaw angle (γ) as shown in Figure 2.5. For non-zero γs, we measured the side forces in addition to the drag and lift forces.

2.3 Oil-surface visualization

In order to obtain qualitative flow features such as the separation of the boundary layer and streamlines on the model surface, the oil-surface visualization is performed. The wind tunnel used in the experiment is a closed-type wind tunnel that has the cross-section of 900 mm $\times$ 900 mm after contraction (see Figure 2.6 for details) and the turbulence intensity is lower than 0.5% at the free-stream velocity of 10 m/s. The blockage ratios of the cross-sectional area of both models to the test-section area are about 2.6% and 4.1% for α= 0° and α = 22° respectively, which are below the critical value ensuring negligible blockage effect on the flow field (Achenbach, 1974). The oil used for visualization is made by mixing lamp oil and soybean oil and a dash of titanium dioxide is added to make the oil white. A digital camera (Nikon D7100), whose frame rate is 60 fps at a resolution of 1920 $\times$ 1080 pixels, is used to capture the resulting flow field.

2.4 Digital particle image velocimetry

I used a digital particle image velocimetry (DPIV) to obtain the velocity and vorticity fields around the carapace models with and without the ridges. The measurements were performed for two cases, α = -22° and $Re = 2 \times 10^5$, and α

$= 18^\circ$ and $Re = 5\ 10^5$, which represent the vigorous swimming of hatchlings and the active ascending swimming of adults, respectively. The same wind tunnel used for force measurements was used. The schematic diagram for DPIV is shown in Figure 2.8. The DPIV system consisted of an Nd:Yag laser (Dual Power 135-15, Litron), a laser optics (Short Mirror Arm, Dantec Dynamics), a pulse generator (IDT USB Timing Hub XS-TH, Integrated Design Tools), a fog generator (F2010, Safex), and a CCD camera mounted with an optical lens (APO MACRO 180mm F2.8, SIGMA). A thickness of a laser sheet generated by the laser optics was about 2 mm. The fog generator produced liquid droplets which were spread inside the wind tunnel and their mean diameter was about 1 μm. The velocity measurements were performed on various planes parallel to the $x - y$ and $y - z$ planes, respectively, where x, y, and z denote the streamwise, vertical, and spanwise directions, respectively, and the origin was located at the center of rear edge of the model. To obtain the velocity field from recorded images, an iterative cross-correlation analysis was performed with an initial window size of 64 $\times$ 64 pixels and a final interrogation window size of 16 $\times$ 16 pixels. The interrogation window was overlapped by 50%, leading to spatial resolutions of about 0.15 mm ($3.75 \times 10^{-4}\ l$) on $x - y$ planes and 0.23 mm ($5.75 \times 10^{-4}\ l$) on $y - z$ planes, where l is the model length. To obtain the time-averaged flow field, 2,000 pairs of images were collected and processed.

Figure 2.1. A stuffed leatherback turtle in National science museum, Daejeon, Korea which is used for three-dimensional surface measurement.

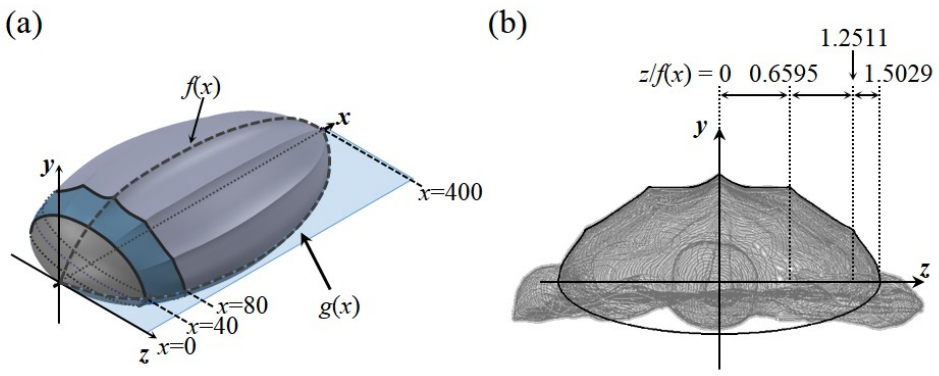

Figure 2.2. Construction of the carapace model. (a) Perspective view; (b) Cross-sectional view.

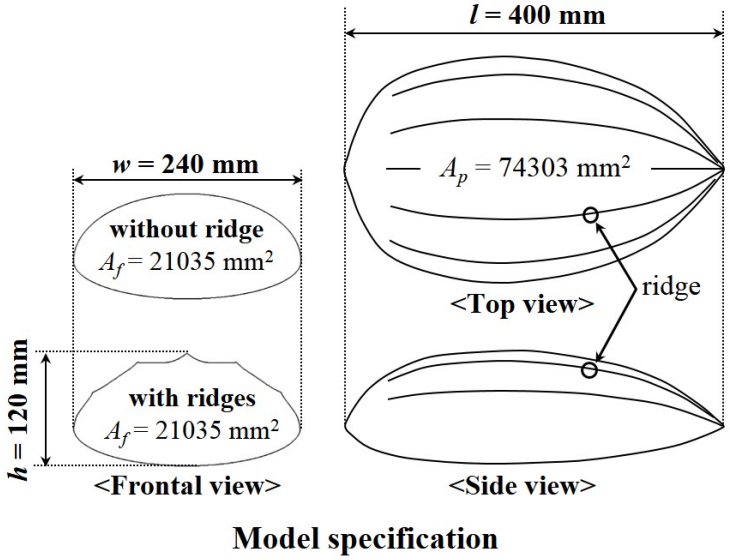

Figure 2.3. Carapace model specification. Characteristic lengths and areas of the carapace models.

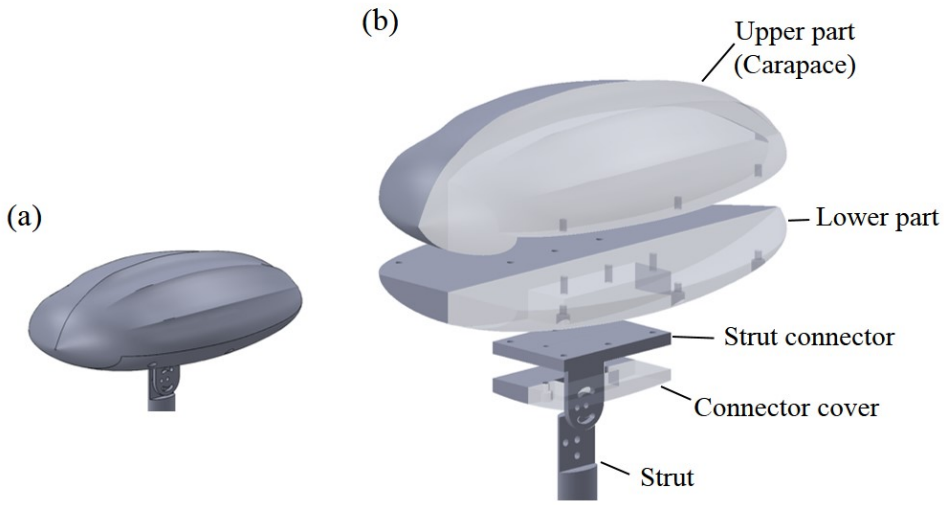

Figure 2.4. (a) Three dimensional drawing of the carapace model; (b) Assembly diagram of the carapace model. Note that the model body is illustrated transparently for clarity.

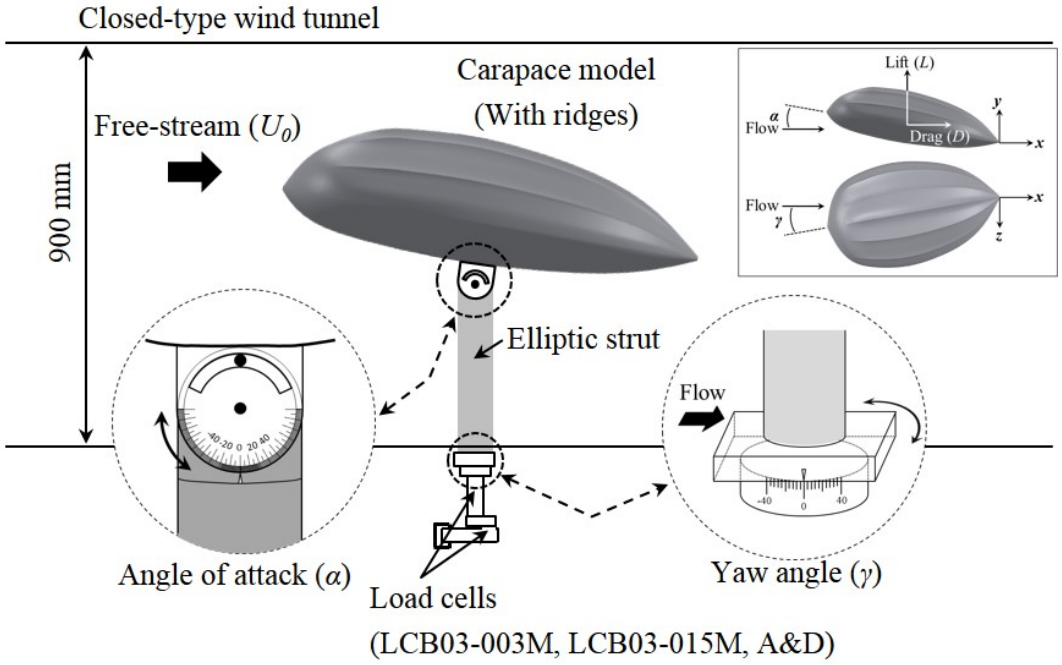

Figure 2.5. Schematic diagram of the experimental set-up for the force measurement. Here, L, D, and S denote the lift, drag, and side forces, respectively, and γ is the yaw angle.

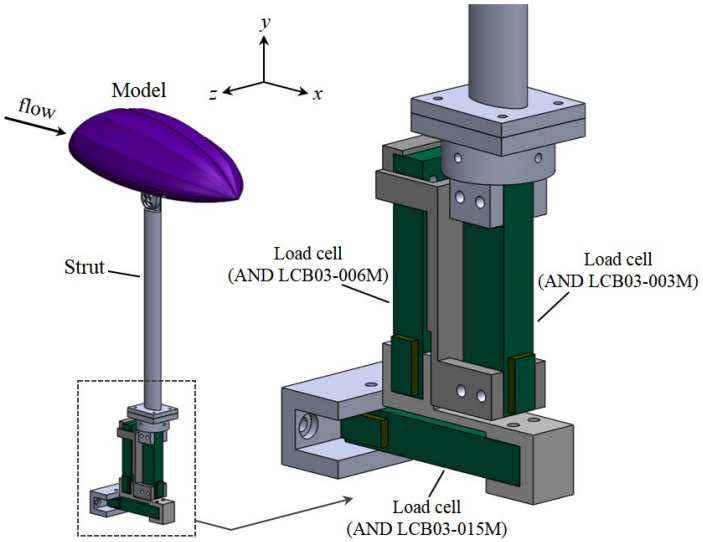

Figure 2.6. Detailed drawing of the force measurement system.

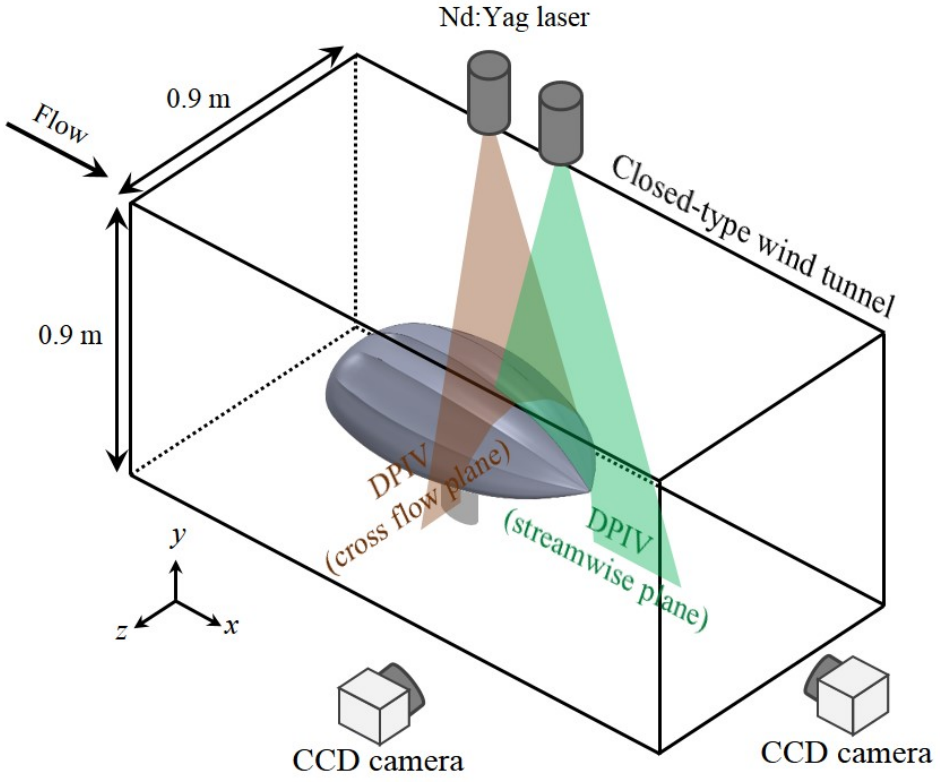

Figure 2.7. Schematic diagram of the experimental set-up for the velocity measurement with DPIV.

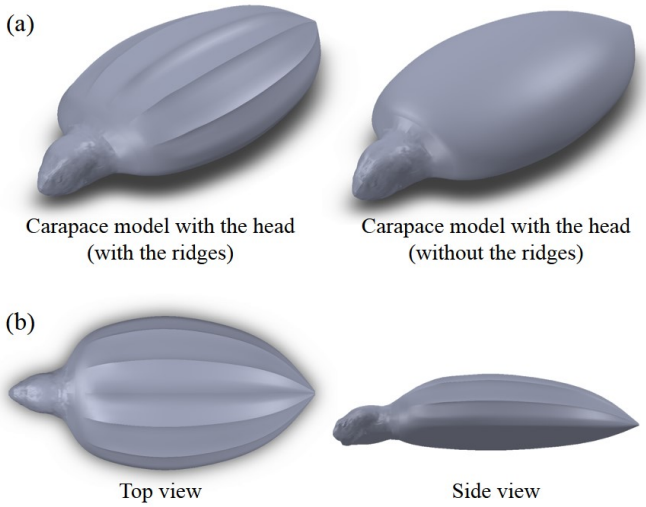

Figure 2.8. Carapace models with the head. (a) Perspective view; (b) Top and side views. The shape of the head was constructed based on the three-dimensional surface data of a stuffed leatherback turtle.

Chapter 3

Results and Discussion

I conducted a series of wind tunnel tests to measure the drag and lift forces on the models with and without the ridges (see Experimental Set-up (Force measurements) and Figure 2.5 for detailed setup). The Reynolds numbers considered were $Re = 0.2 \;\; 1.2 \times 10^6$ (based on the body length l of each model) with varying the angle of attack from α = -22° to 22°. These Re and α ranges include swimming conditions of hatchling and adult leatherback turtles (Figure 1.5, 1.6). I also considered non-zero yaw angles for γ = -22° and 18°, and measured the side forces (Figure 2.5).

3.1 Lift and drag variations

Figure 3.1-3.6 shows the variations of the drag and lift coefficients (C_D and C_L, respectively; see Experimental Set-up (Force measurements) for their definitions), and lift-to-drag ratio (L/D) depending on the angles of attack (α) and the Reynolds numbers (Re). These figure demonstrates two noticeable hydrodynamic roles of the ridges. First, the ridges significantly reduce the drag and also reduce the negative lift at negative to near zero angles of attack (Figure 3.1, 3.2). Especially, at low Reynolds numbers, the drag is reduced by up to 32% at α = -18° (Figure 3.4). In the vigorous swimming, hatchling leatherback turtles adopt a head down/tail up posture at which the attack angle of the body

is about -22° (Davenport, 1987). At this large negative angles of attack, the drag is large and the lift is negative (as shown in Figure 3.4,3.5). Our results suggest that the ridges reduce this high drag force generated during the vigorous swimming of hatchlings.

Second, at positive high angles of attack, the ridges increase both the drag and lift forces, and the lift-to-drag ratio (Figure 3.1-3.3). Especially, at relatively high Reynolds numbers, the lift coefficient and lift-to-drag ratio increase by up to 16% and 7%, respectively, whereas the drag coefficient increases by 5.6% (Figure 3.4-3.6).

3.2 Importance of the hydrodynamic force variations for hatchlings

Let me estimate the importance of these drag and negative-lift reductions (Figure 3.4,3.5) for a hatchling leatherback turtle during the vigorous swimming. At $Re = U_O l/\nu = 2 \times 10^5$, the swimming speed ($U_O$) and body length ($l$) of a hatchling leatherback turtle are obtained to be $U_O = 0.783$ m/s (3.3 l/s) (Davenport, 1987) and $l = 23.8$ cm (the shortest body length of a hatchling leatherback turtle is known to be 9 cm (Davenport, 1987)), where the kinematic viscosity of sea water is $\nu_s ea = 0.932 \ \ 10^{-6}$ m^2/s (El-Dessouky & Ettouney, 2002) and the density of sea water is $\rho_{sea} = 1030$ kg/m^3. Its body mass (m) is 1.89 kg (Jones *et al.*, 2011), body volume (V_O) is $1.94 \times 10_{-3}$ m^3 (Fossette *et al.*, 2010; Lutcavage, Bushnell & Jones, 1992), and planform area is $A_p = 0.0260$ m^2. Since I do not find any information of the measured thrust of a leatherback turtle during the vigorous swimming, I estimate it based on the thrust of a vigorously swimming green sea turtle (*Chelonia mydas*) assuming that the vigorous swimming is a typical swimming pattern of sea turtle hatchlings (Davenport & Clough, 1986). According to Davenport *et al.* (Davenport,

Munks & Oxford, 1984), the body length of a green sea turtle hatchling is 11 cm, and its thrust during the vigorous swimming is 0.61 N (average thrust over 5 s). Then, the thrust of a vigorously swimming leatherback turtle is estimated to be about 2.86 N, assuming that the thrust is proportional to the square of the body length (Watson & Granger, 1998). The drag coefficients at $Re = 2 \times 10^5$ and α = -22° are 0.127 and 0.15 with and without the ridges, respectively. Thus, the amount of drag reduction by the longitudinal ridges is about 0.19 N, which is 6.6% of the thrust force during the vigorous swimming. Therefore, the amount of drag reduction by the ridges is quite remarkable during the vigorous swimming.

On the other hand, the lift coefficients during the vigorous swimming ($Re = 2 \times 10^5$ and α = -22°) are -0.291 and -0.331 with and without the ridges, respectively. Then the lift forces during the vigorous swimming with and without the ridges are -2.39 N and -2.72 N, respectively. The buoyancy force by sea water on a hatchling leatherback turtle is $B = \rho_{sea} V_O g$ = 19.6 N. Therefore, the net forces on the hatchling turtles with and without the ridges are $B \;\; mg + L$ = -1.33 N and -1.66 N, respectively. This analysis shows that the longitudinal ridges reduce negative net vertical force by about 20% but still maintain negative value of the vertical force on the body of a hatchling leatherback turtle. Unnecessarily large net vertical force can make it difficult for hatchlings to control the swimming direction. Therefore, the reduced negative net vertical force can be beneficial for vigorously swimming hatchlings.

On the other hand, vigorously swimming hatchlings show large periodic flipper motions, resulting in non-uniform swimming speed (Davenport, 1987). The range of swimming speed is 0.738 - 1.714 m/s (3.1 7.2 l/s) (Davenport, 1987) for the body length (l) of 23.8 cm, whose corresponding Reynolds numbers are Re = 1.9 4.4 $\times 10^5$. At these Reynolds numbers and α = -22, the longitudinal

ridges reduce the drag and increase the lift (Figure 3.4,3.5), indicating that the hydrodynamic performance of the ridges is still maintained during the flipper motion.

3.3 Importance of the hydrodynamic force variations for adults

During active ascending swimming, the angle between the swimming and horizontal directions (θ in Figure 1.5) is $20^\circ - 30^\circ$ (Fossette *et al.*, 2010). So, the changes in the forces opposite and perpendicular to the gravity direction ($F_v = L\cos\theta - D\sin\theta$ and $F_h = L\sin\theta + D\cos\theta$, respectively), and their ratio due to the ridges are also similar to those of L, D and L/D, respectively: e.g., for $\theta = 30^\circ$, F_v and F_v/F_h increase by 18% and 5%, respectively. High Reynolds numbers are characteristic of the swimming mode of active ascent by adult leatherback turtles in the V-shaped diving (Fossette *et al.*, 2010). These results suggest that the hydrodynamic performance can be enhanced by the ridges in the V-shaped diving where lift generation is required due to negative buoyancy during most of their ascent. Therefore, the longitudinal ridges on the carapace of leatherback turtles provide superior hydrodynamic performance by reducing the drag in hatchlings swimming and generating additional lift in adults swimming.

3.4 Flow-filed measurements for the case of hatchlings

I conducted velocity measurements using DPIV to investigate the modifications of flow structures by the longitudinal ridges. Measurements were performed at two conditions, α = -22° and $Re = 2 \times 10^5$, and $\alpha = 18^\circ$ and $Re = 5 \times 10^5$, that are characteristic of the vigorous swimming of hatchlings and the active ascending swimming of adults, respectively (see Experimental Set-up

(Flow-field measurements) and Figure 2.8 for the experimental set-up). Figure 3.7-3.18 shows the flow fields at α = -22° and $Re = 2 \times 10^5$ (vigorous swimming of hatchlings) at which the ridges reduced the drag by 15.5% and increased the lift by 12% (see Figure 3.4, 3.5). As shown in Figure 3.7-3.10, the flow separates at rear part of the body (separation starts from x/l = -0.21) in the absence of the ridges. With the ridges, flow separation is significantly delayed (there is no separation at $z = z_1$ and separation starts from x/l = -0.06, -0.18, and -0.12 at $z = z_2$, z_3, and z_4, respectively), which is the main reason of drag decrease and lift increase by the ridges. To understand the mechanism of separation delay by the ridges, the contours of instantaneous vorticity and velocity vectors on four cross-flow ($y - z$) planes are drawn in Figure 3.15-3.18. In the absence of the ridges, the shear layer instability occurs after flow separation (see the flow at $x = x_3$) and strong streamwise vortices are generated at a downstream location ($x = x_4$). On the other hand, with the ridges, flow locally separates across the first off-center ridge at $x = x_1$ because this ridge is not aligned to local streamlines. Then, a shear layer evolves, and streamwise vortices are generated at $x = x_2$ and get stronger further downstream. These strong streamwise vortices bring momentum to the flow near the surface, and enable the flow to resist the adverse pressure gradient and to delay the separation. Although the local separation at $x = x_1$ increases the drag, the drag reduction from the main separation delay is much larger than this drag increase, resulting in a significant decrease of total drag. Therefore, the mechanism responsible for main separation delay by the ridges is the generation of streamwise vortices through a local separation by the ridges (figure 3.19).

3.5 Flow-field measurements for the case of adults

Figure 3.20-3.36 shows the flow fields at $\alpha = 18^{\circ}$ and $Re = 5 \times 10^5$ (active ascending swimming of adults) at which both the drag and lift are increased by 5.6% and 11%, respectively, thereby resulting in the increase of the lift-to-drag ratio by 5% by the ridges. From the oil-surface visualization (Figure 3.20,3.21), separation and reattachment lines denoted as solid and dashed red lines, respectively, are formed at the front part of the body in the absence of the ridges. On the other hand, with the ridges, separation occurs only locally near the centerline of the front part. At the rear part of the body, however, it was almost impossible to identify flow structures from the surface-oil visualization because the oil moved downward due to the steeply inclined rear surface. Therefore, separation lines are obtained from velocity measurements above the rear surface (Figure 3.30-3.35). Figure 3.36 shows that the separation line on the rear surface is broadened with the ridges. This result indicates that the ridges suppress the formation of separation bubble existing on the front surface but enhance the separation on the rear surface. Without the ridges, the separation bubble observed on the front surface is similar to that on a low Reynolds number airfoil causing its performance deterioration (Lissaman, 1983; O'Meara & Mueller, 1987; Kerho *et al.*, 1993). Thus, with the ridges, the hydrodynamic performance is increased owing to the reduced separation bubble on the front surface. To explain the suppression of front-body separation by the ridges, contours of the instantaneous streamwise vorticity on four $y - z$ planes for both models are shown in Figure 3.22-3.29. In these figures, the spanwise domain is in between the first and second off-center ridges (figure 3.22-3.25), where weak separation exists without the ridges and no separation occurs with the ridges (Figure 3.20,3.21). Without the ridges, flow separation is so weak that there

is no strong shear layer evolution. On the other hand, the second off-center ridge which is misaligned with local streamlines produces local flow separation in the spanwise direction at x_1. Then, as the fluid flows downstream, strong streamwise vortices are produced at x_2 x_4. These streamwise vortices enable the flow to resist the adverse pressure gradient by supplying momentum to the flow near the surface, which in turn removes the separation on the front surface in between the first and second off-center ridges. Although a part of the separation bubble is suppressed by the ridges, the drag force on the model with the ridges is greater by 5.6% as compared to that without the ridges. This is because the flow separates earlier on the rear surface with the ridges than without the ridges (Figure 3.32-3.38). The early separation at $z/l = 0.04$ is caused by the ridge itself (Figure 3.34). Therefore, this broadened separated region on the rear surface with the ridges leads to the increase in the form drag because this part of surface is nearly vertical at this high angle of attack. On the other hand, as discussed above, the ridges suppress the separation bubble at the front surface where the surface is nearly horizontal, and thereby enhance the lift force by 11%. This increase in the lift contributes to the increase in the lift-to-drag ratio, although the drag is increased.

3.6 Effect of a yaw angle variation

In the presence of ocean current or during turning motion of a turtle, the swimming direction does not coincide with the freestream direction. To examine this effect, we measure the drag, lift and side forces by varying the yaw angle from $\gamma = 0^\circ$ to 30° (Figure 2.25) for both the vigorous and active ascending swimming, and present their variations in Figure 3.37(a). At α = -22° and Re = 2×10^5 (vigorous swimming of hatchlings; Figure 3.37a), the ridges reduce

the drag and increase the lift at $\gamma = 0$ to 30. The side force rapidly increases with increasing yaw angle. The ridges increase the side force more at a large yaw angle of 30°, although they do not change it much at low yaw angles. At $\alpha = 18°$ and $Re = 5 \times 10^5$ (active ascending swimming of adults; Figure 3.37(b)), the ridges enhance the lift and lift-to-drag ratio. On the other hand, the side force shows very different behaviors: i.e., without the ridges, the side force becomes negative at low yaw angles and then positive at a large yaw angle of 30°, whereas it continuously increases with increasing yaw angle with the ridges. These results suggest that, unless the yaw angle is very large, the hydrodynamic roles of the longitudinal ridges in terms of the lift, drag, and their ratio are still similar to those of zero yaw angle.

3.7 Effect of a head

Since the separation bubble exists on the front surface of the model for the active ascending swimming, the presence of turtles head may affect the flow above the front surface. According to previous observations, the angle of the head from the body of a leatherback turtle does not noticeably change during swimming (Davenport, 1987; Oliver *et al.*, 2000). Therefore, we constructed additional carapace models including the head part by scanning the head of a leatherback turtle (Figure 2.9) and measured the drag and lift forces. In the case of high attack angle and high Re condition that represents the active ascending swimming of adults, the ridges enhance both the lift (9.3%) and lift-to-drag ratio (5.2%) even in the presence of the head (see Figure 3.38(b)). On the other hand, in the case of negative attack angle and low Re condition that represents the vigorous swimming of hatchlings, the ridges significantly reduce the drag (up to 22%) and increase the lift (up to 23.3%) (Figure 3.38(a)). These

results indicate that the presence of the head part does not change the hydrodynamic roles of the ridges for both the vigorous and active ascending swimming. Leatherback turtles have a vaulted carapace, whereas other hard-shelled sea turtles have relatively flat carapaces. Typically, the flow over a vaulted surface may experience stronger adverse pressure gradient followed by flow separation (White, 2008). Therefore, leatherback turtles, unlike other sea turtles, may have a higher probability of massive flow separation on their carapace, so any device that aids separation delay should be more useful in swimming than other turtles having rather flat carapaces. Also, in contrast to the V-shaped diving of leatherback turtles, other sea turtles (*Chelonia mydas*, *Caretta caretta*) are generally known for swimming at a location where they achieve a neutral buoyancy, and thus they may not experience a negative buoyancy during their swimming (Davenport & Clough, 1986; Watson & Granger, 1998). Therefore, the lift enhancement by the ridges in V-shaped diving may not be necessary in other sea turtles swimming.

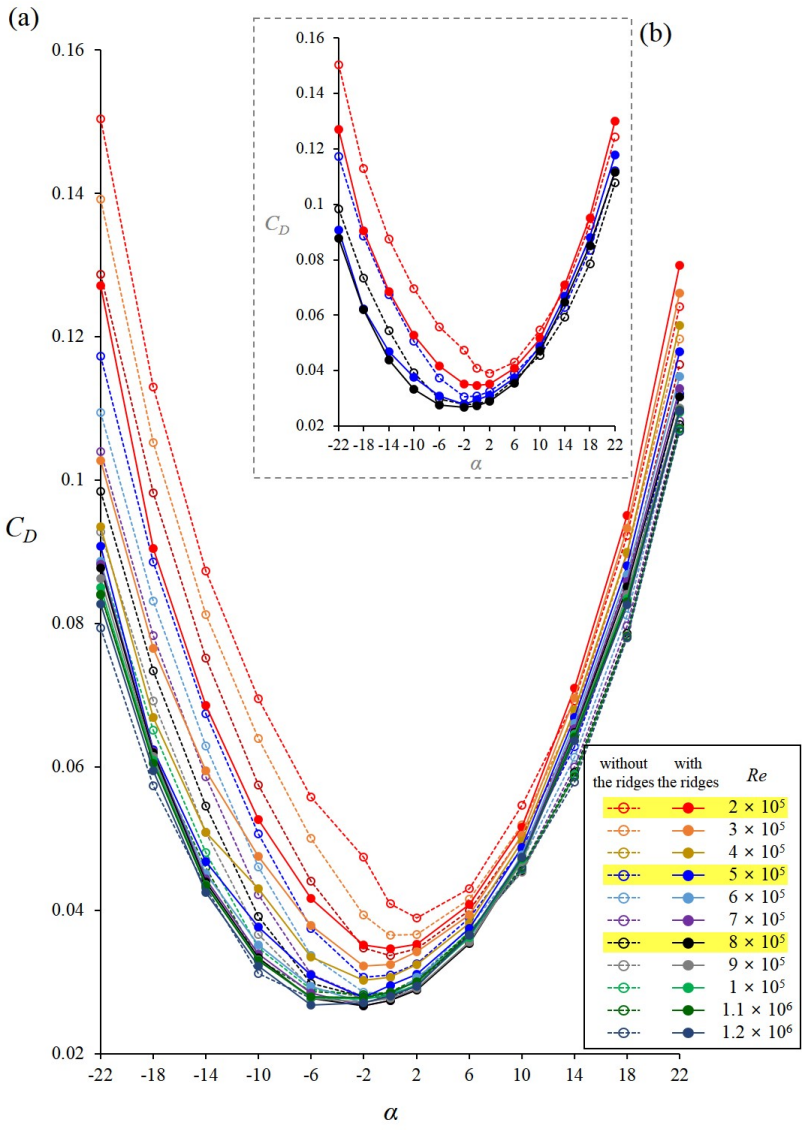

Figure 3.1. Results of force measurements (γ=0°). (a) Variations of the drag coefficients (C_D) on the models with (solid symbols) and without (open symbols) the ridges depending on the angles of attack (α) and Reynolds numbers (Re); (b) Variations of the drag coefficients with three Reynolds numbers ($Re = 2 \times 10^5$, 5×10^5, 8×10^5) for clarity.

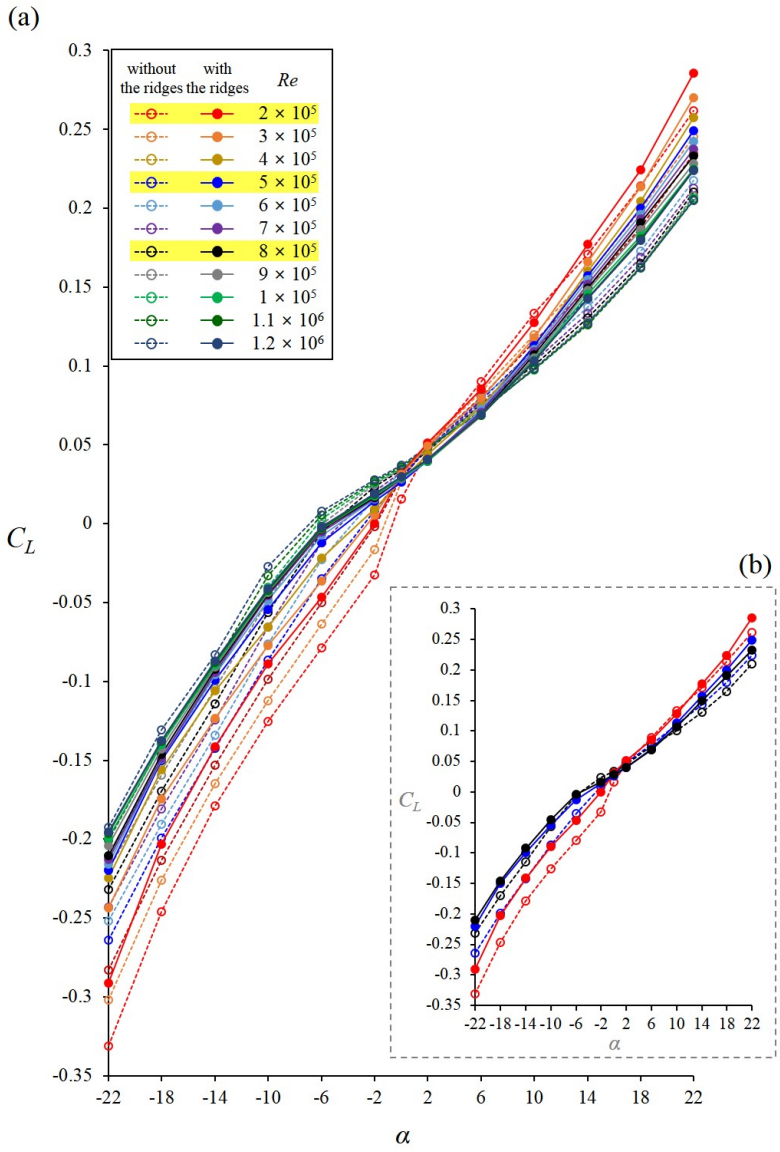

Figure 3.2. Results of force measurements (γ=0°). (a) Variations of the lift coefficients (C_L) on the models with (solid symbols) and without (open symbols) the ridges depending on the angles of attack (α) and Reynolds numbers (Re); (b) Variations of the lift coefficients with three Reynolds numbers ($Re = 2 \times 10^5$, 5×10^5, 8×10^5) for clarity.

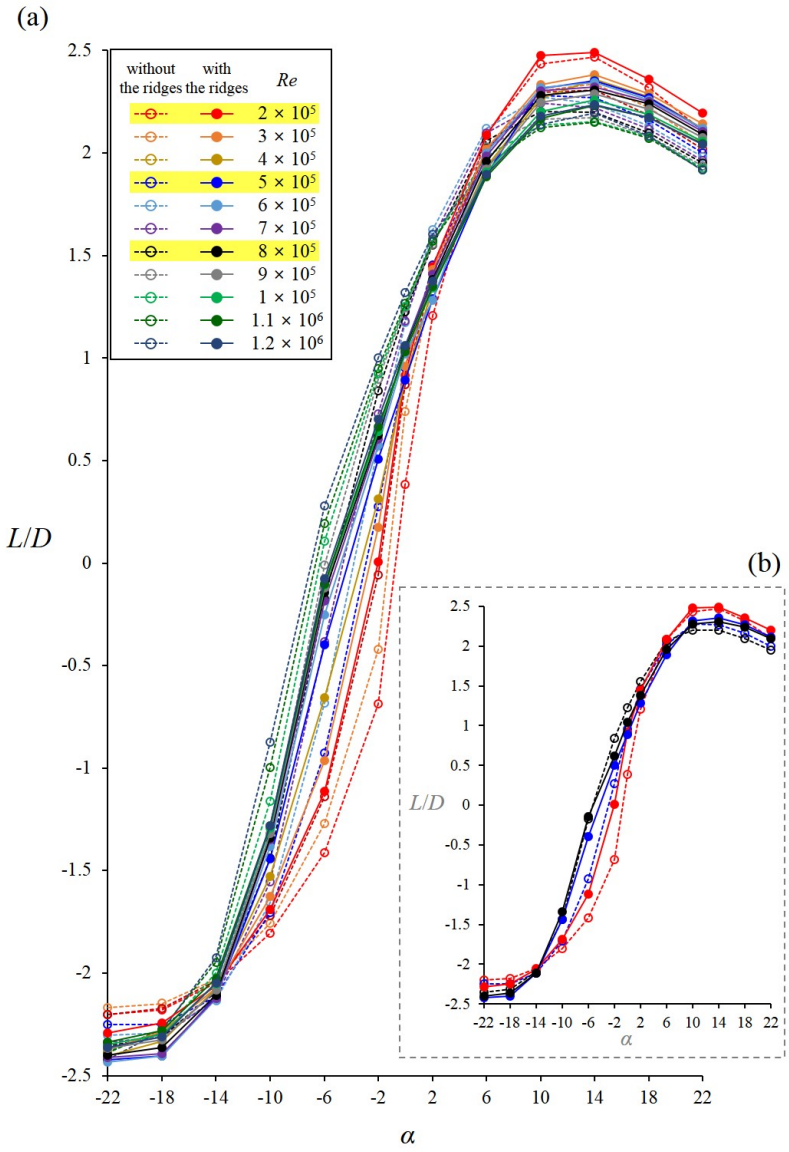

Figure 3.3. Results of force measurements (γ=0°). (a) Variations of the lift-to-drag ratio (L/D) on the models with (solid symbols) and without (open symbols) the ridges depending on the angles of attack (α) and Reynolds numbers (Re); (b) Variations of the lift-to-drag ratio with three Reynolds numbers (Re = 2×10^5, 5×10^5, 8×10^5) for clarity.

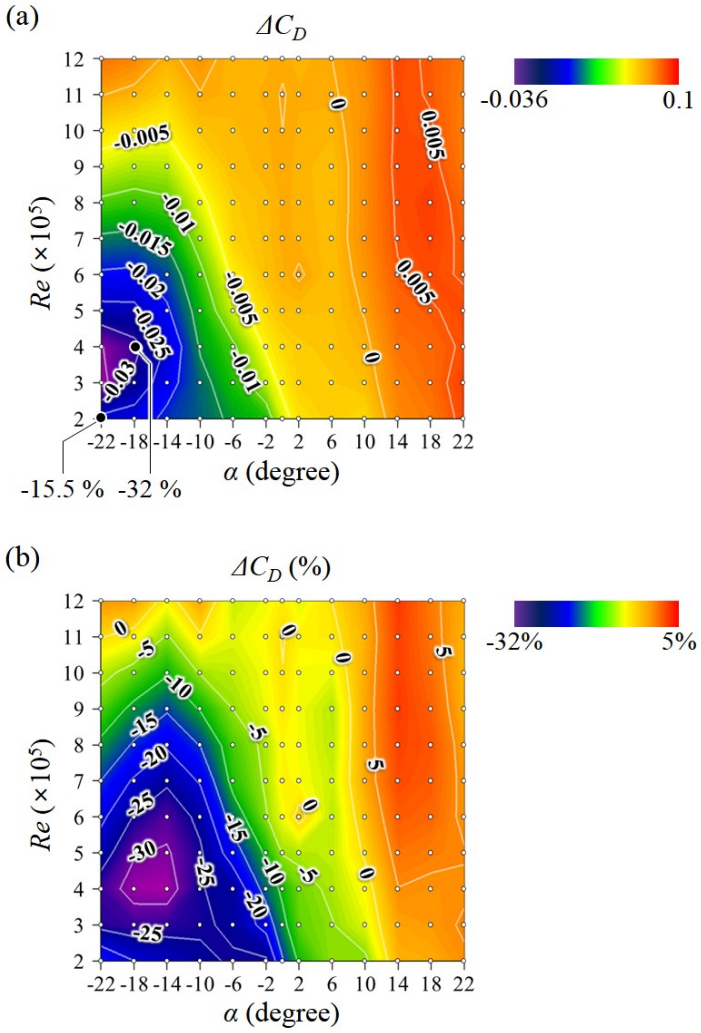

Figure 3.4. Results of force measurements (γ=0°). (a) Variations of the drag coefficient (C_D) by the ridges. Here, $\Delta C_D = C_{D,withtheridges} - C_{D,withouttheridges}$; (b) Variation rates of C_D by the ridges. Here, $\Delta C_D(\%) = (C_{D,withtheridges} - C_{D,withouttheridges})/C_{D,withouttheridges} \times 100$. The white dots in these figures represent the points where the experiments were conducted.

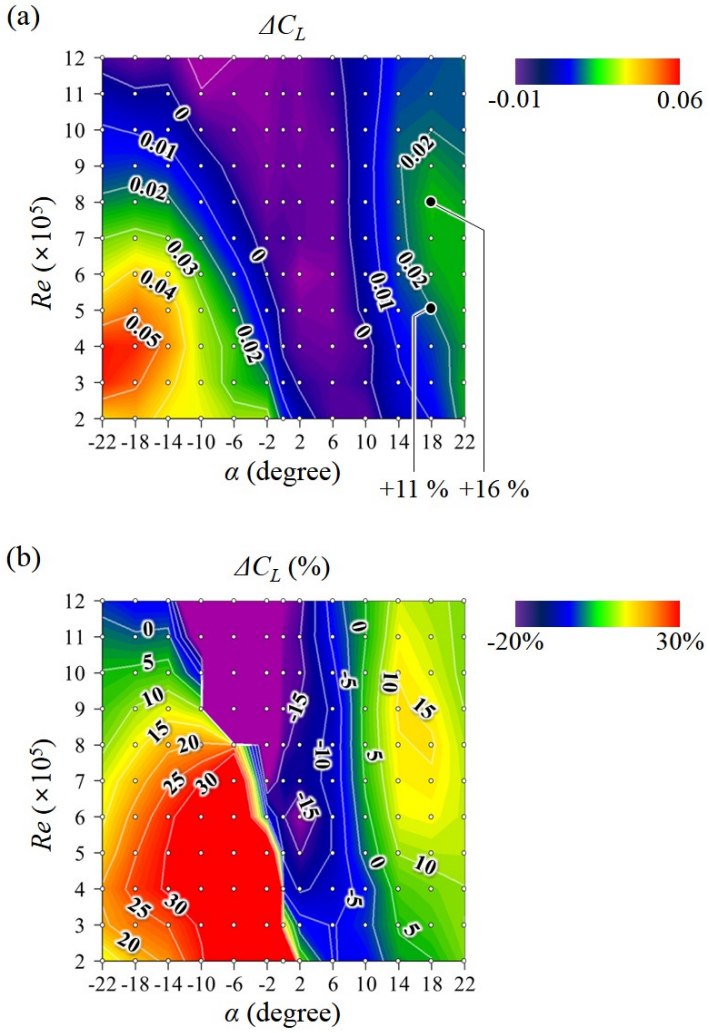

Figure 3.5. Results of force measurements (γ=0°). (a) Variations of the lift coefficient (C_L) by the ridges. Here, ΔC_L=$C_{L,withtheridges}$-$C_{L,withouttheridges}$; (b) Variation rates of C_L by the ridges. Here, $\Delta C_L(\%)$=($C_{L,withtheridges}$-$C_{L,withouttheridges}$)/$C_{L,withouttheridges}$ ×100. The white dots in these figures represent the points where the experiments were conducted.

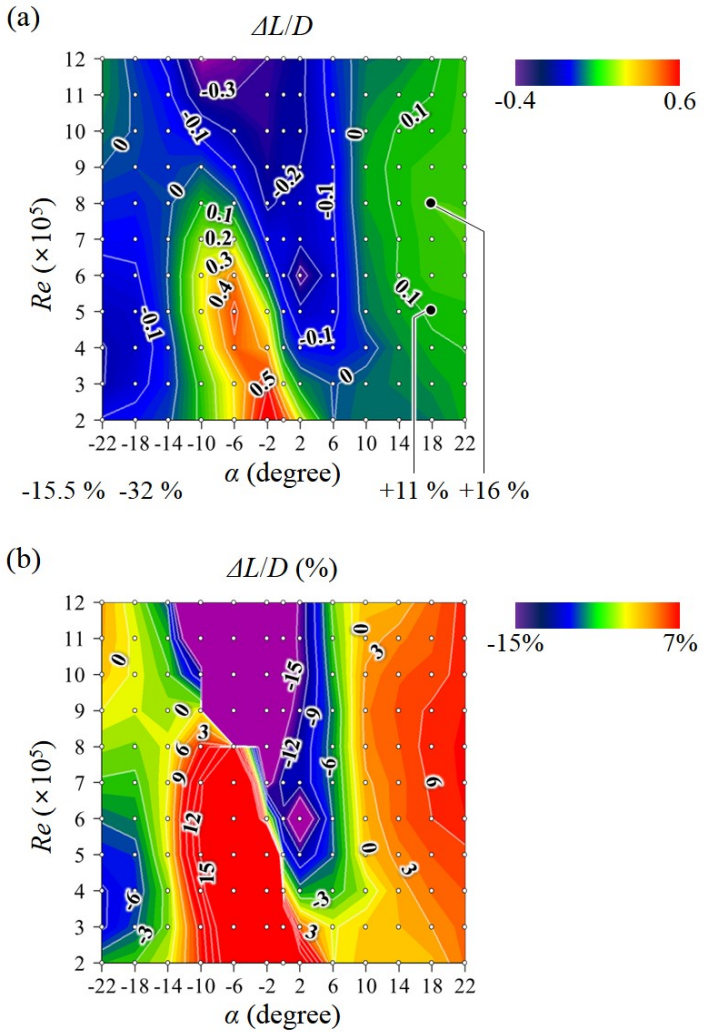

Figure 3.6. Results of force measurements (γ=0°). (a) Variations of the lift-to-drag ratio (L/D) by the ridges. Here, $\Delta L/D$=$L/D_{withtheridges}$-$L/D_{withouttheridges}$; (b) Variation rates of L/D by the ridges. Here, $\Delta L/D(\%)$=($L/D_{withtheridges}$-$L/D_{withouttheridges}$)/$L/D_{withouttheridges}$ ×100. The white dots in these figures represent the points where the experiments were conducted.

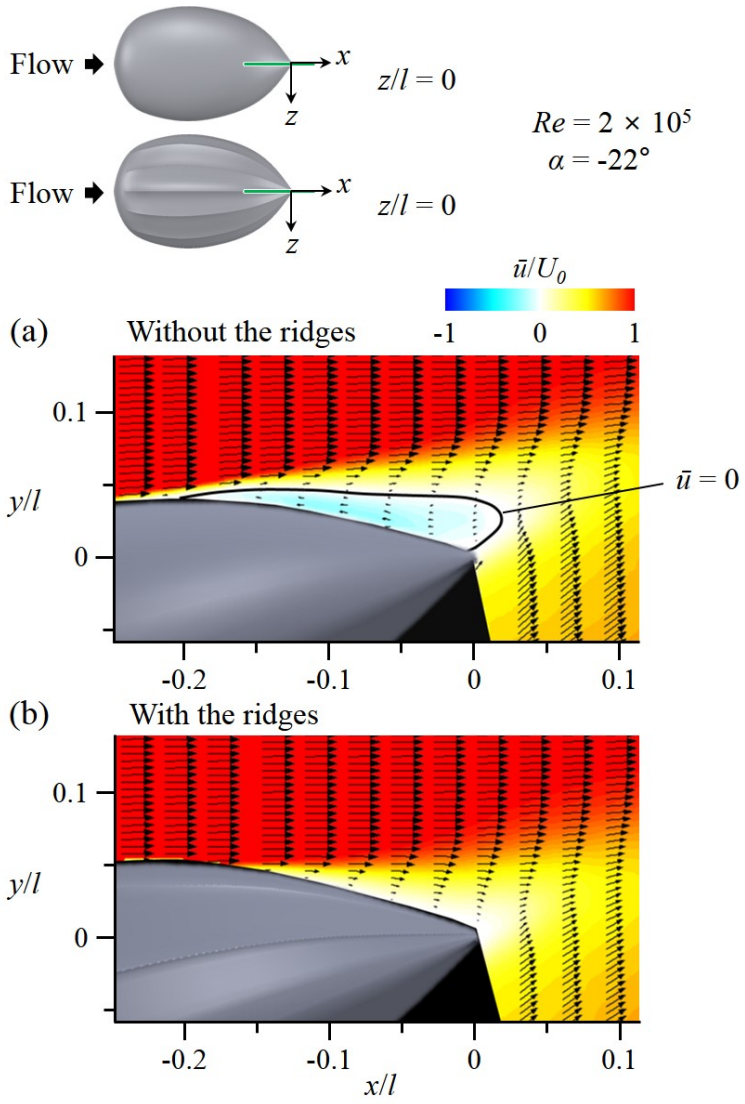

Figure 3.7. Results of flow-field measurements at α=-22° and Re=2×10^5 that represents the vigorous swimming of the hatchlings (z/l=0, γ=0°). (a)Contours of time-averaged streamwise velocity and velocity vectors with absence of the ridges; (b) Contours of time-averaged streamwise velocity and velocity vectors with presence of the ridges.

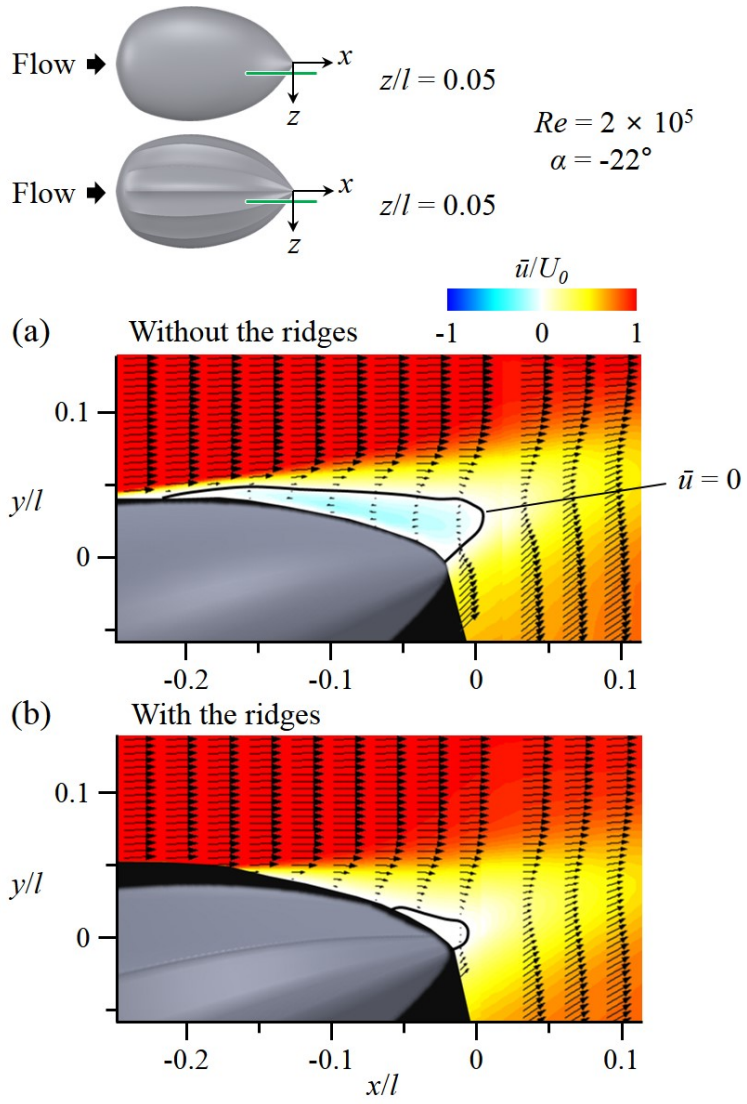

Figure 3.8. Results of flow-field measurements at α=-22° and Re=2×10^5 that represents the vigorous swimming of the hatchlings (z/l=0.05, γ=0°). (a)Contours of time-averaged streamwise velocity and velocity vectors with absence of the ridges; (b) Contours of time-averaged streamwise velocity and velocity vectors with presence of the ridges.

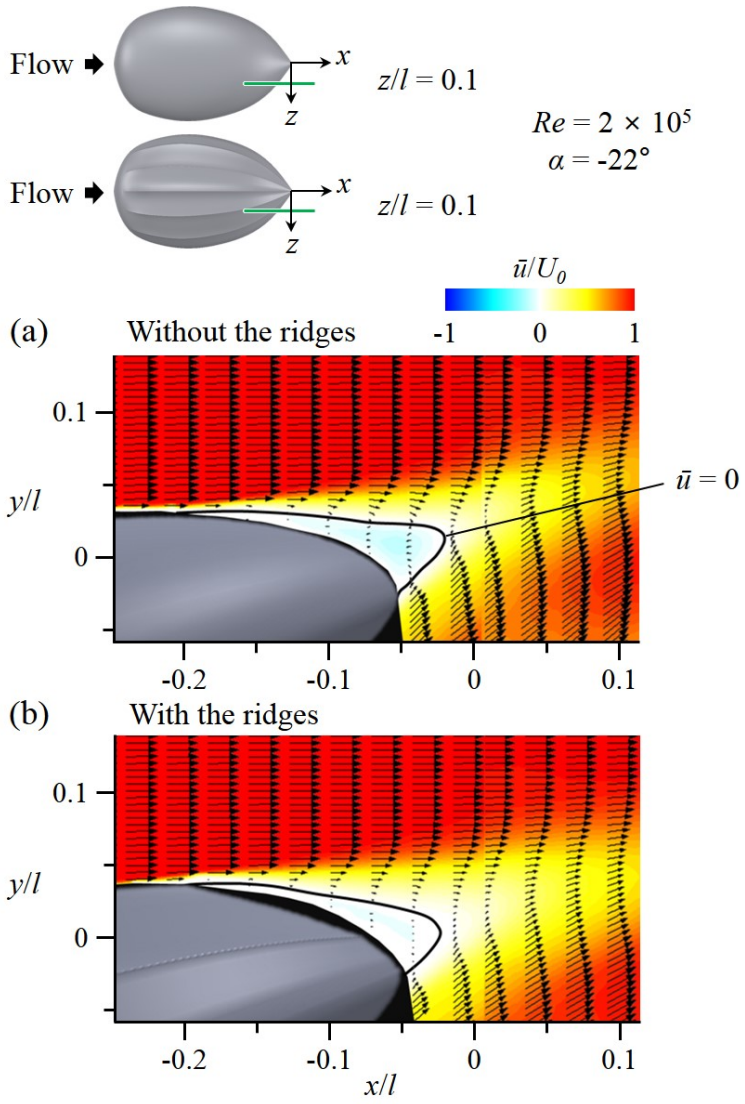

Figure 3.9. Results of flow-field measurements at α=-22° and Re=2×10^5 that represents the vigorous swimming of the hatchlings (z/l=0.1, γ=0°). (a)Contours of time-averaged streamwise velocity and velocity vectors with absence of the ridges; (b) Contours of time-averaged streamwise velocity and velocity vectors with presence of the ridges.

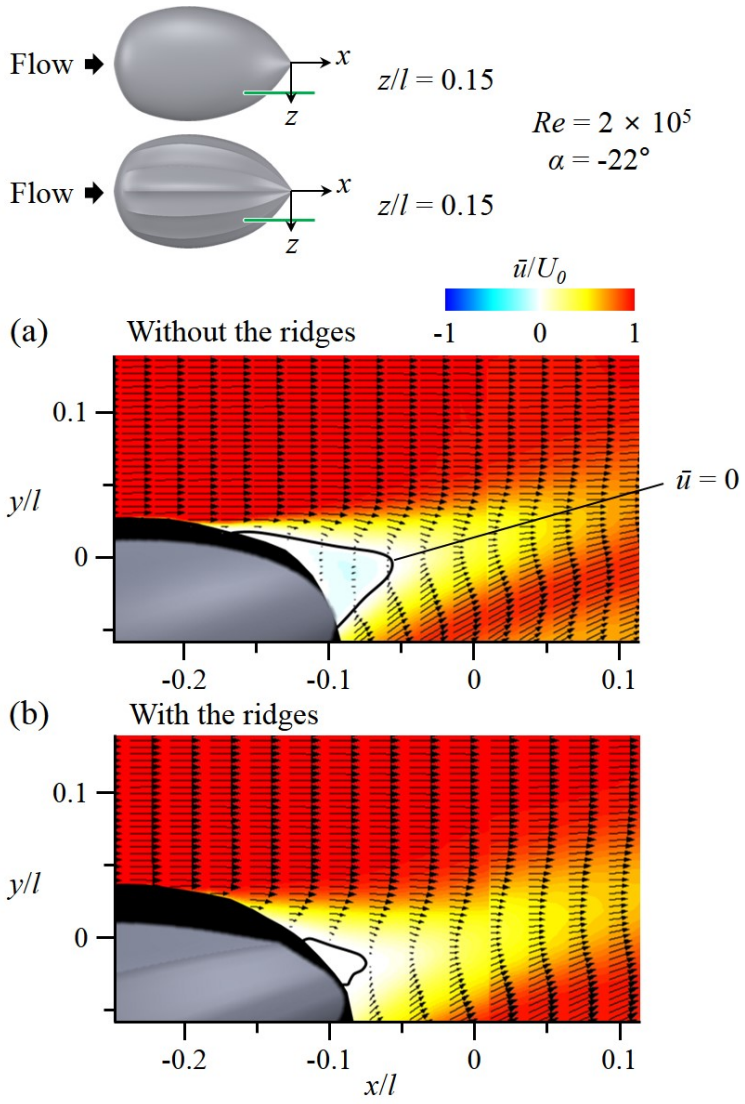

Figure 3.10. Results of flow-field measurements at α=-22° and Re=2×10^5 that represents the vigorous swimming of the hatchlings (z/l=0.15, γ=0°). (a)Contours of time-averaged streamwise velocity and velocity vectors with absence of the ridges; (b) Contours of time-averaged streamwise velocity and velocity vectors with presence of the ridges.

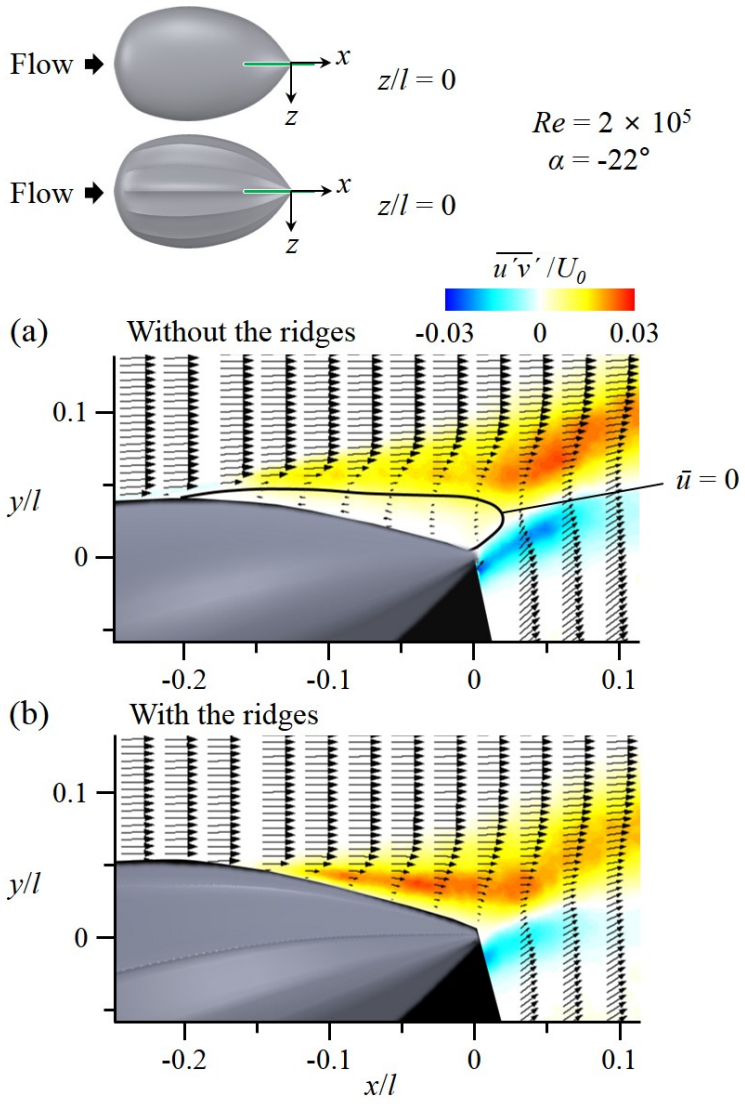

Figure 3.11. Results of flow-field measurements at α=-22° and Re=2×10^5 that represents the vigorous swimming of the hatchlings (z/l=0, γ=0°). (a)Contours of Reynolds shear stress and velocity vectors with absence of the ridges; (b) Contours of Reynolds shear stress and velocity vectors with presence of the ridges.

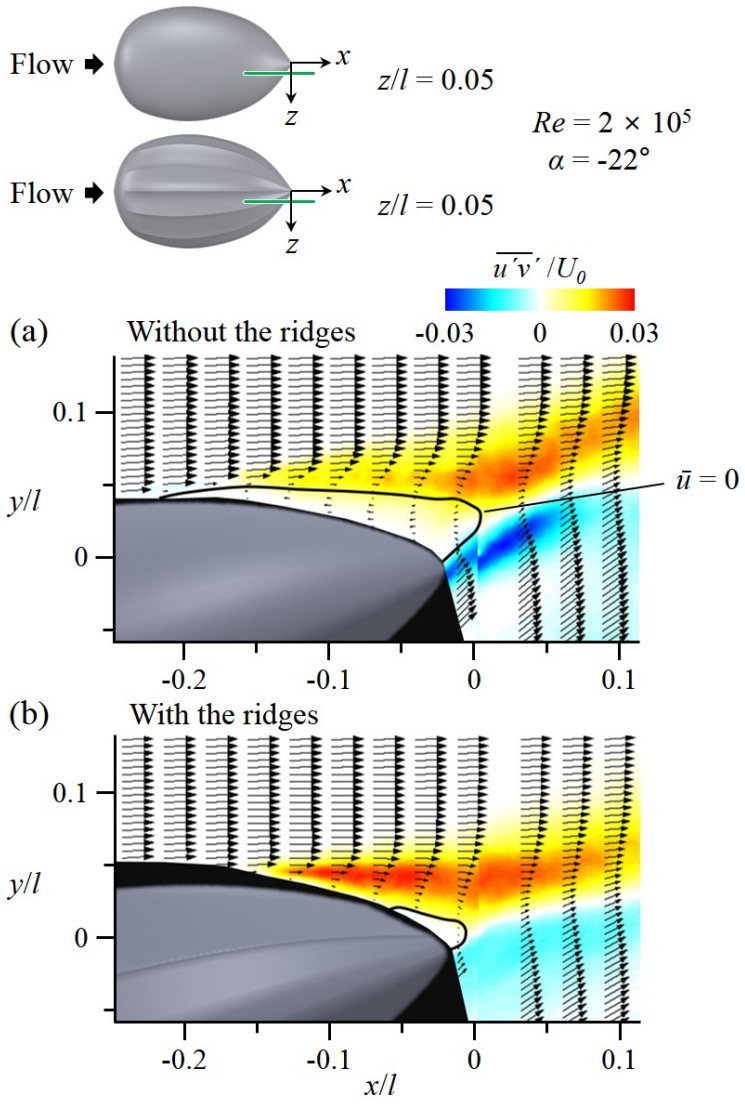

Figure 3.12. Results of flow-field measurements at α=-22° and Re=2×10^5 that represents the vigorous swimming of the hatchlings (z/l=0.05, γ=0°). (a)Contours of Reynolds shear stress and velocity vectors with absence of the ridges; (b) Contours of Reynolds shear stress and velocity vectors with presence of the ridges.

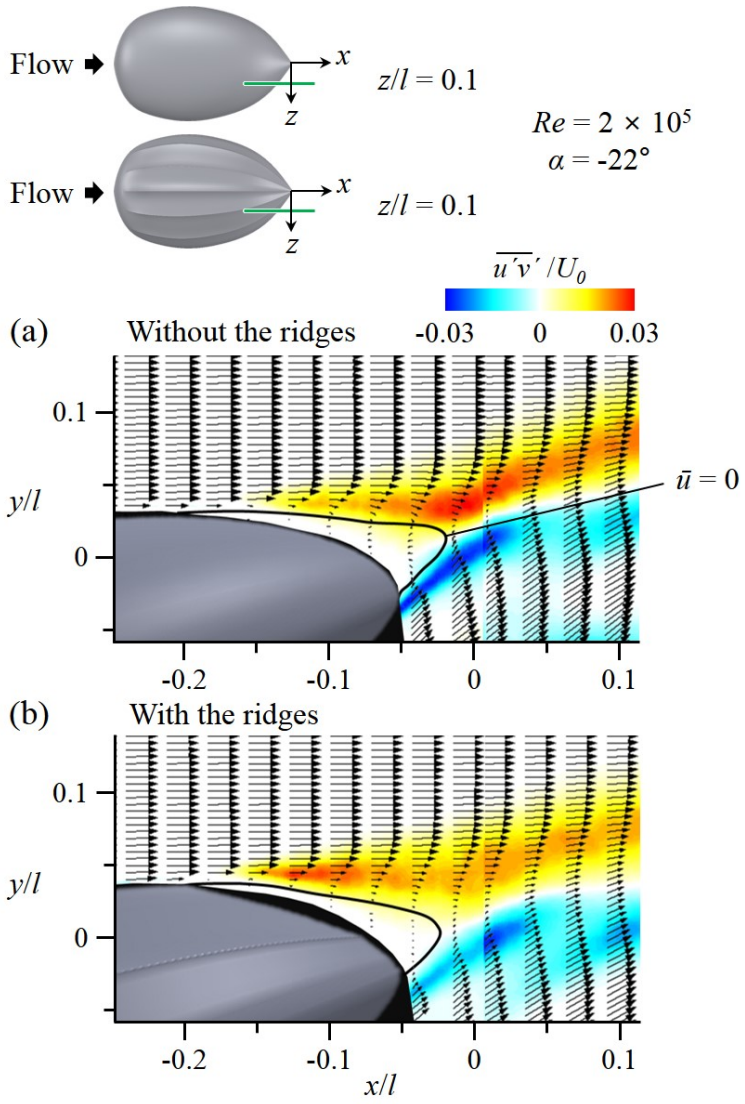

Figure 3.13. Results of flow-field measurements at α=-22° and Re=2×10^5 that represents the vigorous swimming of the hatchlings (z/l=0.1, γ=0°). (a)Contours of Reynolds shear stress and velocity vectors with absence of the ridges; (b) Contours of Reynolds shear stress and velocity vectors with presence of the ridges.

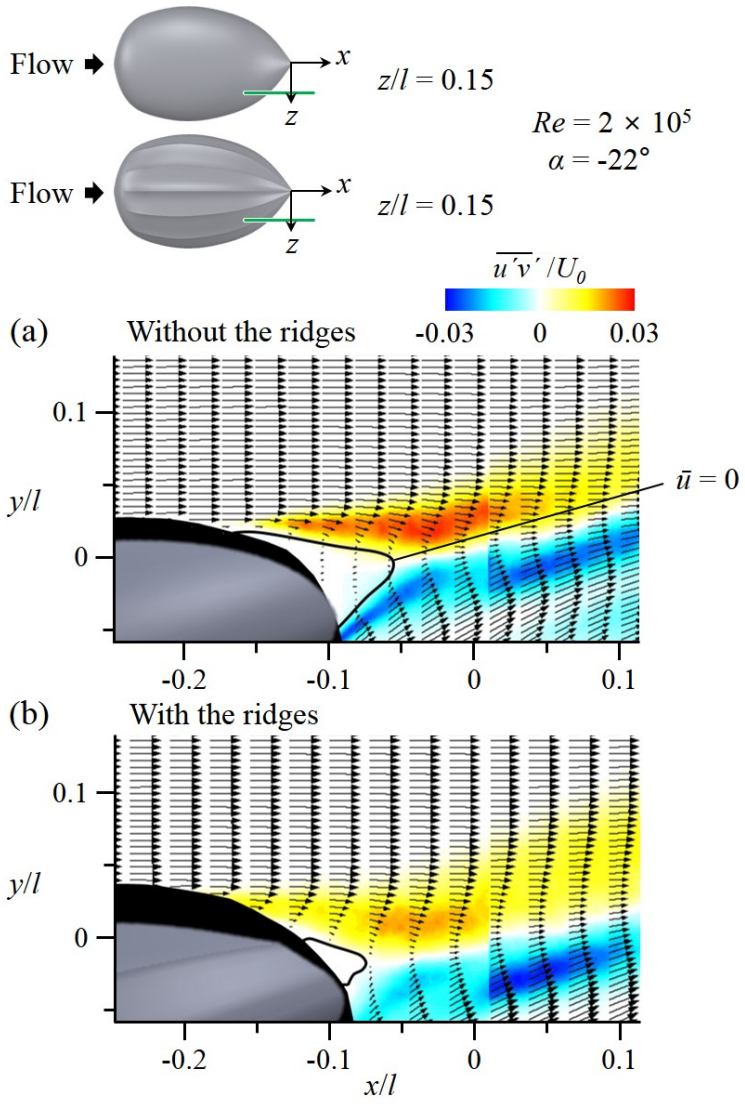

Figure 3.14. Results of flow-field measurements at α=-22° and Re=2×10^5 that represents the vigorous swimming of the hatchlings (z/l=0.15, γ=0°). (a)Contours of Reynolds shear stress and velocity vectors with absence of the ridges; (b) Contours of Reynolds shear stress and velocity vectors with presence of the ridges.

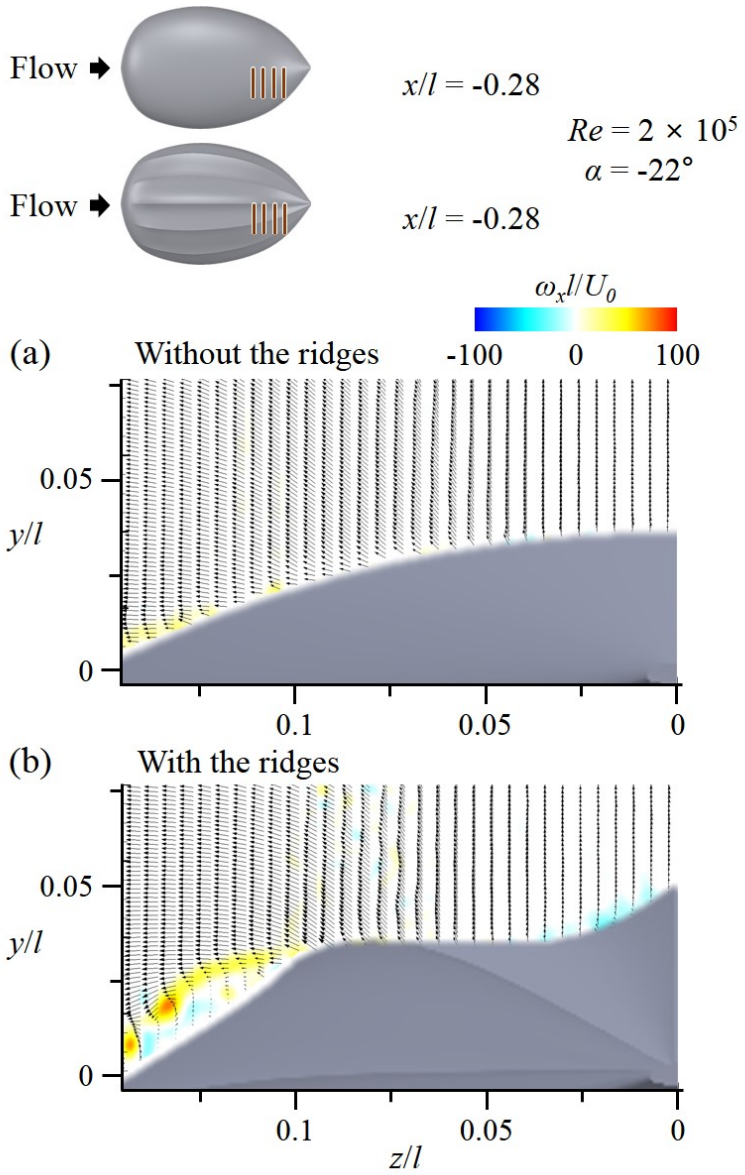

Figure 3.15. Results of flow-field measurements at α=-22° and Re=2×10^5 that represents the vigorous swimming of the hatchlings (x/l=-0.28, γ=0°). (a)Contours of instantaneous streamwise vorticity and velocity vectors with absence of the ridges; (b) Contours of instantaneous streamwise vorticity and velocity vectors with presence of the ridges.

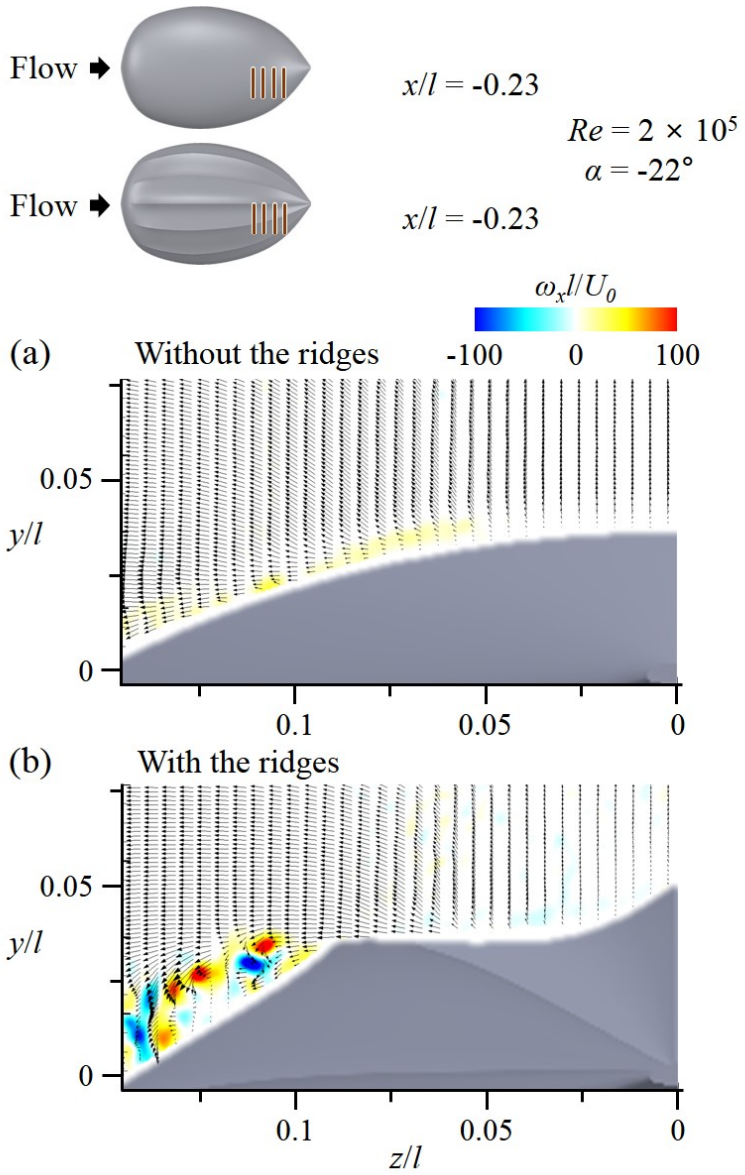

Figure 3.16. Results of flow-field measurements at α=-22° and Re=2×10^5 that represents the vigorous swimming of the hatchlings (x/l=-0.23, γ=0°). (a)Contours of instantaneous streamwise vorticity and velocity vectors with absence of the ridges; (b) Contours of instantaneous streamwise vorticity and velocity vectors with presence of the ridges.

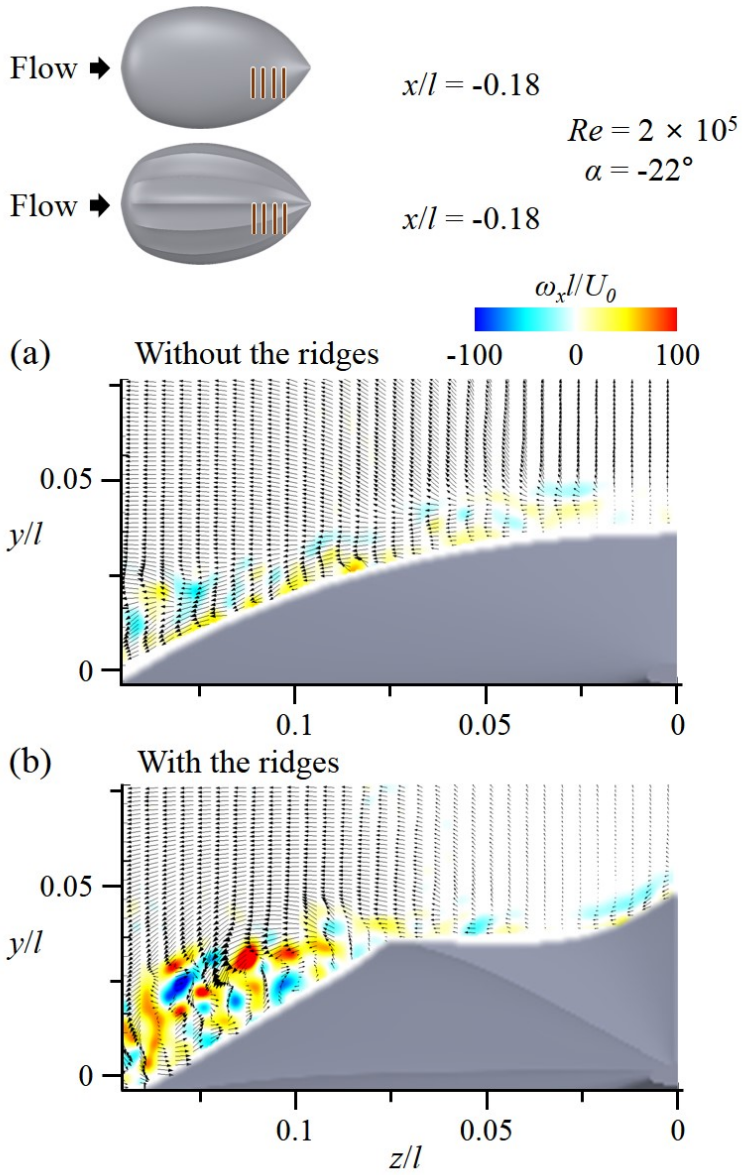

Figure 3.17. Results of flow-field measurements at α=-22° and Re=2×10^5 that represents the vigorous swimming of the hatchlings (x/l=-0.18, γ=0°). (a)Contours of instantaneous streamwise vorticity and velocity vectors with absence of the ridges; (b) Contours of instantaneous streamwise vorticity and velocity vectors with presence of the ridges.

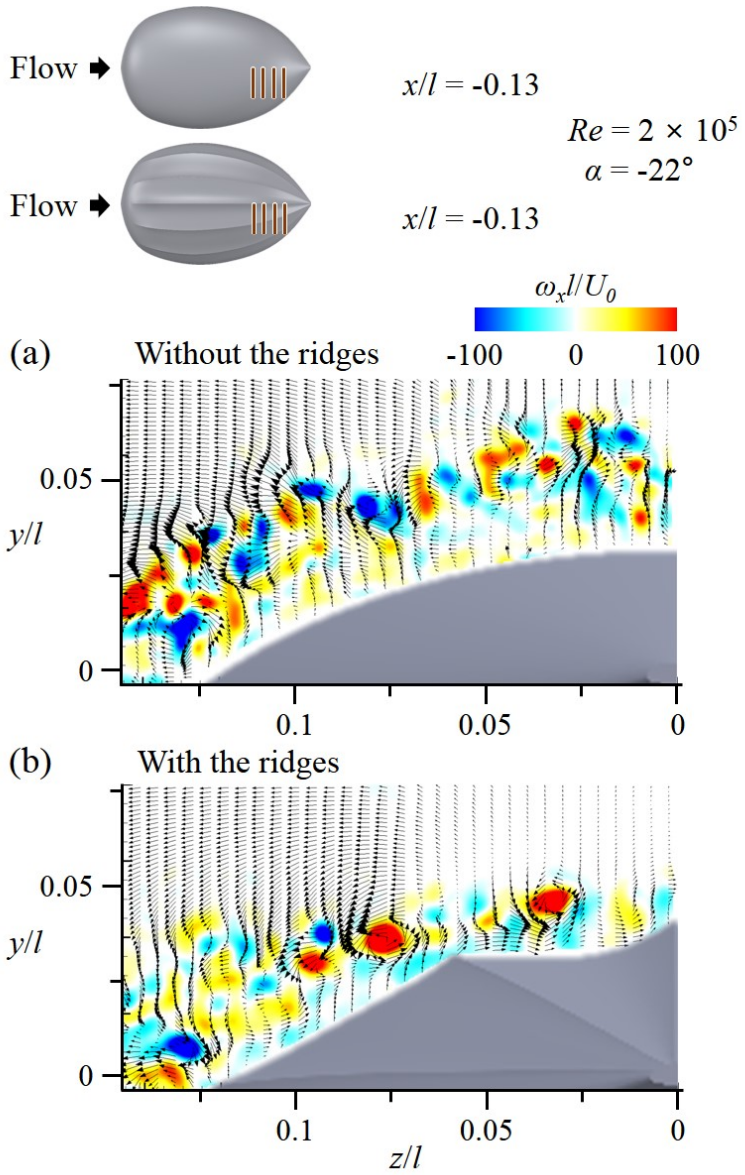

Figure 3.18. Results of flow-field measurements at α=-22° and Re=2×10^5 that represents the vigorous swimming of the hatchlings (x/l=-0.13, γ=0°). (a)Contours of instantaneous streamwise vorticity and velocity vectors with absence of the ridges; (b) Contours of instantaneous streamwise vorticity and velocity vectors with presence of the ridges.

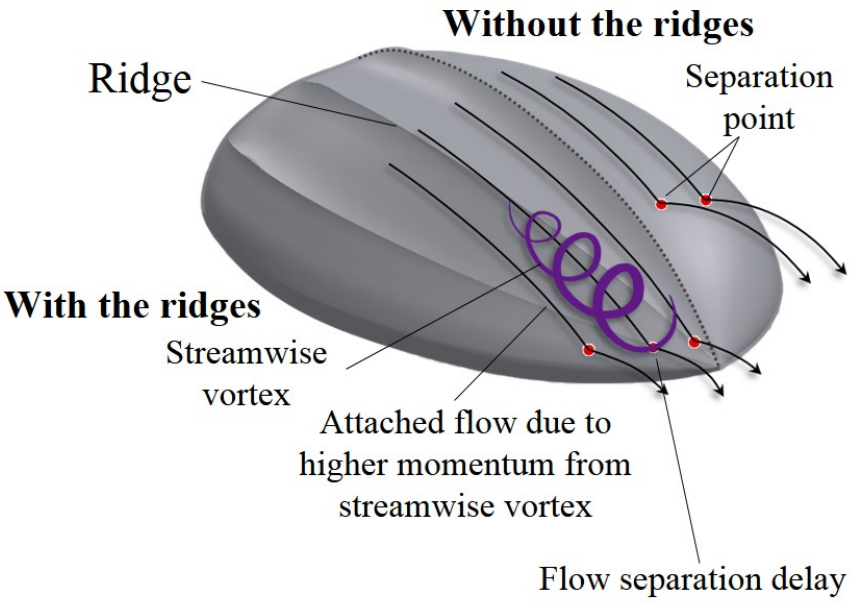

Figure 3.19. Schematic diagram for the mechanism of streamwise vortex generation and separation delay by the ridges.

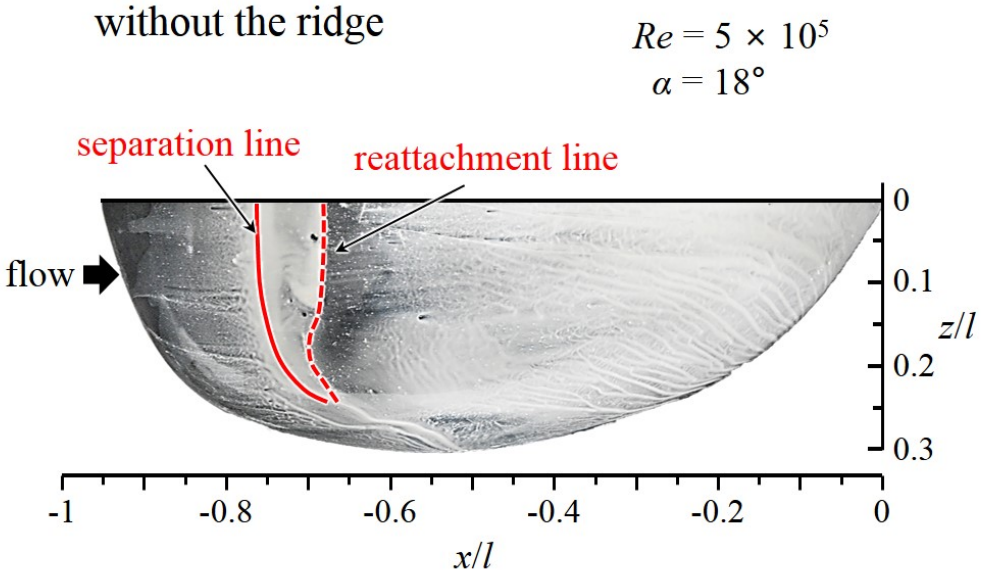

Figure 3.20. Oil-surface visualization on the model without the ridges at α=18° and Re=5×10^5 that represents the active ascending swimming of adults (γ=0°). Red solid and dashed lines denote the locations of flow separation and reattachment on the front surface of the model, respectively.

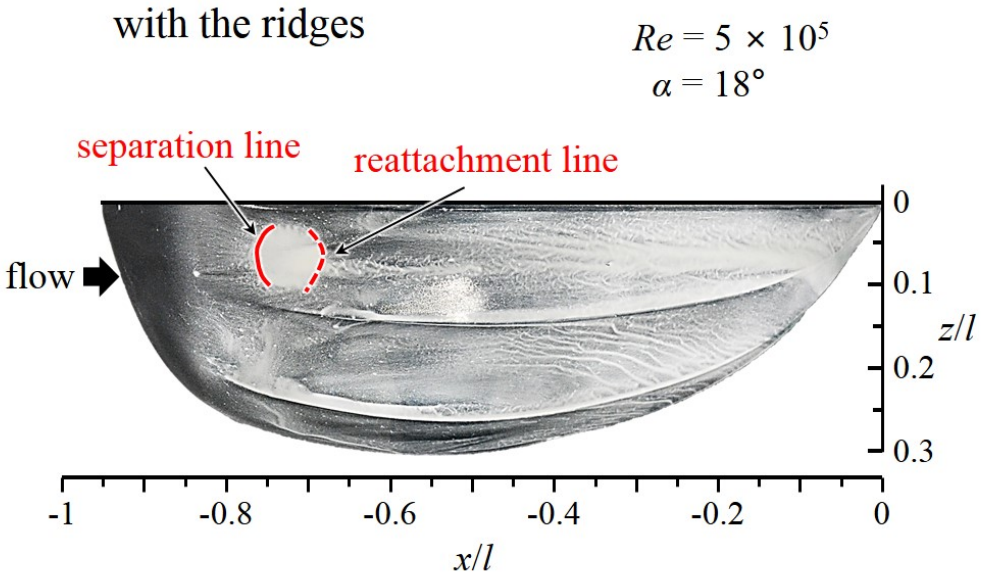

Figure 3.21. Oil-surface visualization on the model with the ridges at α=18° and Re=5×10^5 that represents the active ascending swimming of adults (γ=0°). Red solid and dashed lines denote the locations of flow separation and reattachment on the front surface of the model, respectively.

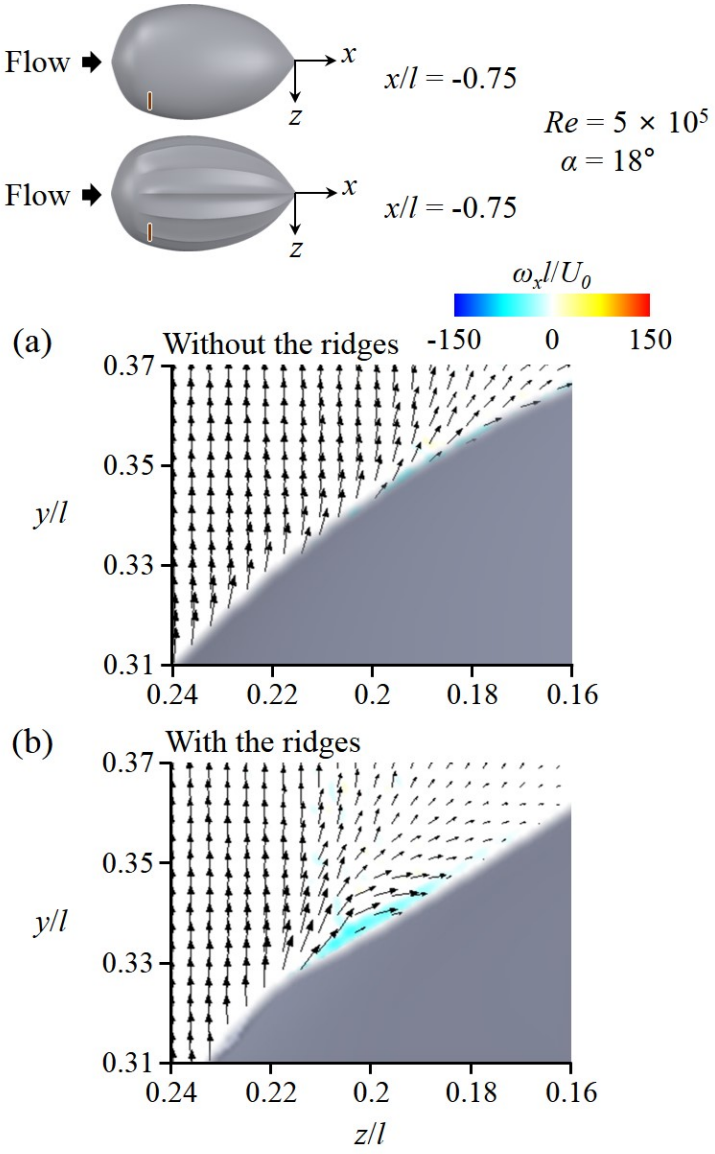

Figure 3.22. Results of flow-field measurements at α=18° and Re=5×10^5 that represents the active ascending swimming of adults (x/l=-0.75, γ=0°). (a) Contours of the instantaneous streamwise vorticity and velocity vectors with absence of the ridges; (b) Contours of the instantaneous streamwise vorticity and velocity vectors with presence of the ridges. Here, the spanwise domain is in between the first and second off-center ridges.

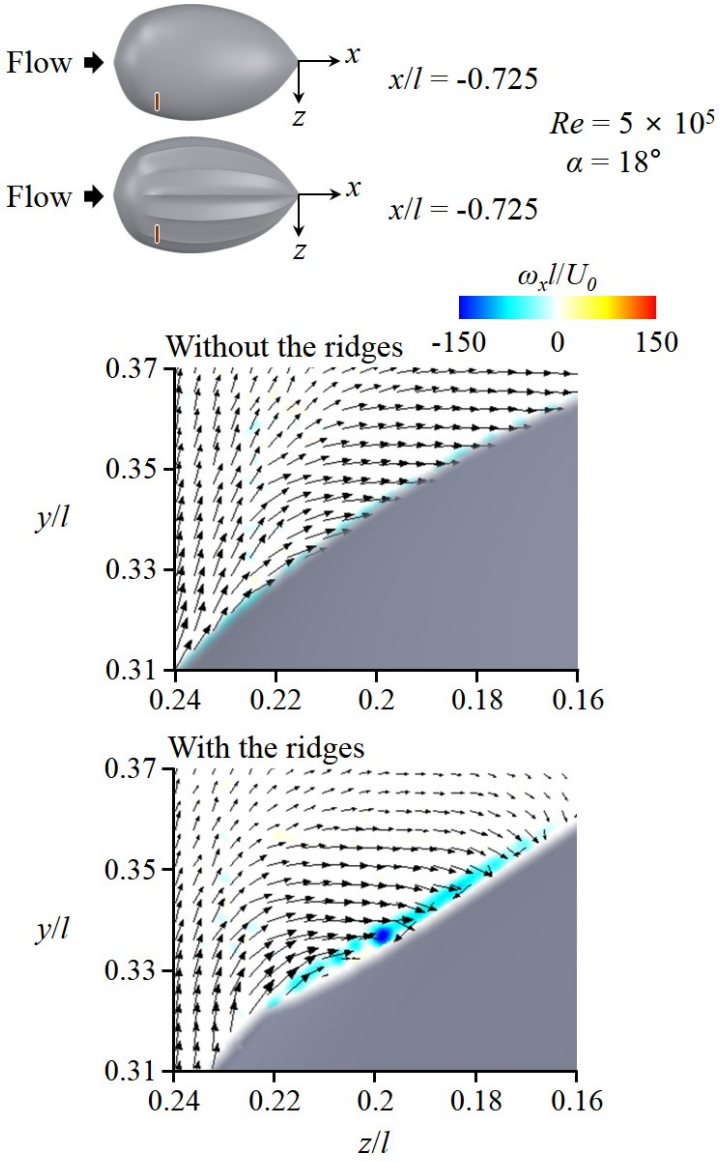

Figure 3.23. Results of flow-field measurements at α=18° and Re=5×10^5 that represents the active ascending swimming of adults (x/l=-0.725, γ=0°). (a) Contours of the instantaneous streamwise vorticity and velocity vectors with absence of the ridges; (b) Contours of the instantaneous streamwise vorticity and velocity vectors with presence of the ridges. Here, the spanwise domain is in between the first and second off-center ridges.

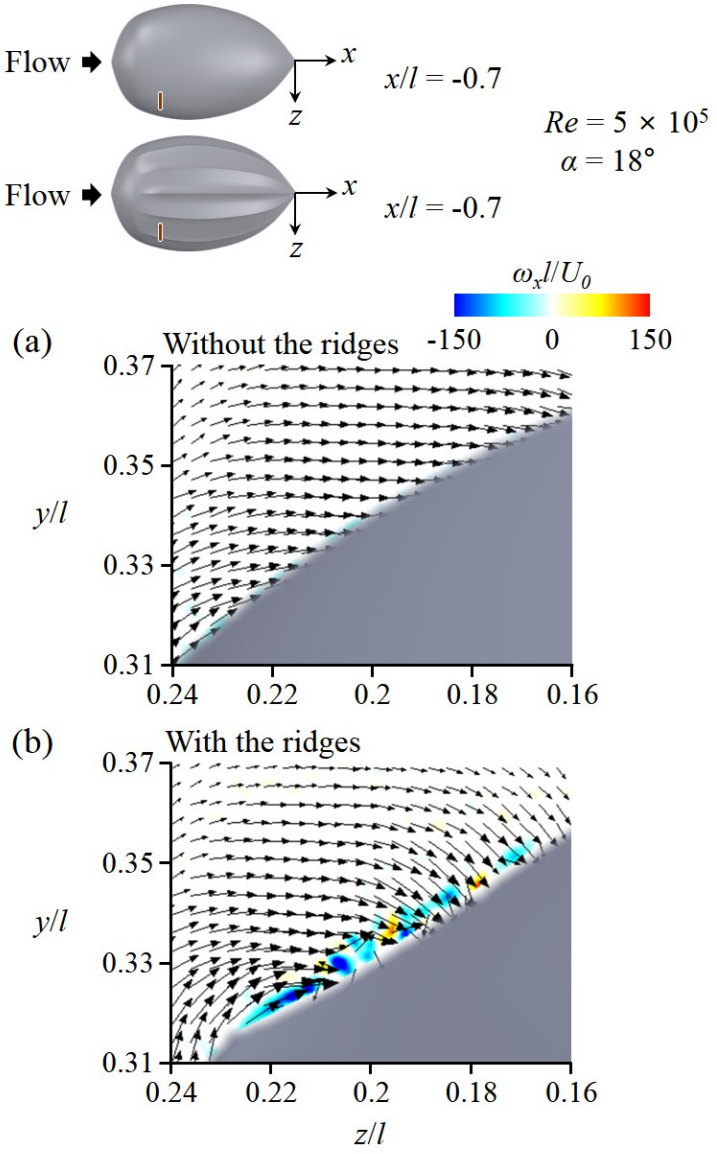

Figure 3.24. Results of flow-field measurements at α=18° and Re=5×10^5 that represents the active ascending swimming of adults (x/l=-0.7, γ=0°). (a) Contours of the instantaneous streamwise vorticity and velocity vectors with absence of the ridges; (b) Contours of the instantaneous streamwise vorticity and velocity vectors with presence of the ridges. Here, the spanwise domain is in between the first and second off-center ridges.

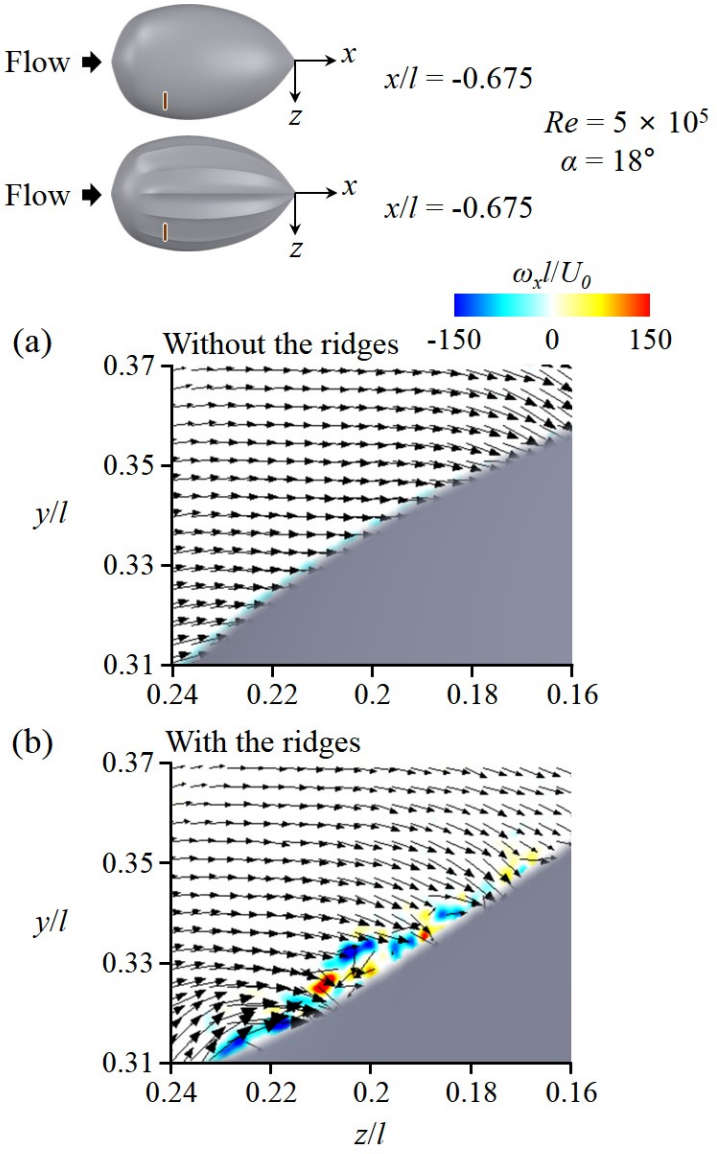

Figure 3.25. Results of flow-field measurements at α=18° and Re=5×10^5 that represents the active ascending swimming of adults (x/l=-0.675, γ=0°). (a) Contours of the instantaneous streamwise vorticity and velocity vectors with absence of the ridges; (b) Contours of the instantaneous streamwise vorticity and velocity vectors with presence of the ridges. Here, the spanwise domain is in between the first and second off-center ridges.

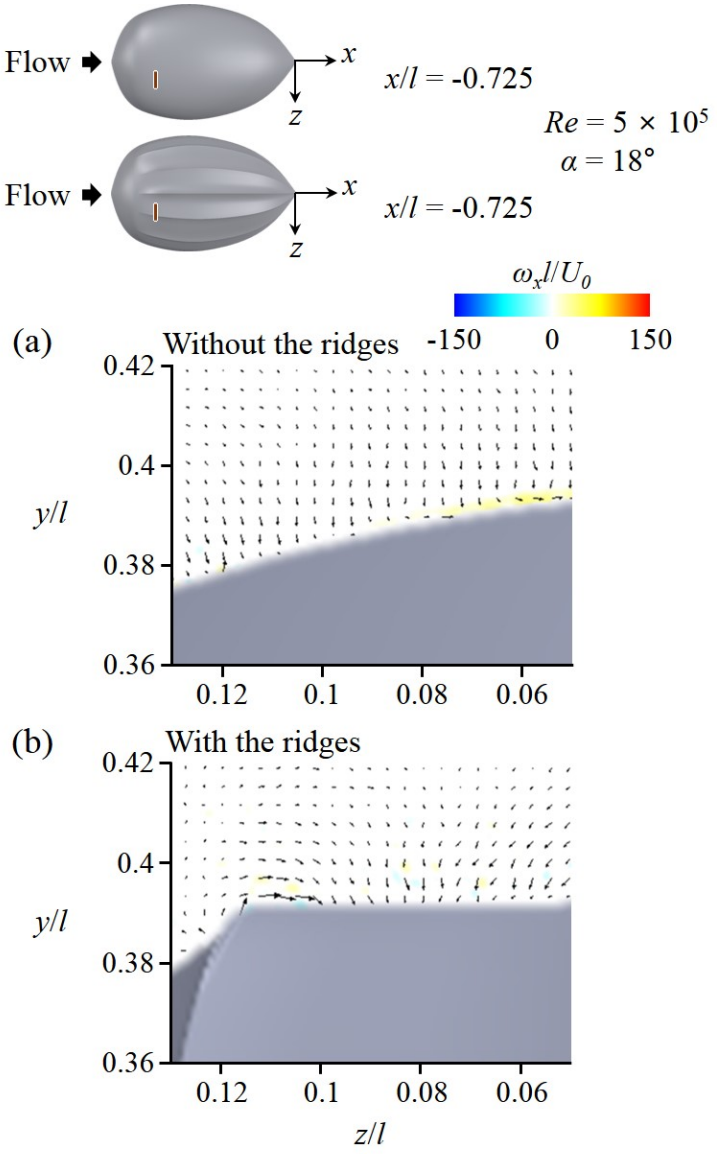

Figure 3.26. Results of flow-field measurements at α=18° and Re=5×10^5 that represents the active ascending swimming of adults (x/l=-0.725, γ=0°). (a) Contours of the instantaneous streamwise vorticity and velocity vectors with absence of the ridges; (b) Contours of the instantaneous streamwise vorticity and velocity vectors with presence of the ridges. Here, the spanwise domain is in between the center and first off-center ridges.

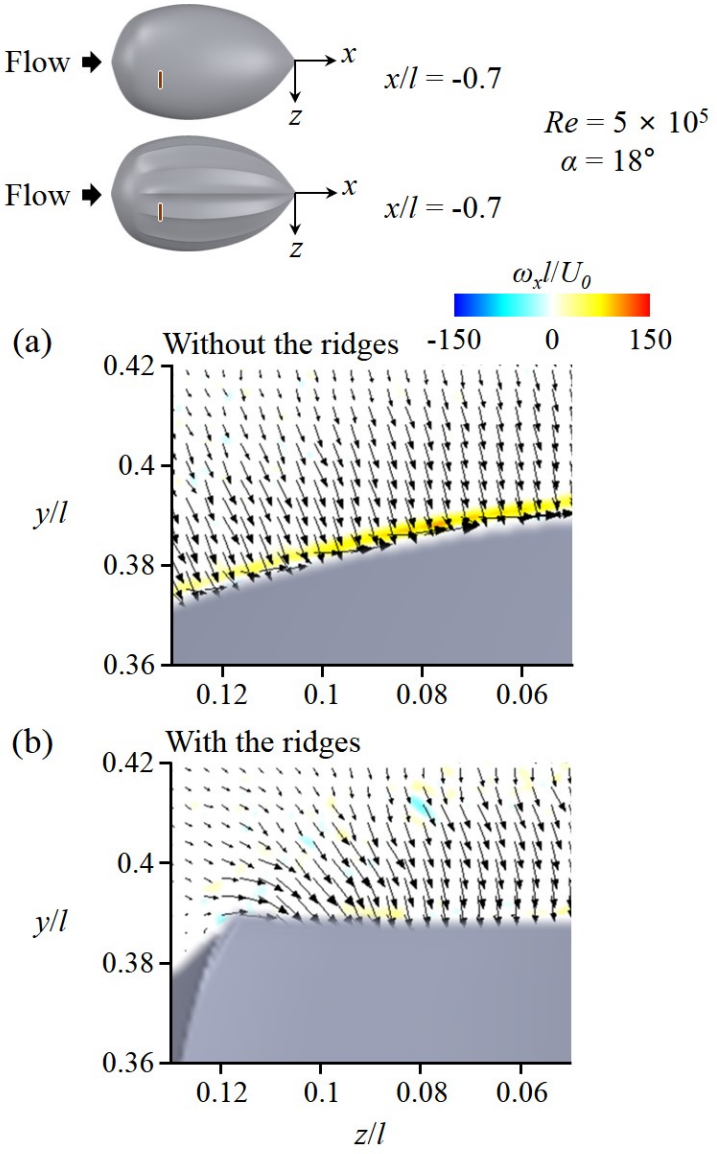

Figure 3.27. Results of flow-field measurements at α=18° and Re=5×10^5 that represents the active ascending swimming of adults (x/l=-0.7, γ=0°). (a) Contours of the instantaneous streamwise vorticity and velocity vectors with absence of the ridges; (b) Contours of the instantaneous streamwise vorticity and velocity vectors with presence of the ridges. Here, the spanwise domain is in between the center and first off-center ridges.

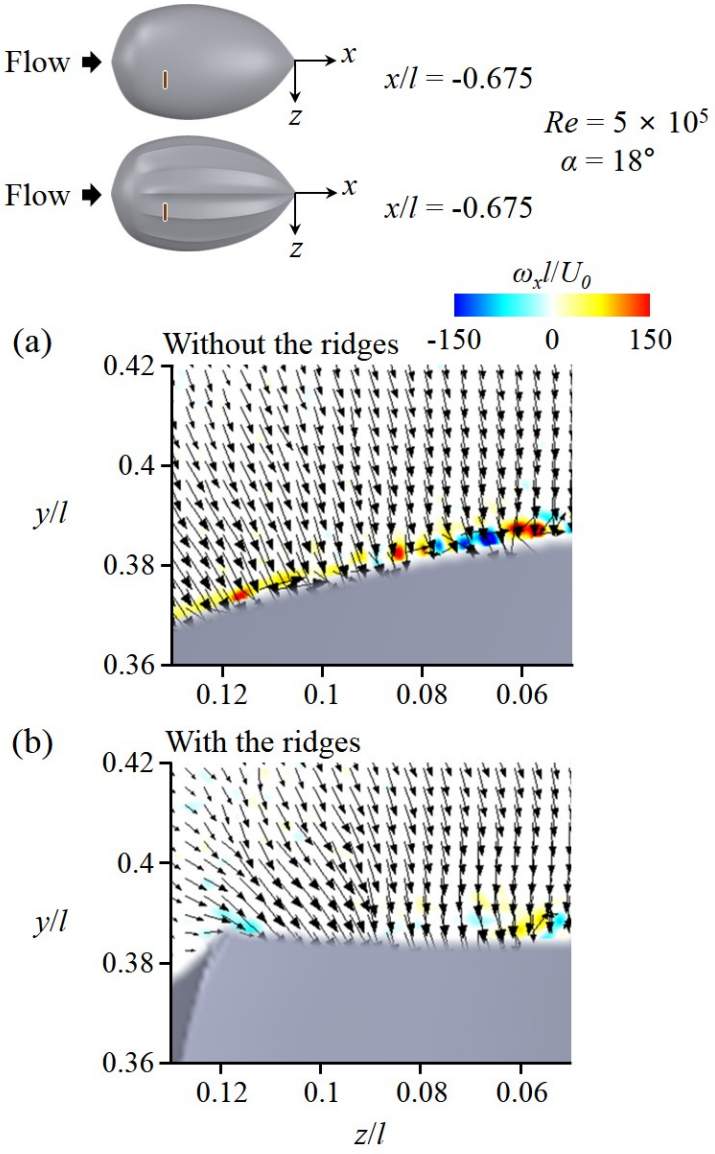

Figure 3.28. Results of flow-field measurements at α=18° and Re=5×10^5 that represents the active ascending swimming of adults (x/l=-0.675, γ=0°). (a) Contours of the instantaneous streamwise vorticity and velocity vectors with absence of the ridges; (b) Contours of the instantaneous streamwise vorticity and velocity vectors with presence of the ridges. Here, the spanwise domain is in between the center and first off-center ridges.

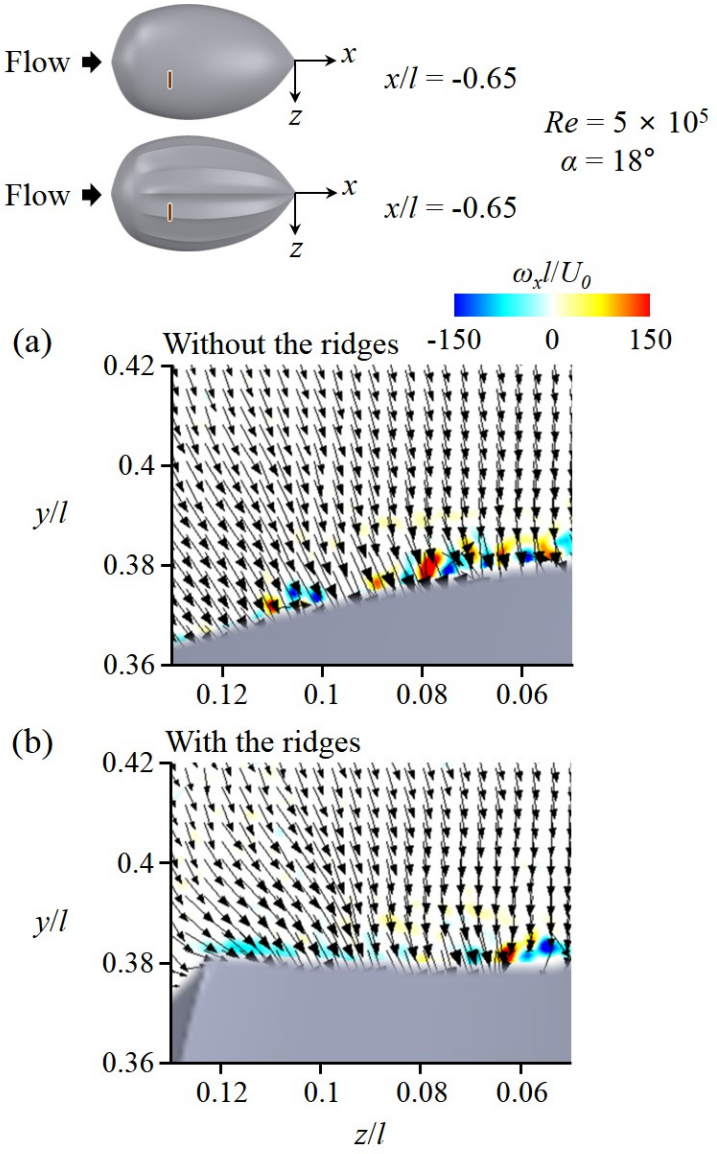

Figure 3.29. Results of flow-field measurements at α=18° and Re=5×10^5 that represents the active ascending swimming of adults (x/l=-0.65, γ=0°). (a) Contours of the instantaneous streamwise vorticity and velocity vectors with absence of the ridges; (b) Contours of the instantaneous streamwise vorticity and velocity vectors with presence of the ridges. Here, the spanwise domain is in between the center and first off-center ridges.

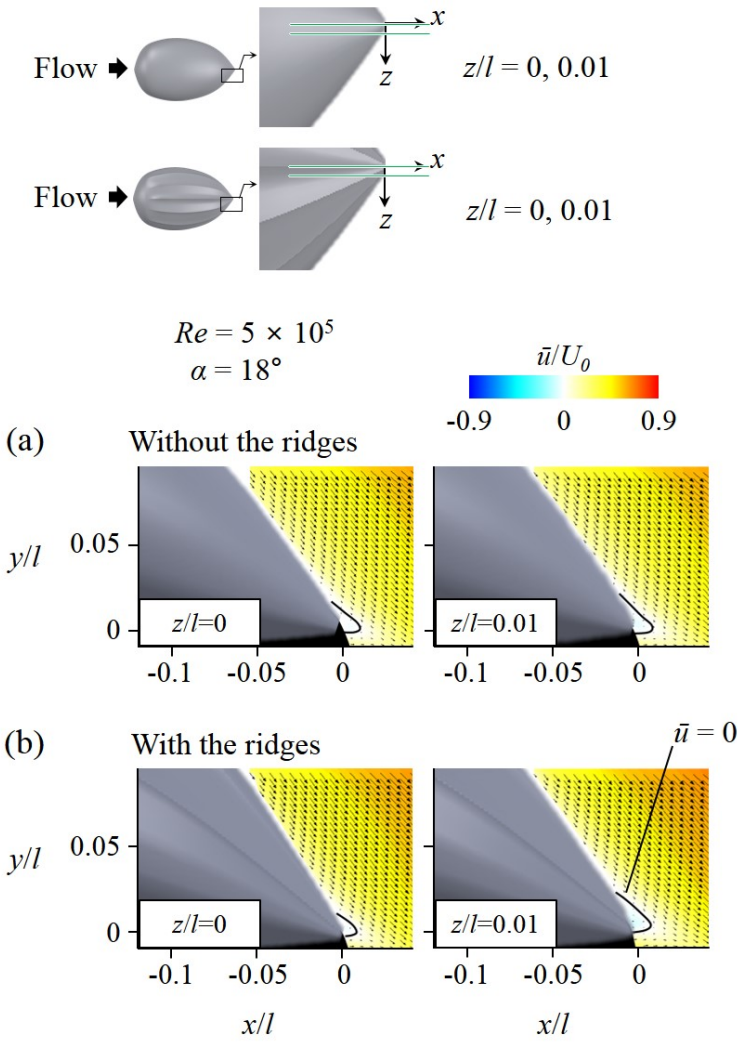

Figure 3.30. Results of flow-field measurements at α=18° and Re=5×10^5 that represents the active ascending swimming of adults (z/l=0 (left panel), z/l=0.01 (right panel), γ=0°). (a) Contours of time-averaged streamwise velocity and velocity vectors at two spanwise locations on the rear part of the model without the ridges; (b) Contours of time-averaged streamwise velocity and velocity vectors at two spanwise locations on the rear part of the model with the ridges.

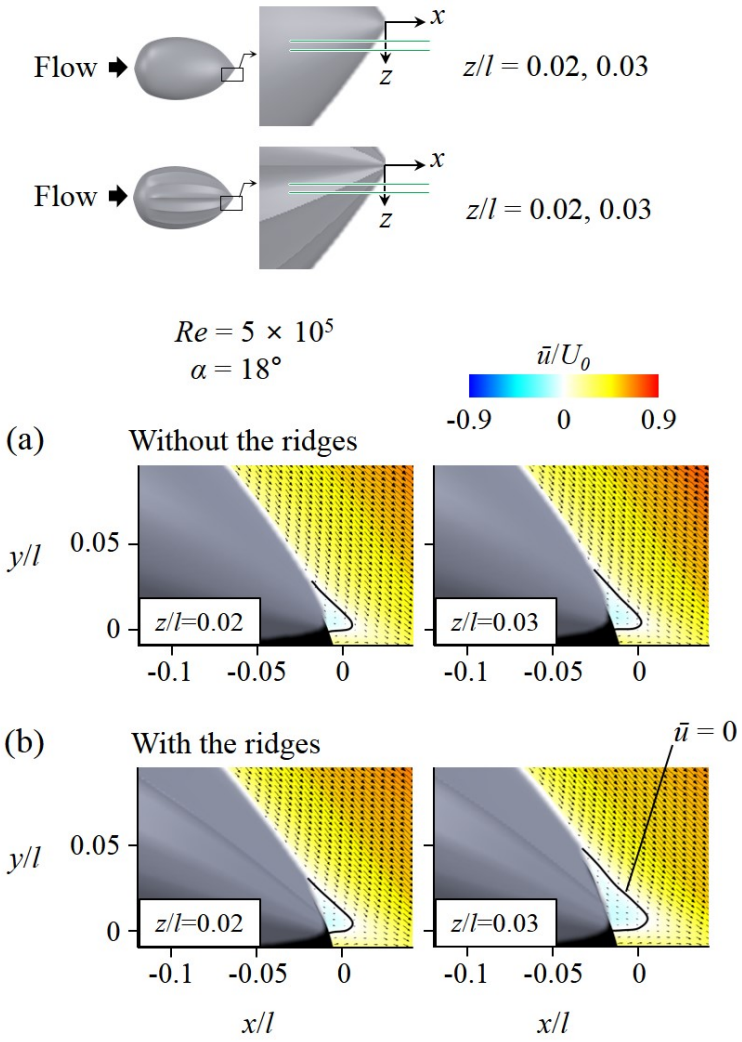

Figure 3.31. Results of flow-field measurements at α=18° and Re=5×10^5 that represents the active ascending swimming of adults (z/l=0.02 (left panel), z/l=0.03 (right panel), γ=0°). (a) Contours of time-averaged streamwise velocity and velocity vectors at two spanwise locations on the rear part of the model without the ridges; (b) Contours of time-averaged streamwise velocity and velocity vectors at two spanwise locations on the rear part of the model with the ridges.

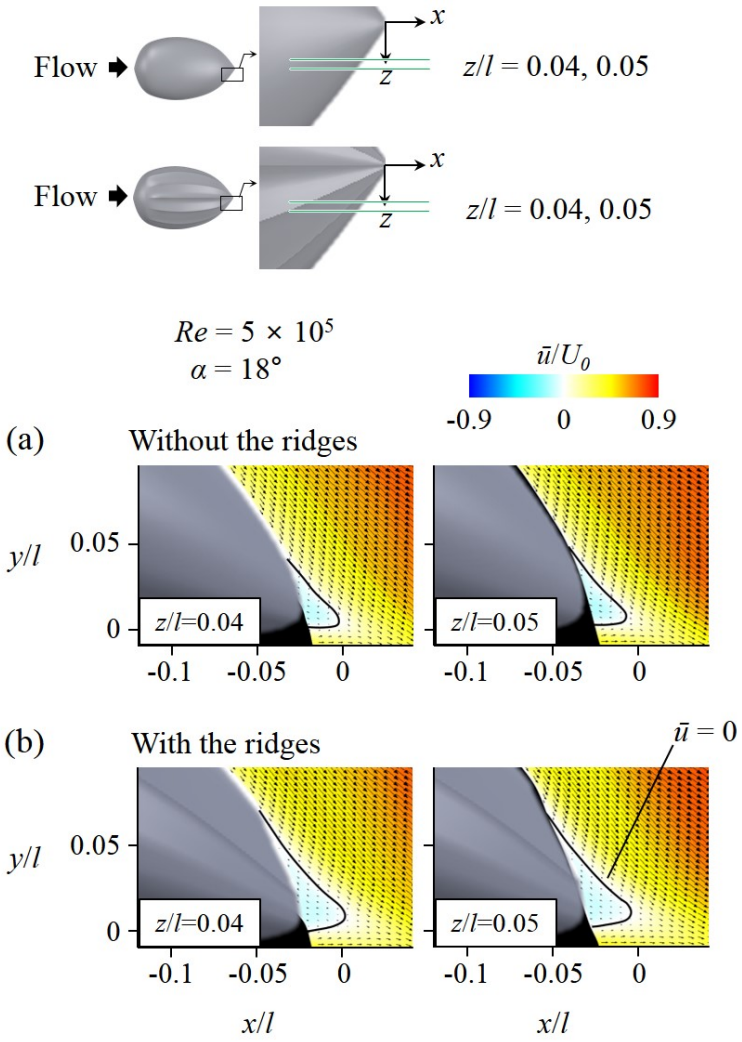

Figure 3.32. Results of flow-field measurements at α=18° and Re=5×10^5 that represents the active ascending swimming of adults (z/l=0.04 (left panel), z/l=0.05 (right panel), γ=0°). (a) Contours of time-averaged streamwise velocity and velocity vectors at two spanwise locations on the rear part of the model without the ridges; (b) Contours of time-averaged streamwise velocity and velocity vectors at two spanwise locations on the rear part of the model with the ridges.

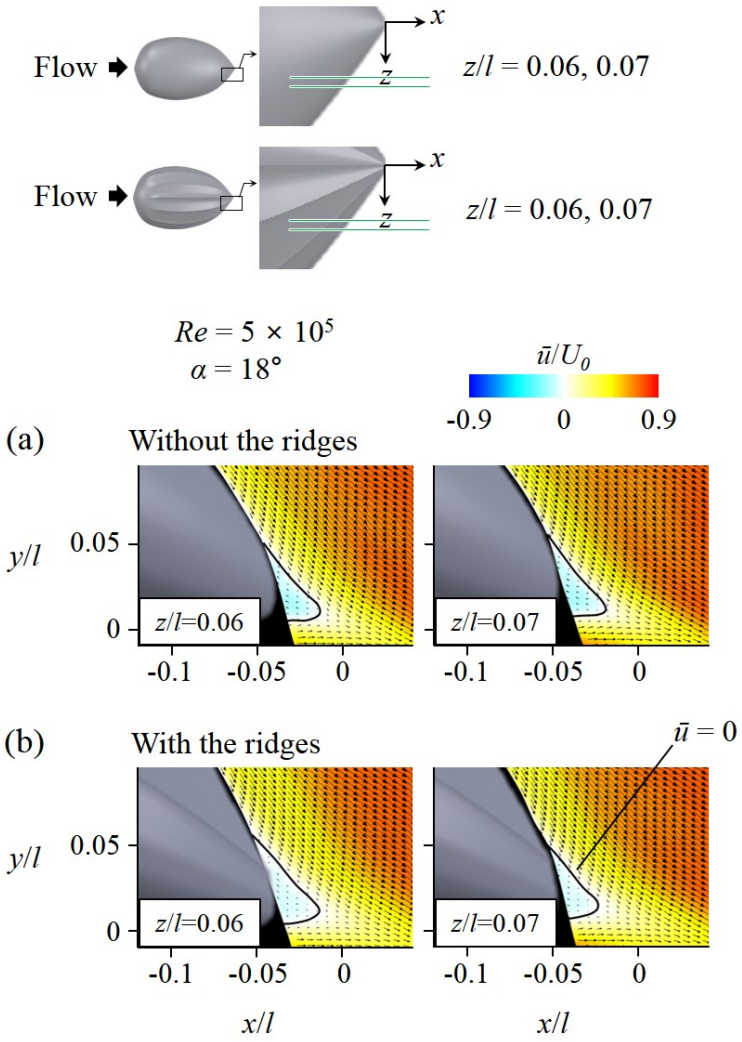

Figure 3.33. Results of flow-field measurements at α=18° and Re=5×10^5 that represents the active ascending swimming of adults (z/l=0.06 (left panel), z/l=0.07 (right panel), γ=0°). (a) Contours of time-averaged streamwise velocity and velocity vectors at two spanwise locations on the rear part of the model without the ridges; (b) Contours of time-averaged streamwise velocity and velocity vectors at two spanwise locations on the rear part of the model with the ridges.

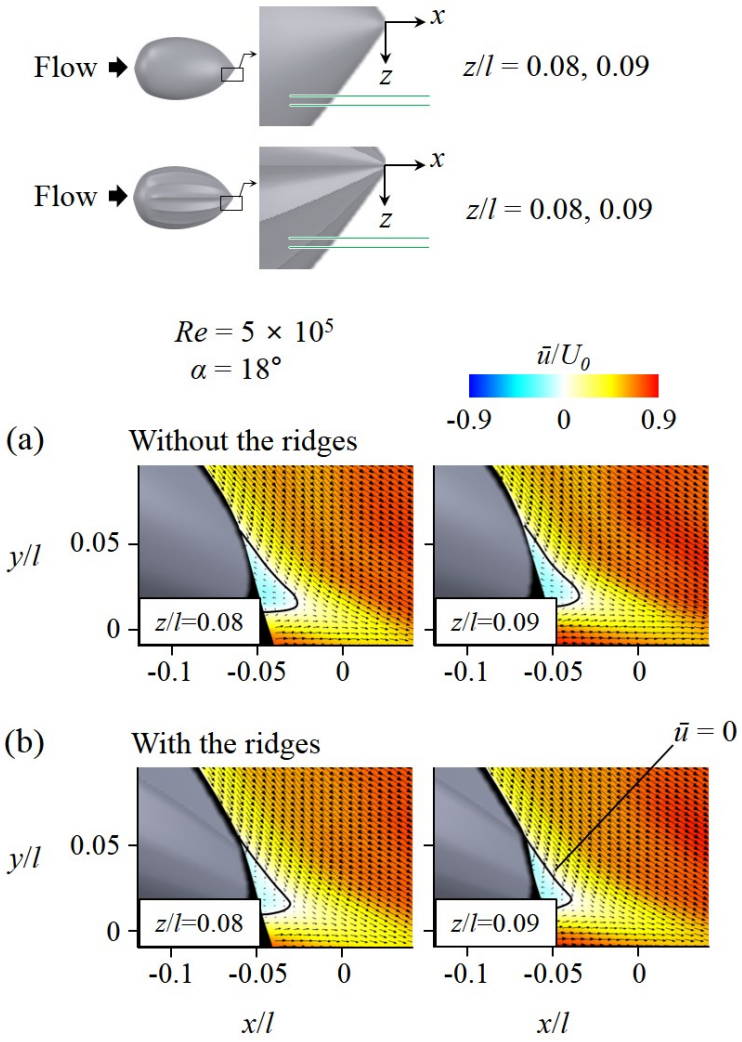

Figure 3.34. Results of flow-field measurements at α=18° and Re=5×10^5 that represents the active ascending swimming of adults (z/l=0.08 (left panel), z/l=0.09 (right panel), γ=0°). (a) Contours of time-averaged streamwise velocity and velocity vectors at two spanwise locations on the rear part of the model without the ridges; (b) Contours of time-averaged streamwise velocity and velocity vectors at two spanwise locations on the rear part of the model with the ridges.

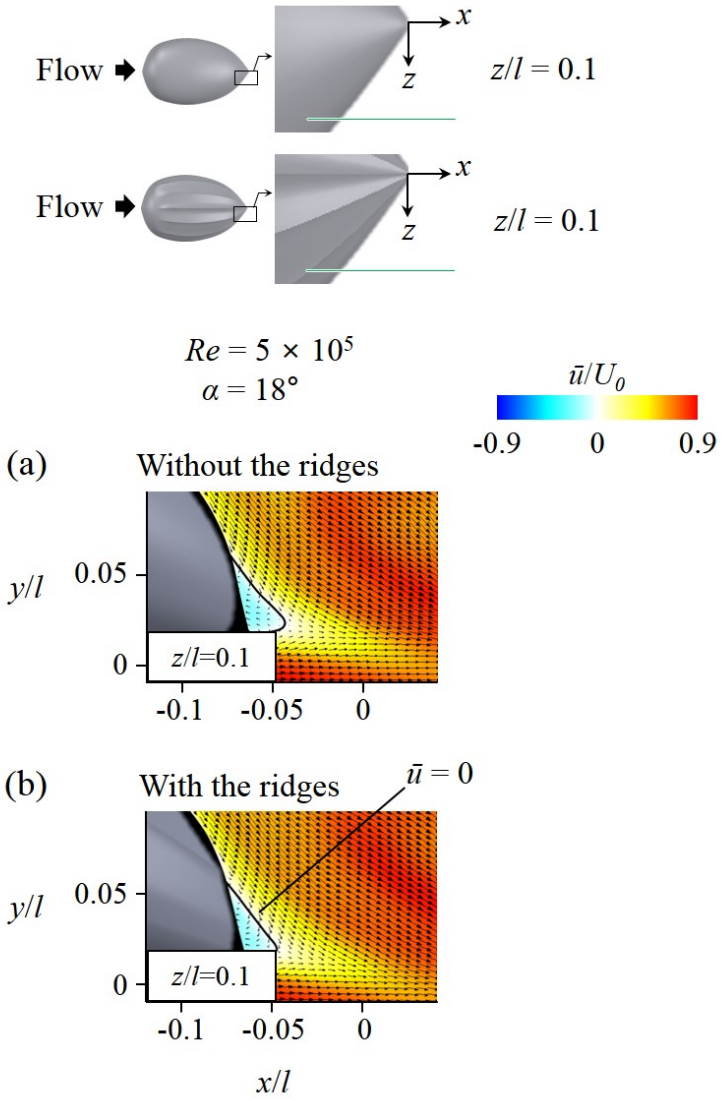

Figure 3.35. Results of flow-field measurements at α=18° and Re=5×10^5 that represents the active ascending swimming of adults (z/l=0.1, γ=0°). (a) Contours of time-averaged streamwise velocity and velocity vectors on the rear part of the model without the ridges; (b) Contours of time-averaged streamwise velocity and velocity vectors on the rear part of the model with the ridges.

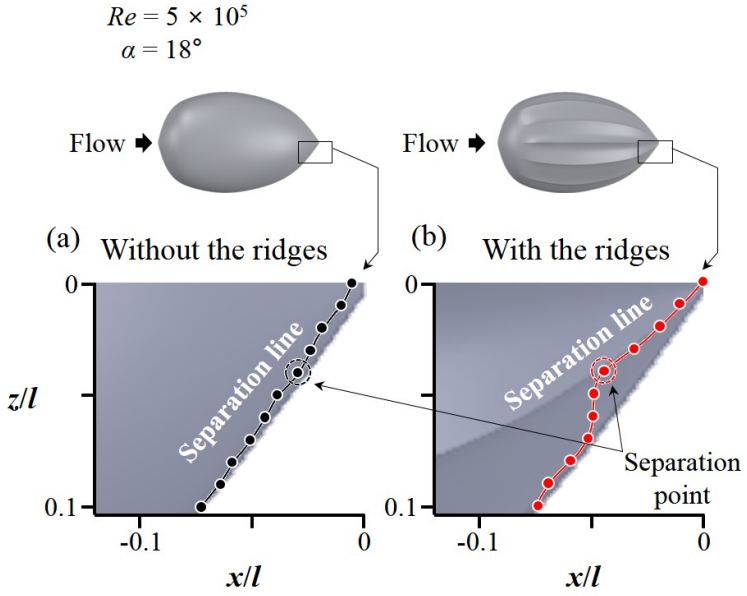

Figure 3.36. Separation lines on the rear part of the model. (a) Separation line with absence of the ridges; (b) Separation line with presence of the ridges. These lines are drawn from the velocity fields measured at eleven spanwise locations and detailed information is given in Fiugre 3.30 - 3.37.

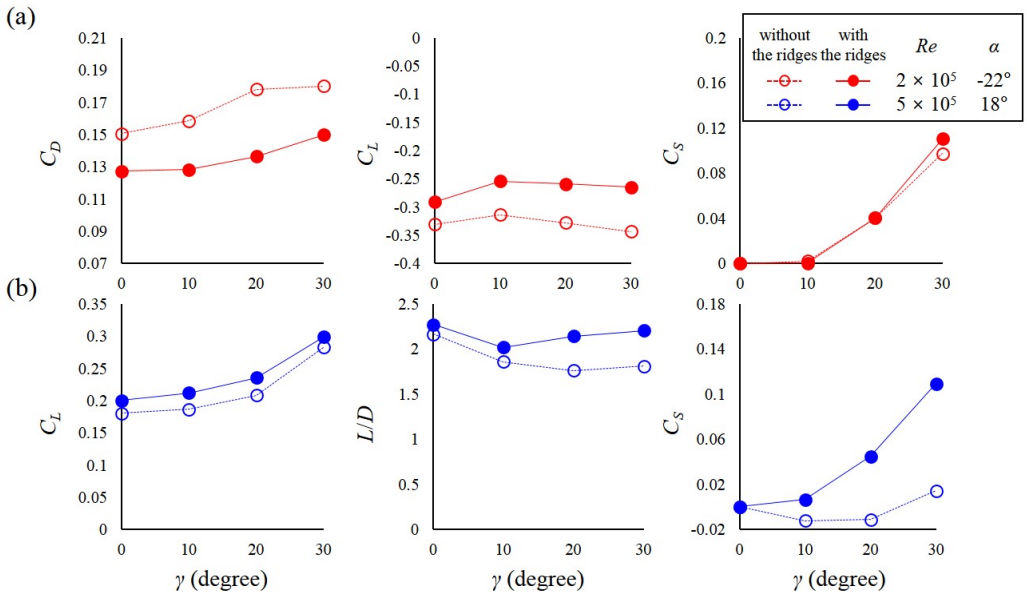

Figure 3.37. Variations of the drag (C_D), lift (C_L), and side force (C_S) coefficients with the yaw angle. (a) Vigorous swimming of hatchlings; (b) Active ascending swimming of adults.

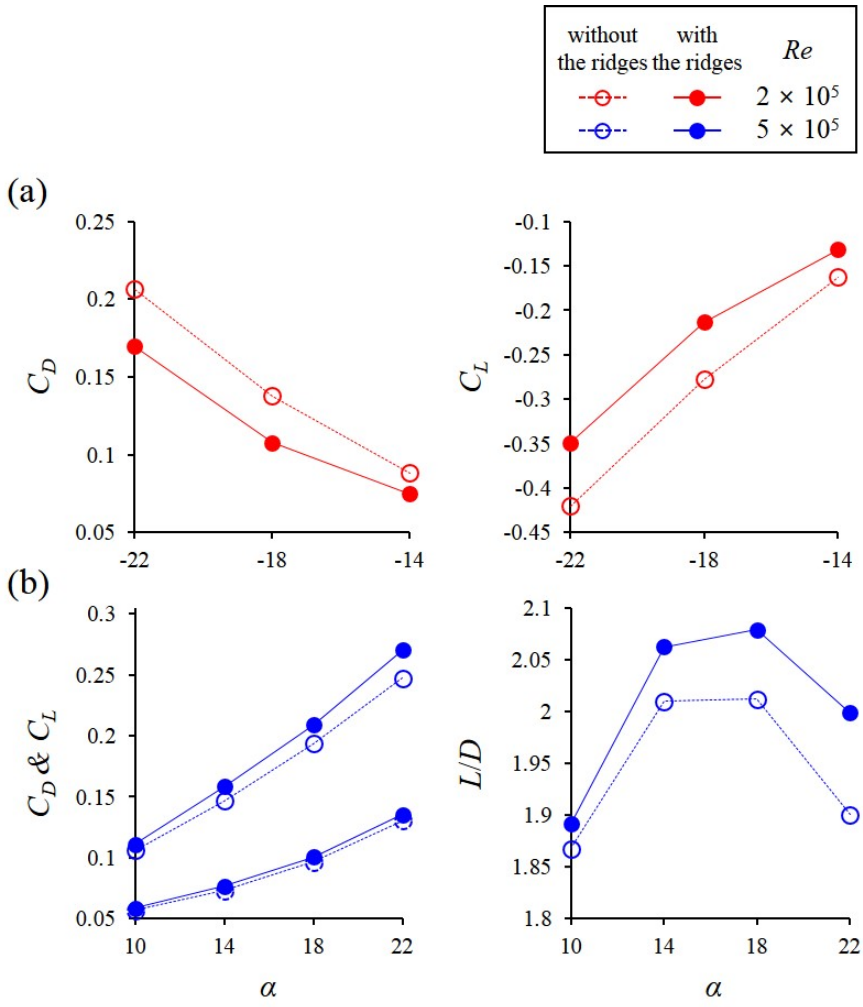

Figure 3.38. Force measurements on the carapace models with the head (γ=0°). (a) Vigorous swimming of hatchlings; (b) Active ascending swimming of adults.

Chapter 4

Summary and Concluding Remarks

The present results are the first experimental evidence about the hydrodynamic roles of the longitudinal ridges in leatherback turtle swimming. The ridges functioned differently depending on the flow conditions: (1) they significantly reduced the drag forces at negative angles of attack and relatively low Reynolds numbers that represents a vigorous swimming performed by hatchlings; (2) at positive angles of attack and relatively high Reynolds numbers, corresponding to an active ascending swimming of adults in V-shaped diving, the ridges enhanced both the lift and lift-to-drag ratio. Our DPIV results provided explanations on how the ridges enhanced the hydrodynamic performances for these two swimming conditions. The longitudinal ridges that are misaligned with local streamlines generated local flow separation, which in turn induced a shear layer instability and produced streamwise vortices (therefore, unlike the conjectures by Deraniyagala (Deraniyagala, 1936) and Hendrickson (Hendrickson, 1980), the role of ridges is not to keep the flow over the carapace laminar). These streamwise vortices delayed or suppressed flow separation, resulting in both drag reduction for the vigorous swimming of hatchlings and lift enhancement for the active ascending swimming by adults. Other morphological features, such as dorsal and ventral keels of a boxfish (Bartol *et al.*, 2002, 2003, 2008), tubercles on the leading edge of a humpback whales flipper (Miklosovic *et al.*, 2004; Fish & Lauder, 2006; Pedro & Kobayashi, 2008), an

alula on the leading edge of a magpies feather (Lee *et al.*, 2015), and a serrated leading edge of an owls feather (Anders, 2000; Choi *et al.*, 2012), have shown aero- and hydrodynamic roles similar to that of the longitudinal ridges, in that they generate streamwise vortices and increase the aero- and hydrodynamic performances. However, there also exist notable differences between those cases and the present one. That is, those morphological features exist only at the frontal parts of the body, flipper and wing, and thus most of them work only at limited situations like at high angles of attack for lift enhancement. On the other hand, the longitudinal ridges exist along the entire body and function differently depending on the swimming conditions: i.e., the ridges reduce the drag at negative angles of attack by controlling the flow at the rear part of the body, and increase the lift at positive angles of attack by controlling the flow at the frontal part of the body. Our study therefore reveals a natures solution, i.e., the longitudinal ridges that are slightly misaligned to local streamlines, for flow control on a teardrop-shaped body at negative to positive angles of attack. These ridges are also contrary to a general intuition that a streamlined body shape is advantageous in decreasing the drag. Our results suggest that the hydrodynamic performance can be optimized even with the features that are not streamlined. We expect that the longitudinal surface protrusions slightly misaligned with local streamlines may provide an innovative design concept for vehicles with better hydro- and aerodynamic performances.

Part II

Development of a bio-mimetic concept car design

with low aerodynamic drag

Chapter 5

Introduction

The rapid increment of crude oil hit the global world and the timing of depletion of petroleum resources is approaching, there is growing need to reduce fuel consumption in automobiles. Many companies make efforts to improve fuel efficiency to reduce fuel consumption in automobiles, and international environmental regulations are also being strengthened for reducing greenhouse gas emissions. Reducing the aerodynamic drag by applying aerodynamic research to automobile development is one of effective ways to enhance fuel efficiency. Hucho and Sovran (Hucho & Sovran, 1993) suggested that the aerodynamic drag makes up 46% of fuel consumption for a midsize car in highway driving. Furthermore, McCallen *et al* (McCallen *et al.*, 1999) reported that a typical modern tractor-trailer possessing the drag coefficient of 0.6 takes 65% of the total fuel consumption to overcome the aerodynamic drag. Therefore, they suggested that the drag reduction of a typical tractor-trailer from 0.6 - 0.3 would result in a 43% fuel savings. Many companies have been trying to improve the aerodynamic performance of their cars for a long time. Figure 5.1 shows the distribution of drag coefficients for a number of automobiles developed from the 1920s to the present. This figure shows that the drag coefficient of the vehicle has gradually decreased with time. However, in the case of passenger cars marked with black circles, it can be seen that the drag coefficient of automobiles has been steadily decreasing in the past 1970s to 1980s, however recently

it has become stagnant. This phenomenon means that the shape optimization method, which was traditionally used as a drag reduction strategy, has reached its limit in recent year. Therefore, we need to establish a new strategy for drag reduction of automobiles.

Bio-mimetic engineering is an innovative approach to solve engineering problems by mimicking the appearance, structure, and working principles of living creatures and applying them to engineering applications (Choi *et al.*, 2012). As examples of applying this approach to vehicle development, Mercedes-Benz has developed a concept car (Bionic) with very low aerodynamic drag by mimicking the shape of a box fish. Another interesting bio-inspired flow control device is from the secondary feathers of a bird's wing. This bio-mimetic flow control device has been applied to an airfoil (Liebe, 1979) and Ahmed body (Kim *et al.*, 2016) and succeeded to improve the aerodynamic performance of the models.

In this study, I suggest the logitudinal ridges of a leatherback turtle as a new bio-mimetic flow control device for aerodynamic performance enhancement of an automobile. The leatherback turtles are the largest and fastest turtles in the world. Through wind tunnel experiments using a leatherback turtle model, I found that the five longitudinal ridges on their back generate streamwise vortices and delay the flow separation on the surface, resulting in drag reduction (upto 32%). Therefore, from this conceptual approach, the purpose of this study is to develop a new bio-mimetic concept car design with low aerodynamic drag by applying the ridge shape of a leatherback turtle to an automobile design.

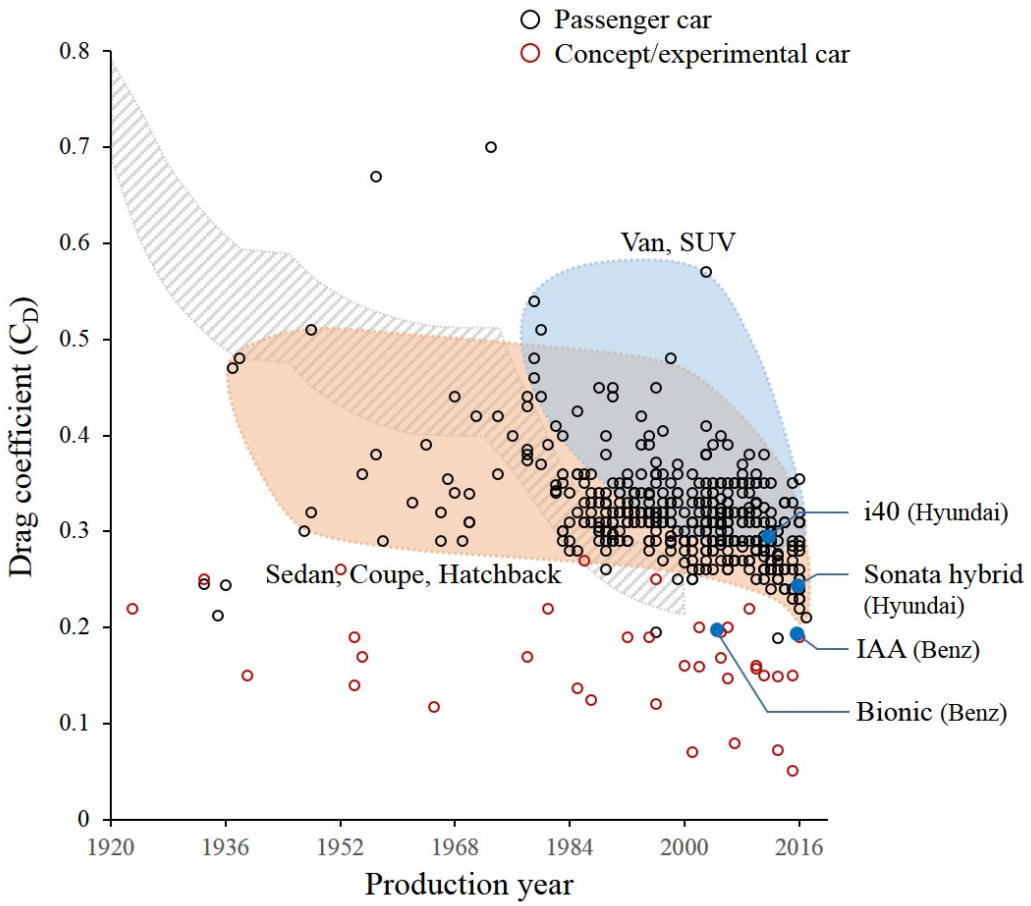

Figure 5.1. Aerodynamic drag distribution of various automobiles with respect to production year.

Chapter 6

Experimental Set-up

6.1 Target model

The drag coefficient distribution in Figure 5.1 shows that the drag coefficients of automobiles having relatively large l/h such as sedans or hatchbacks are typically smaller than those of vans or SUVs having relatively small l/h. In other words, the length-to-height ratio (l/h) of the automobile greatly affects the drag characteristics of the automobile. Therefore, I selected the target model of this study based on the length-to-height ratio (l/h) of the automobile. Figure 6.1 shows the distribution of the drag coefficients according to the length-to-height ratio of several cars. By comparing the case of the leatherback turtle model (l/h of the leatherback turtle model is 3.3), Figure 6.1 shows that Sonata hybrid (l/h=3.3), Genesis (l/h=3.36), and I40 (l/h=3.28) (made by Hyundai motors) have similar values. In the case of the sedan (i.e. Sonata hybrid, Genesis), the slant angle of the rear glass is low, thereby the flow separation is rarely appeared on that region. Therefore, the longitudinal ridges of the leatherback turtle may not be suitable for expecting a good effect. On the other hand, in the case of the hatchback (i.e. I40), the slant angle of the rear glass is relatively large, thereby this type has a higher probability of flow separation on the rear surface of the body. Therefore, it can be expected that if the ridges are applied to this case, the drag reduction can be achieved by delaying flow separation on

the rear surface of the body. For these reasons, the I40 model is selected as the target model in this study.

Since the cross-section of the wind tunnel is 900 mm (horizontal direction) × 835 mm (vertical direction) when the end-plate is installed, the full-scale model of the automobile can not be used. Therefore, the experiment model should be constructed by reducing the size with considering the blockage ratio of the cross-sectional area. The experiment model is constructed in a 1/8.28 scale by 3D printing. The size of the model is 577 mm in length, 250 mm in width, and 154 mm in height and 32987 mm^2 in cross section (Figure 6.2). The blockage ratio of the cross-sectional area of the model to the test-sectional area is 4.4%. Considering that the maximum free-stream velocity of the wind tunnel is 60 m/s, thereby it is possible to measure by up to 20% of the full-scale Reynolds number ($Re_{h,full}$=2,500,000 (U_0=100 kph)) by using this experiment model.

As a preliminary study on the development of the concept-design through the application of the ridges, additional measurements are conducted for the absence of attached devices such as side mirrors and rear-top deflector to investigate the flow characteristics around the vehicle shape. For this purpose, the side mirrors and rear-top deflector are designed to be removable, respectively.

6.2 Development of concept car design

Figure 6.3 shows the schematic diagram of the design process of the concept-model drawings. In order to design a concept-model shape resembling the appearance of the leatherback turtle, a concept-model surface shape is constructed using a weighting factor between the surface shape of the target model (I40) and the surface shape of the leatherback turtle model. The weighting factor is selected differently depending on the spanwise location. To emphasize the

shape of first and second off-center ridges, the weighting factor on the surface of the leatherback turtle shape is larger at z/h=0.2 - 0.6 because the first and second off-center ridges have an important role in flow control (see Figure 3.9). On the other hand, weighting factor on the surface of the target model shape has larger value at z/h=0.6 - 0.8 to emphasize the shape of the target model at this region. Then, near the center region of the model (z/h=0 - 0.2), the weighting factors of the shape of the target model and leatherback turtle model have similar values to each other.

Figure 6.4 shows the top view, side view, and front view of the newly designed concept model and the characteristic area of cross-section of the model. The cross-sectional area of the concept model is 32987 mm^2, which is the same with the cross-sectional area of the target model (I40 model).

6.3 Wind-tunnel measurements

Figure 6.5 shows the schematic diagram of the present experimental set-up, consisting of a closed-type wind tunnel, target model, end-plate, supporter and load cell. The cross-section of the wind tunnel after contraction is 900 mm $\times$ 900 mm and the maximum wind speed at the test section is 60 m/s. End-plate is installed in the test section to reduce the effect of the boundary layer on the wind-tunnel floor. The target model is installed at 1/4 point in the streamwise direction and 1/2 point in the spanwise direction of the test section. The blockage ratio of the cross-sectional area of the target model to the test-sectional area is 4.4%, which is below the critical value ensuring negligible blockage effect according to Achenbach (Achenbach, 1974). To minimize the disturbance from the supporter, its cross-section is designed to be an ellipse with a ratio of jajor to minor axis of 2.

The drag (D) and side (S) forces on the car models are measured with various Reynolds numbers (Re) and yaw angles (γ). The yaw angles (angle between the free-stream direction and the longitudinal direction of the model) are 0° - 30°, and the free-stream velocity (U_0) varies from 15 to 45 m/s, corresponding to the Reynolds numbers (Re=$U_0 h/\nu$) are from 154,000 to 462,000, where h is the height of the target model, ν is the kinematic viscosity of air. The drag (D) and side (S) forces on the models are measured simultaneously with two load cells (A$D LCB03-006M for the drag force and A&D LCB03-003M for the side force) (Figure 6.5). Resolutions of these load cells are 0.006 N and 0.003 N with maximum capacities of 60 N and 30 N, respectively. The signals from these load cells were digitized by an A/D converter (PXI-6259, National Instruments Co.) and sampled for 40 s at a rate of 10 kHz to obtain the mean value. The drag (C_D) and side force (C_S) coefficients are defined as $C_D = D/(0.5\rho U_0^2 A_f)$, $C_S = S/(0.5\rho U_0^2 A_f)$, respectively, where ρ is the air density, and A_p is the frontal area of the model at γ=0°.

Figure 6.6 shows the schematic diagram of a digital particle image velocimetry (DPIV) which I used to obtain the velocity and vorticity fields around the target and concept models. The measurement are performed at γ=0°, Re_h=0°. The DPIV system consisted of an Nd:Yag laser (Dual Power 135-15, Litron), a laser optics (short Mirror Arm, Dantec Dynamics), a pulse generator (IDT USB Timing Hub XS-TH, Integrated Design Tools), a fog generator (F2010, Safex), and a CCD camera mounted with and optical lens (APO MACRO 180 mm F2.8, SIGMA for the streamwise planes, APO MACRO 180 mm F2.8, SIGMA with 1.7× teleconverter, Nikon for the cross-flow planes). The velocity measurements are performed on various planes parallel to the $x-y$ (streamwise) and $y-z$ (cross-flow) planes, respective, where x, y, and z denote the streamwise, vertical, and spanwise direction, respectively, and the origin was located at the

center of the front bottom edge. To obtain the velocity field from recorded images, an iterative cross-correlation analysis was performed with and initial window size of 64 $\times$ 64 pixels and a final interrogation window size of 16 $\times$ 16 pixels. The interrogation window was overlapped by 50%, leading to spatial resolutions of about 0.23 mm ($1.47 \times 10^{-3}h$) on $x - y$ planes and 0.53 mm ($3.43 \times 10^{-3}h$). To obtain the time-averaged flow field, 1,000 pairs of images are collected and processed.

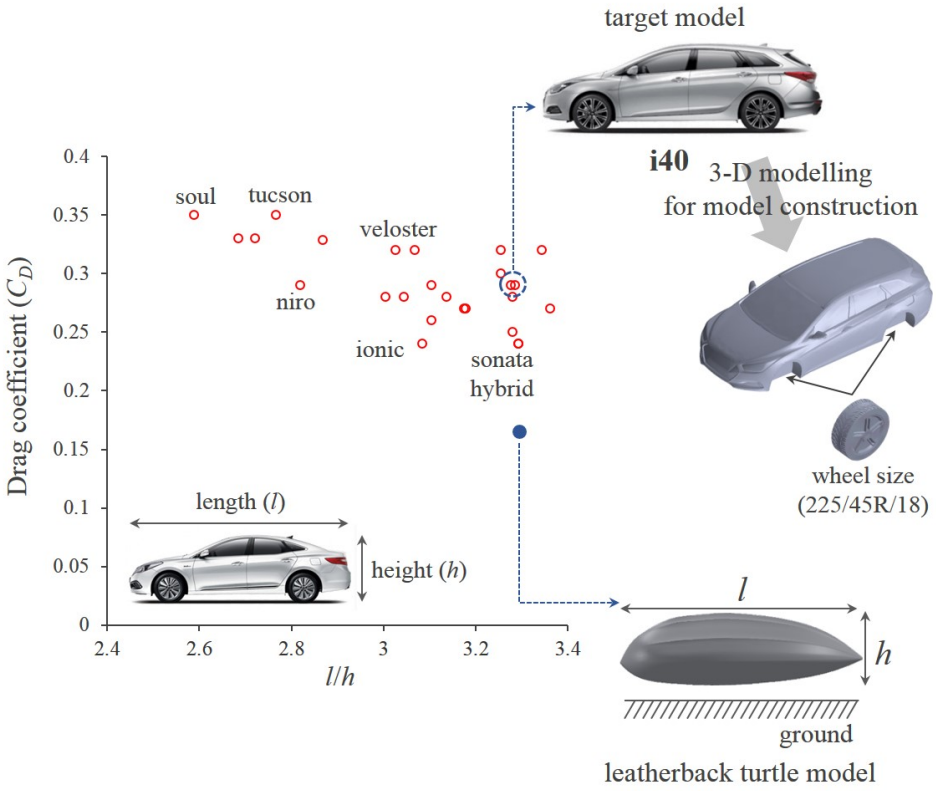

Figure 6.1. Target model selection based on the distribution of drag coefficient according to automobile length-to-height ratio (l/h).

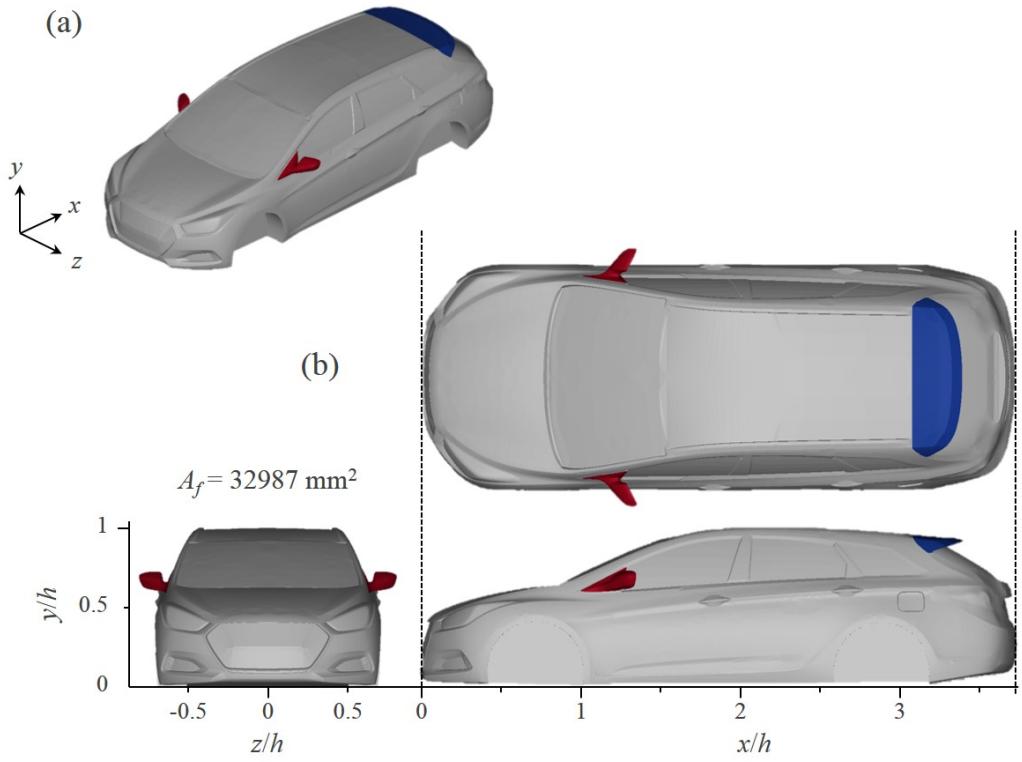

Figure 6.2. Construction of the experiment model based on I40. (a) Perspective view; (b) Top view, side view, and front view of the model and characteristic area of the model.

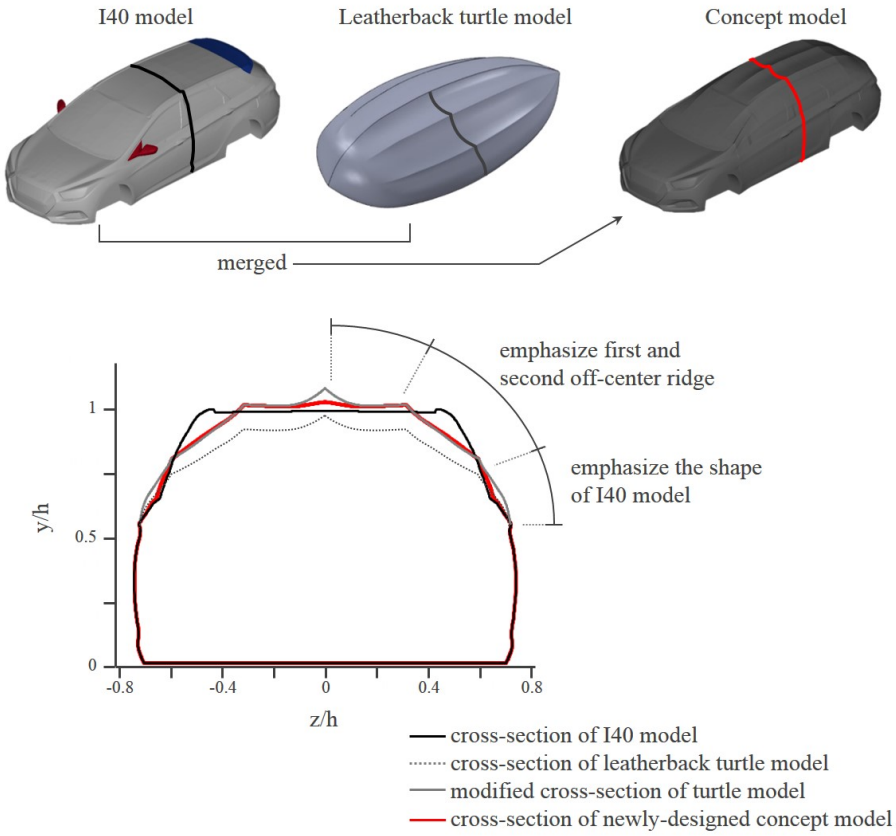

Figure 6.3. Development of concept model based on I40 model and leatherback turtle model.

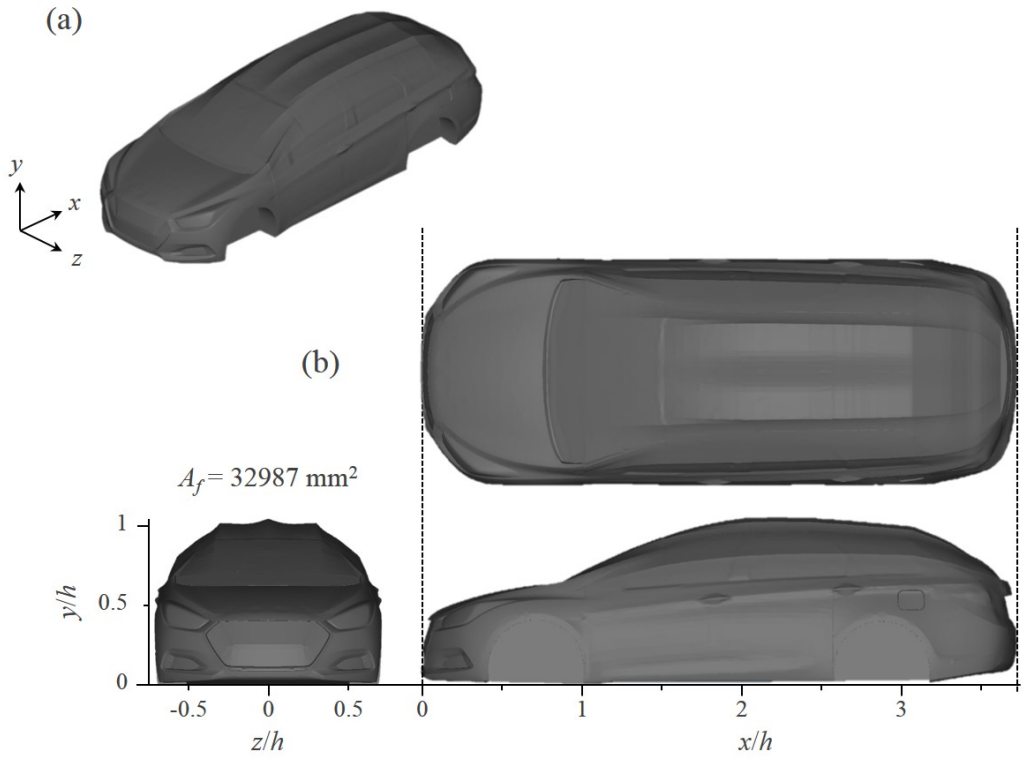

Figure 6.4. Construction of the newly-designed concept model. (a) Perspective view; (b) Top view, side view, and front view of the model and characteristic area of the model.

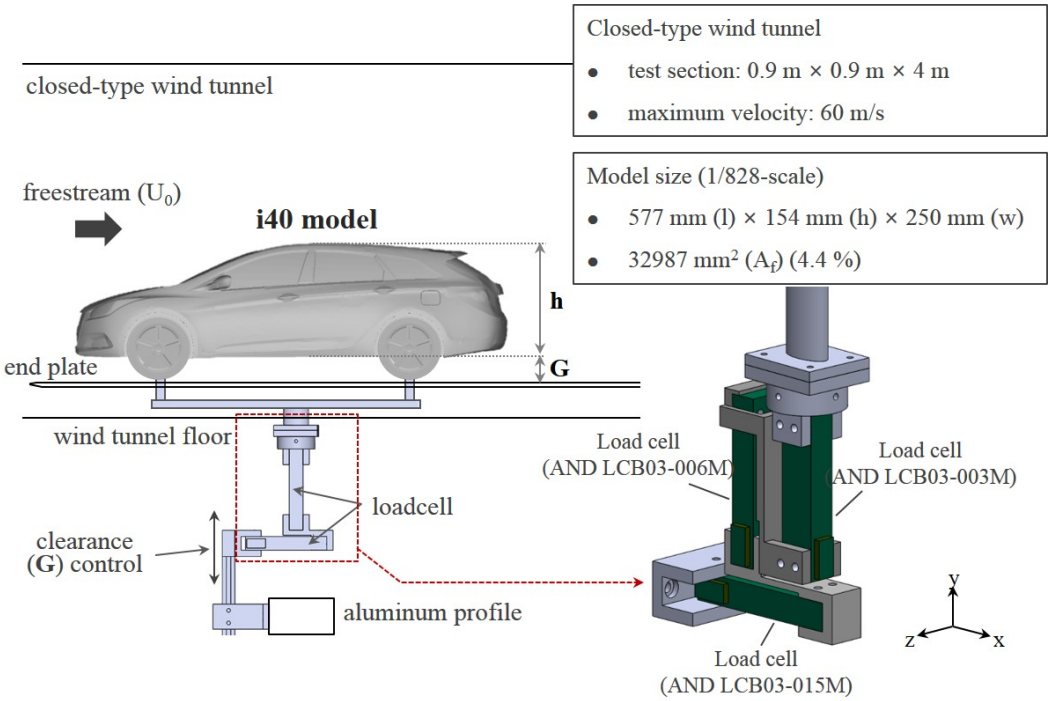

Figure 6.5. Schematic diagram of the experimental set-up for the force measurement and detailed drawing of the force measurement system. Here, h, and G denote the model height, and ground clearance, respectively, and γ is the yaw angle.

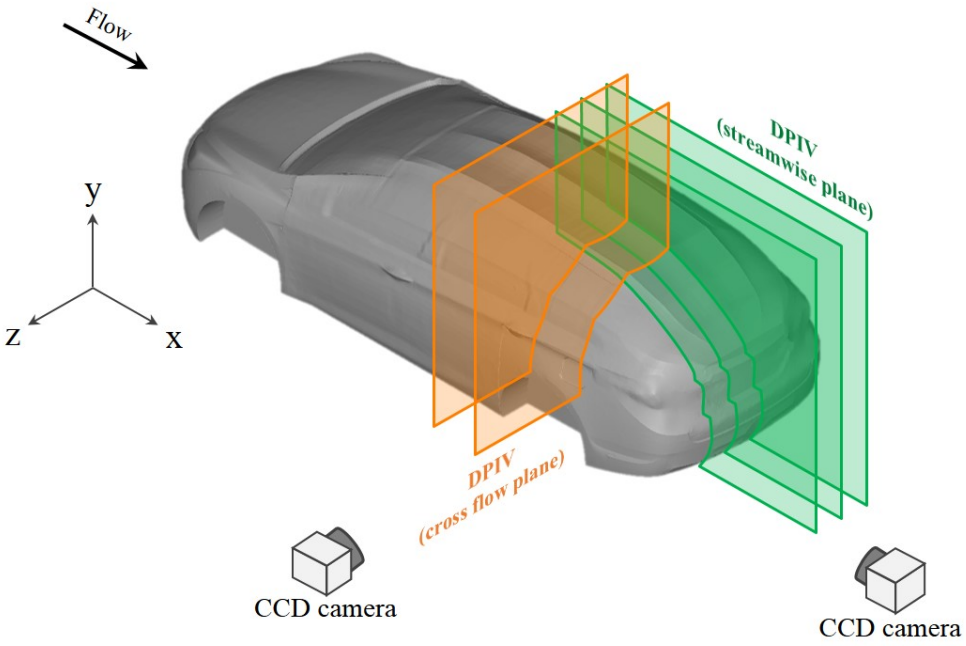

Figure 6.6. Schematic diagram of the experimental set-up for the velocity measurement with DPIV.

Chapter 7

Results and Discussion

7.1 Drag variation on the target model

I conduct a series of wind tunnel tests to measure the drag (D) and side (S) forces on the target (I40) models with and without attached devices (side mirror, rear top deflector). The Reynolds numbers considered are Re_h=154,000-462,000 (based on the model height h) with varying the yaw angle from γ=0° to 30°. Figure 7.1 shows the drag coefficient (C_D; see Experimental set-up (Wind tunnel measurement) for its definition) variations of the target (I40) model with and without side mirrors, with and without rear top deflector. The present drag coefficient of the I40 model shows good agreement with the data provided from the Hyundai motors.

The drag coefficients of the models without side mirror (dark blue symbol (without deflector) and dark gray symbol (with deflector) in Figure 7.1) are lower about 0.01 compared to those of the models with side mirrors (light blue symbol (without deflector) and light gray symbol (with deflector) in Figure 7.1). This result shows that a pair of side mirrors have an effect of increasing the drag coefficient of the automobile by about 0.01. On the other hand, in the case of the rear top deflector, the drag coefficients of the models with deflector (dark gary symbol (without side mirror) and light gray symbol (with side mirror) in Figure 7.1) have about 2% lower values compared to those of the models without

deflector (dark blue symbol (without side mirror) and light blue symbol (with side mirror) in Figure 7.1). Therefore, it can be concluded that the rear top deflector has an effect on drag reduction of the automobile by about 2%.

7.2 Drag and side force variations of concept model

Figure 7.2 shows the drag coefficient (C_D) variations of the newly-designed concept model and the I40 models with and without deflector. In this case, side mirrors are removed to invstigate the flow characteristics of the models themselves. This figure demonstrates that the drag coefficients on the concept model show noticeably lower values compared to those of the I40 models with and without deflector. The values of drag coefficients on the concept model are 4-5% lower than those of the I40 model with deflector and 6-7% lower than those of the I40 model without deflector. The drag reduction effect remain similar throughout the range of Reynolds number (Re_h= 154,000-462,000) in which measurements are conducted.

In the presence of side wind or during cornering motion of an automobile, the moving direction does not coincied with the freestream direction. To examine this effect, the drag and side force measurements are conducted by varying the yaw angle from γ=0° to 30° for both the concept model and the I40 model with the Reynolds number Re_h=154,000-462,000 (Figure 7.3-7.6). Figre 7.3(a) shows that the drag reduction rate (ΔC_D) of the concept model compared to the I40 model with deflector is about 5% at zero yaw angle, and this drag reduction rate is gradually enhanced with increment of the yaw angle (γ) from 0° to 30°. The drag reduction rate of the concept model is about 10% at γ=20° and 13% at γ=30°, respectively. Therefore, it can be seen from these results that the concept model has a more advantage in terms of drag reduction even in the

case where the side wind is strongly blown. In the case of the side force, the side force coefficients (C_S) of the models rapidly increase with increasing yaw angle (Figure 7.3(b)). In this case, the values of the side force coefficient on the concept model are lower than those on the I40 model, and this tendency of side force reduction of the concept model remain similar throughout the range of γ=10°-30°. The side force reduction rate of the concept model is about 17% at γ=20° and 14% at γ=30°, respectively. Therefore, these results surpport that the concept model also has an advantage in terms of side force reduction as well as drag reduction. These results suggest that, unless the yaw angle is very large, the aerodynamic effects of the concept design in terms of the drag and side forces are still similar to those of zero yaw angle. Figure 7.4-7.6 show the drag and side forces variations depending on the yaw angle with higher Reynolds number conditions (Re_h=257,000-462,000). Through these figures, it can be seen that the concept model has drag and side forces reduction effects regardless of the Reynolds number.

7.3 Flow-field measurements on both target and concept model

I conduct a flow visualization using oil-surface visualization (Figure 7.7) and velocity measurements using DPIV (Digital particle image velocimetry), respectively, to investigate the modifications of flow structures on the concept model. From the oil-surface visualization (Figure 7.7), flow separation lines, denoted as dashed red lines, are formed at the rear slanted surface of the models. In the case of the I40 model without deflector, flow separation occurs widely over almost the whole spanwise location (Figure 7.7(a)). On the other hand, in the case of the concept model, separation occurs only locally near the centerline of the rear surface.

To conduct a quantitative analysis about flow fieds, DPIV measurements are performed with three models (I40 model with deflector, I40 model without deflector, and concept model) at γ=0° and Re_h=154,000 in several streamwise and cross-flow planes (see Experimental set-up (Wind tunnel measurement) and Figure 6.6 for the experimental set-up).

Figure 7.8-7.10 show contours of the time-averaged streamwise velocity ($\overline{u}$) and velocity vectors at three spanwise locations (z/h=0, 0.1, and 0.2) for the cases of concept model and I40 model with and without deflector. Here, since the the I40 model without deflector has the largest drag coefficient, I40 model is considered as a no control case. In these figures, sub figure (a) shows the case of I40 model without deflector (no control), sub figure (b) shows the case of concept model, and sub figure (c) shows the case of the I40 model with deflector (see Figure 7.8 for example). In the case of the I40 model without deflector (no control), black solid line, which means the location where $\overline{u}$ is 0, shows that the flow separation is occurred at the rear slanted surface of the model, resulting in the significant pressure drop at this region (Figure 7.8(a)-7.10(a)). Rear top deflector fix the flow separation at the trailing edge of the deflector and make the main separation bubble locate farther downstream than that without deflector, there is a weak reverse flow exists on the slanted surface (Figure 7.8(c)-7.10(c)). On the other hand, in the case of the concept model, the flow separation is almost suppressed and there is no separation at the rear slanted surface of the concept model, resulting in the pressure recovery on the slanted surface (Figure 7.8(b)-7.10(b)). This result is the main reason of drag reduction on the concept model. Figure 7.11-7.13 show flow-fields on the slanted surfaces of the models at the same spanwise locations in Figure 7.8-7.10 to show the separation point and separated flow in more detail.

To understand the mechanism of separation delay on the slanted surface of

the concept model, the contours of instantaneous vorticity and velocity vectors on two cross-flow ($y-z$) planes are drawn in Figure 7.14, 7.15. In the case of the I40 model with and without deflector, there is a counter clock-wise streamwise vortex near the roof edge (Figure 7.14(a),(c), 7.15(a),(c)). This vortical structure is an A-pillar vortex generated form the A-pillar of the model, which causes aerodynamic drag and aeroacoustic noise increment in automobiles (Buchheim *et al.*, 1982). Except for this A-pillar vortex, there is no noticeable vortical structures near the surface of the I40 model (Figure 7.14(a),(c), 7.15(a),(c)). On the other hand, in the case of the concept model, A-pillar vortex is nearly disappeared, and complex vortical structures are formed around the surface of the model (Figure 7.14(b), 7.15(b)). To investigate these vortical structures in more detail, Figure 7.16 shows magnified instantaneous flow structures on the same cross-flow planes with Figure 7.14,7.15 near the first (Figure 7.16(b)), and second (Figure 7.16(a)) off-center ridges. This figure shows that local separated shear layers formed along the ridges generate streamwise vortices, which could supply higher momentum to the flow near the surface, resulting in main separation delay. Therefore, this is the main reaseon of the drag reduction on the concept model which has the ridges on the surface.

To investigate the flow characteristics at the wake region of both models, I conducted PIV measurements behind both models. Figure 7.17-7.22 show contours of the time-averaged streamwise vorticity ($\overline{\omega_x}$) and velocity vectors at six streamwise locations (x/h=3.5 - 4.5) for the cases of the concept model and the I40 model. A clock-wise streamwise vortex which is generated from a C-pillar part of the car model (Figure 7.17, Figure 7.18) is formed behind both models (Figure 7.19-Figure 7.22). This streamwise vortex (C-pillar vortex) is generally known for the major source of the drag increment on an automobile. In this case (I40 model and concept model), the shape of the C-pillar vortex

and the location of the vortex core are similar to each other (Figure 7.19-Figure 7.22). Therefore we can suppose the modification of the C-pillar vortex is not the main reason of the drag reduction on the concept model.

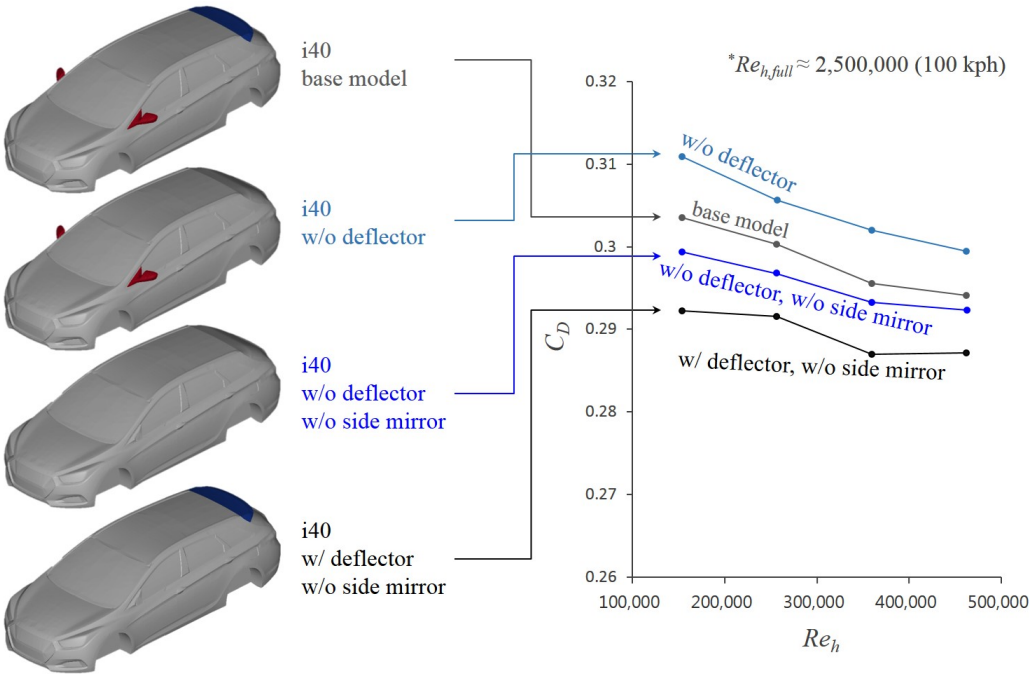

Figure 7.1. Variations of drag coefficient on the I40 model (target model).

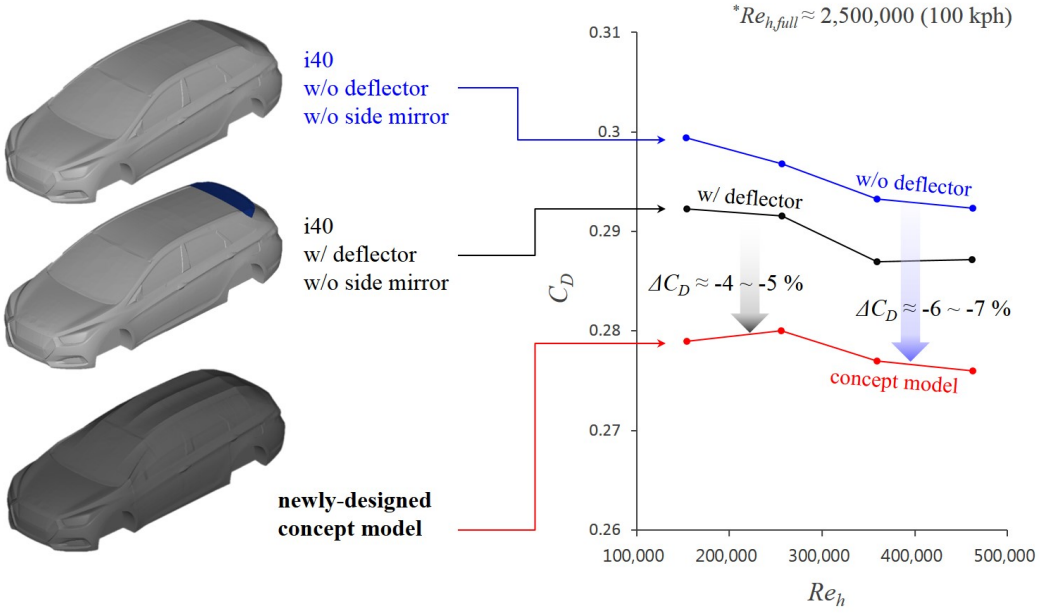

Figure 7.2. Variations of drag coefficient on the I40 model and Concept model (new design).

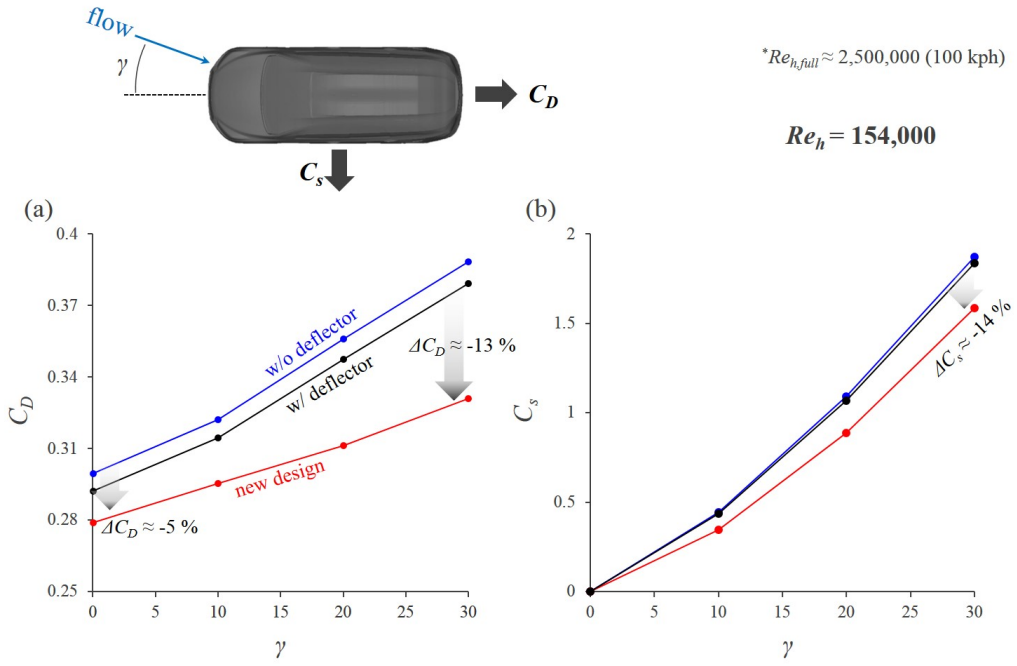

Figure 7.3. Effect of yaw angle variation (γ=0°-30°) on the models at Re=154,000. (a) Variations of drag coefficient depending on the yaw angle; (b) Variations of side force coefficient depending on the yaw angle.

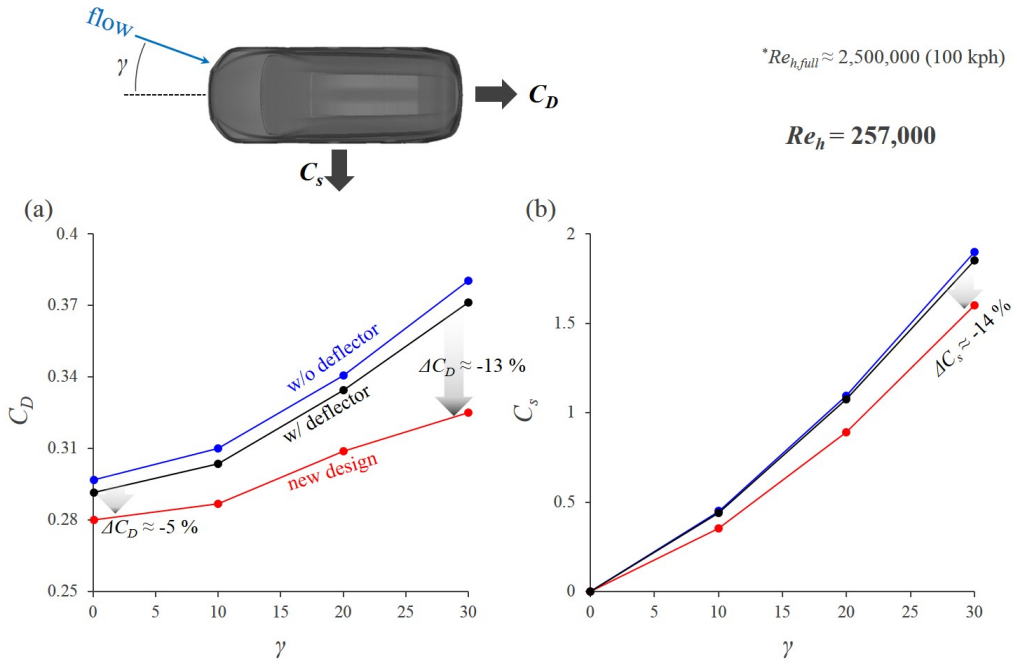

Figure 7.4. Effect of yaw angle variation (γ=0°-30°) on the models at Re=257,000. (a) Variations of drag coefficient depending on the yaw angle; (b) Variations of side force coefficient depending on the yaw angle.

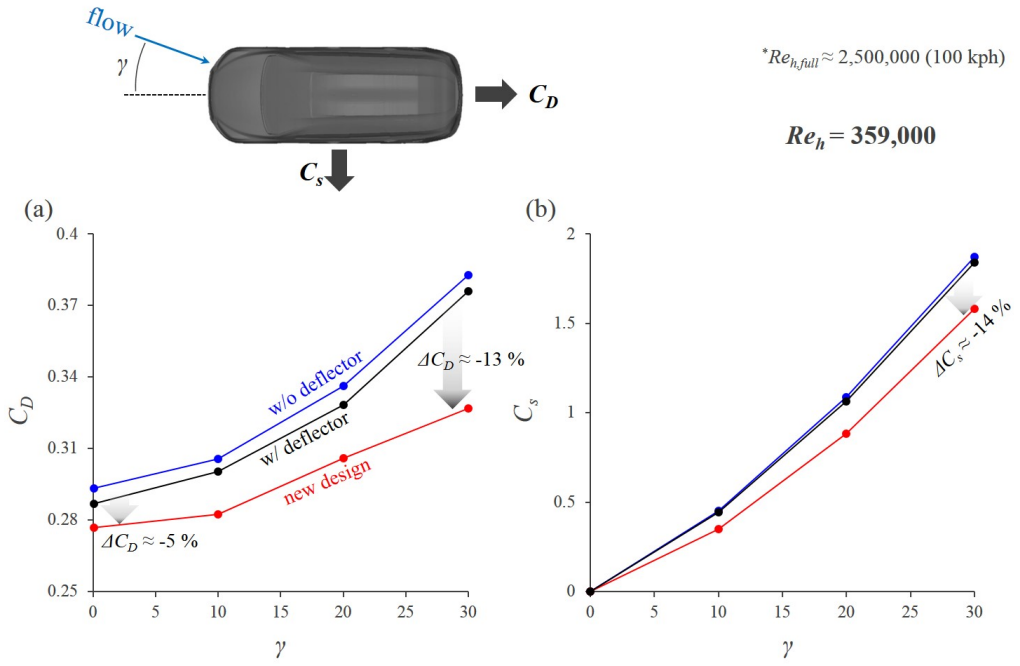

Figure 7.5. Effect of yaw angle variation (γ=0°-30°) on the models at Re=359,000. (a) Variations of drag coefficient depending on the yaw angle; (b) Variations of side force coefficient depending on the yaw angle.

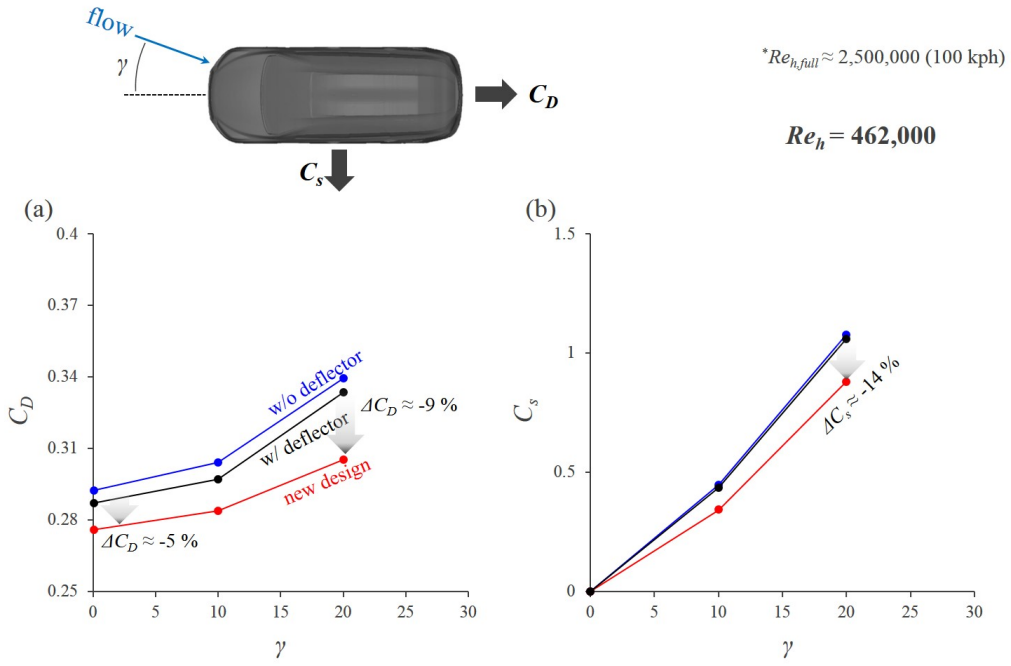

Figure 7.6. Effect of yaw angle variation (γ=0°-20°) on the models at Re=462,000. (a) Variations of drag coefficient depending on the yaw angle; (b) Variations of side force coefficient depending on the yaw angle.

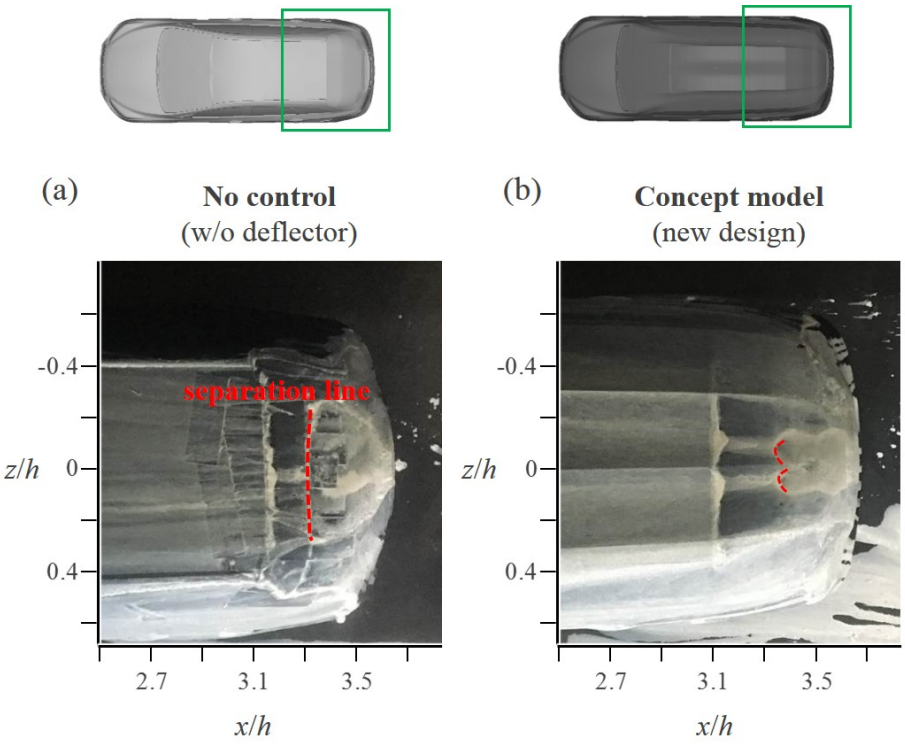

Figure 7.7. Oil-surface visualization on the rear part of the models at Re=154,000, γ=0°. (a) I40 model without deflector (no control); (b) Concept model (new design).

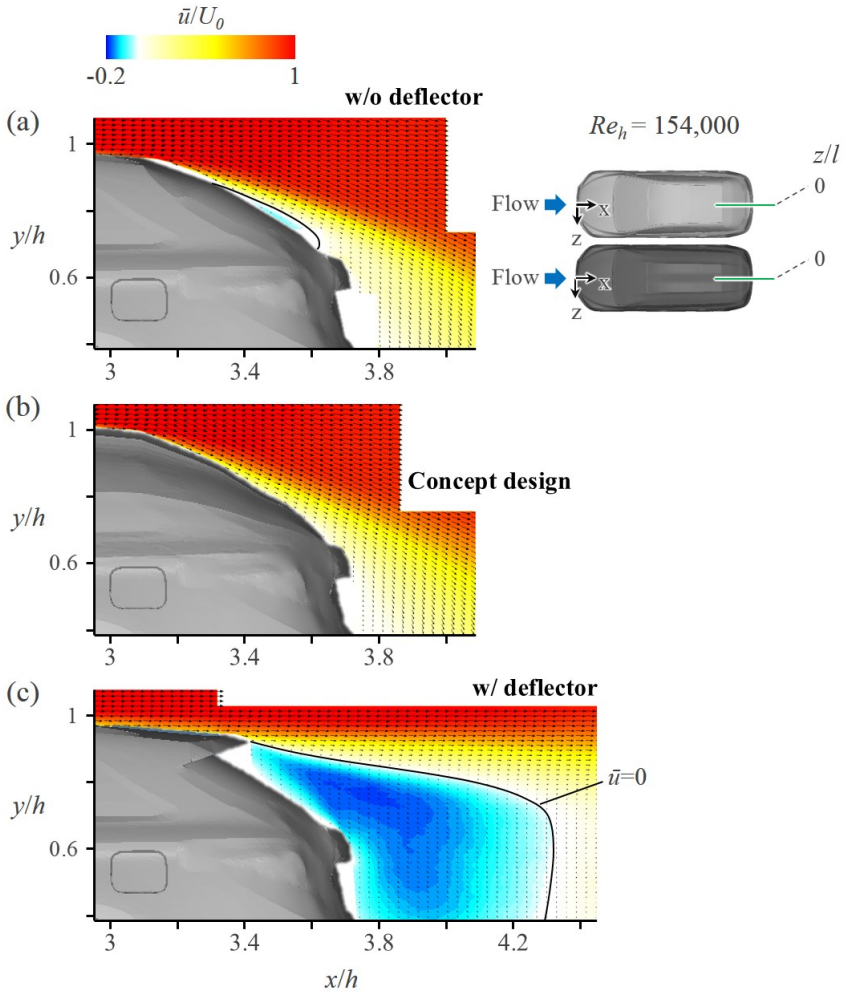

Figure 7.8. Contours of the time-averaged streamwise velocity ($\overline{u}$) and velocity vectors at z/h=0, Re=154,000 (γ=0°). Solid black lines in this figure indicate the locations of $\overline{u}$=0. (a) I40 model without deflector (no cnotrol); (b) Concept model (new design); (c) I40 model with deflector.

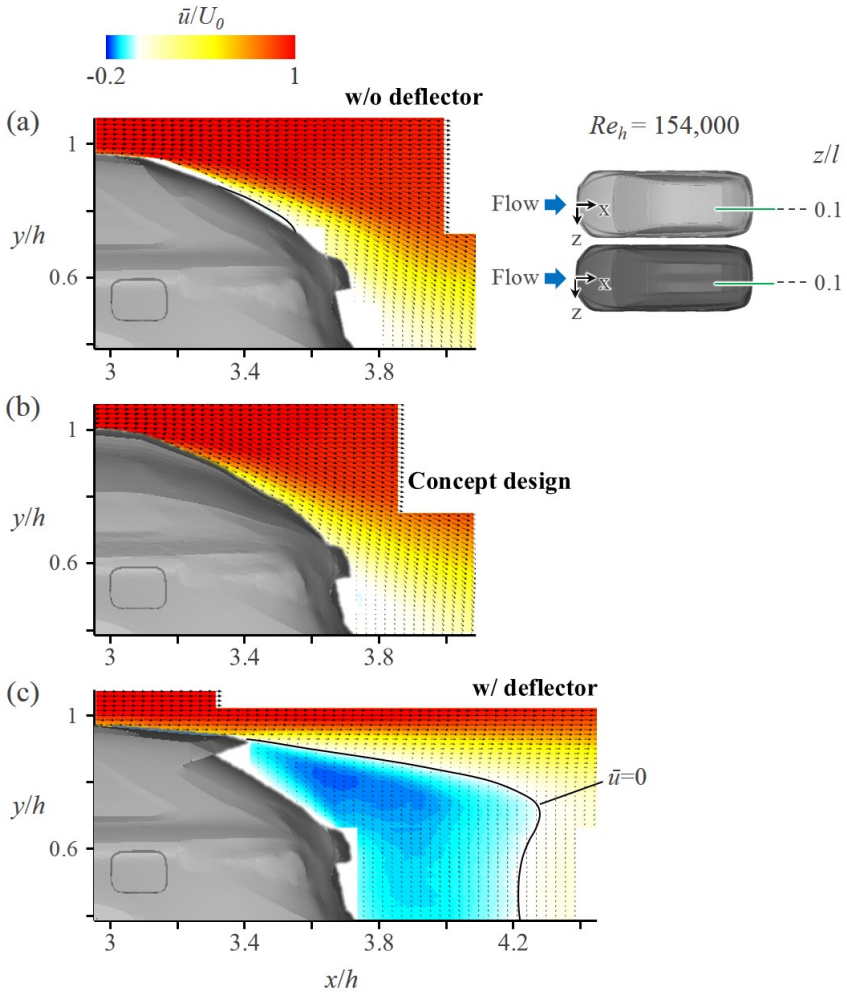

Figure 7.9. Contours of the time-averaged streamwise velocity ($\overline{u}$) and velocity vectors at z/h=0.1, Re=154,000 (γ=0°). Solid black lines in this figure indicate the locations of $\overline{u}$=0. (a) I40 model without deflector (no cnotrol); (b) Concept model (new design); (c) I40 model with deflector.

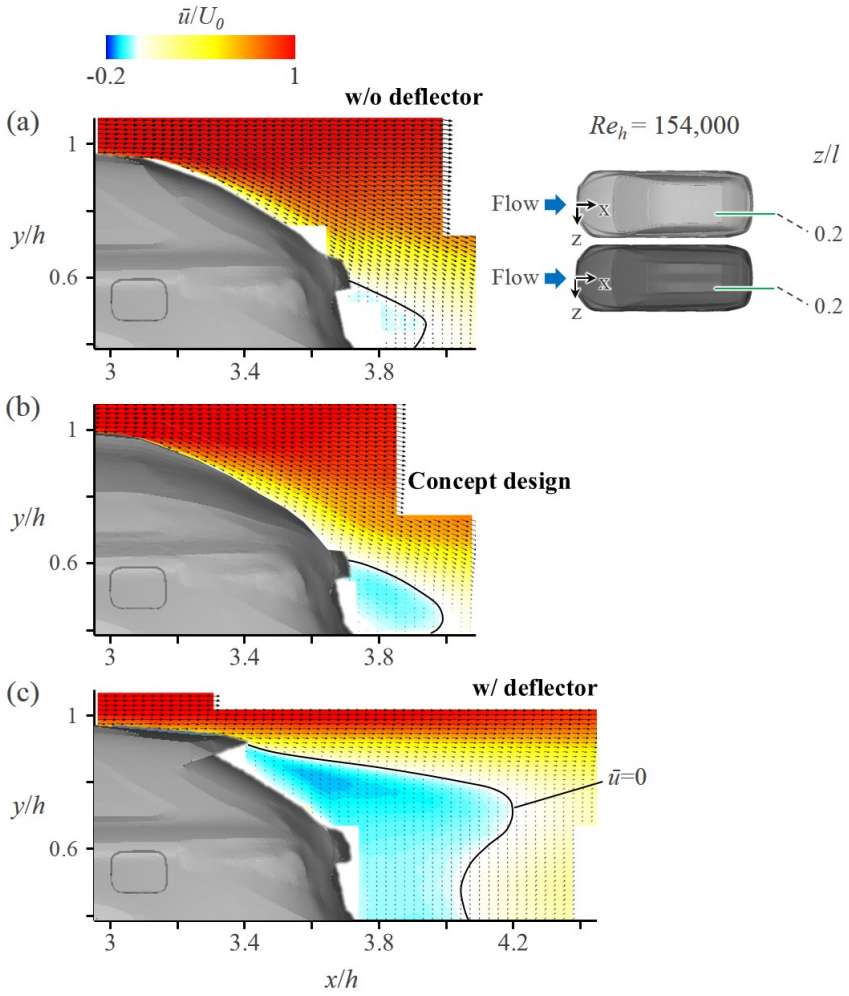

Figure 7.10. Contours of the time-averaged streamwise velocity ($\overline{u}$) and velocity vectors at z/h=0.2, Re=154,000 (γ=0°). Solid black lines in this figure indicate the locations of $\overline{u}$=0. (a) I40 model without deflector (no cnotrol); (b) Concept model (new design); (c) I40 model with deflector.

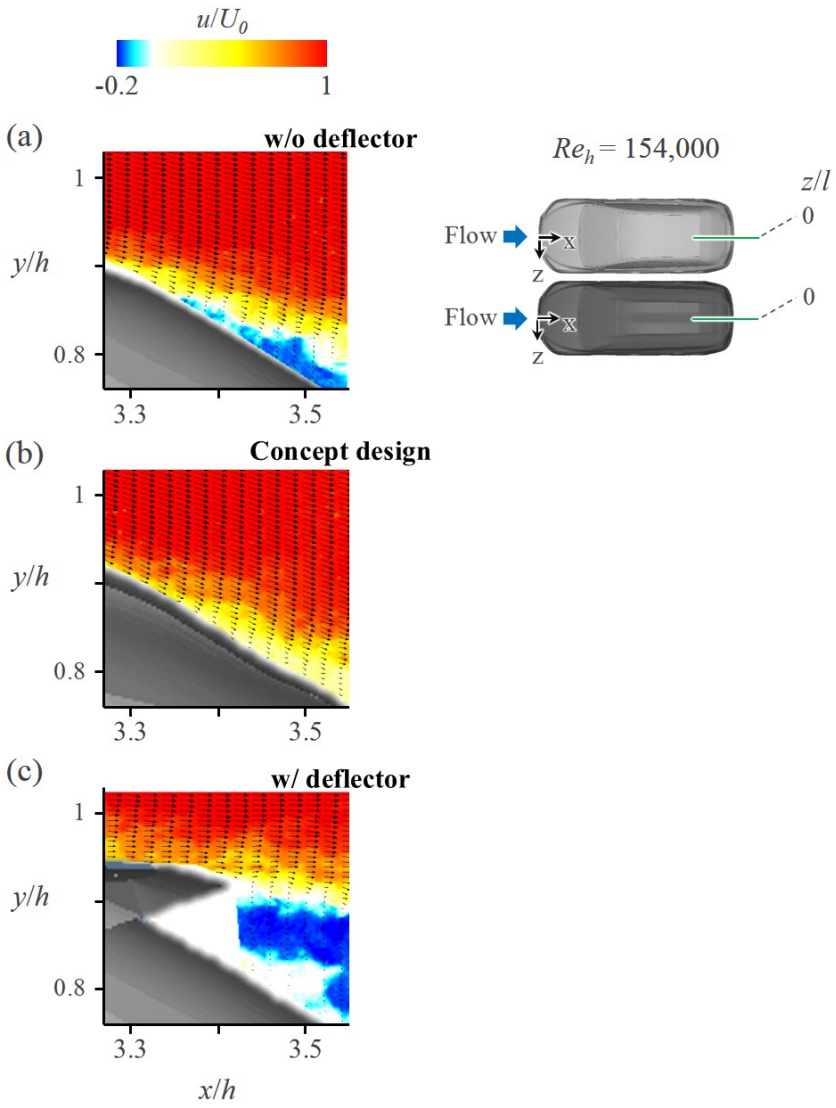

Figure 7.11. Contours of the instantaneous streamwise velocity (u) and velocity vectors at z/h=0, Re=154,000 (γ=0°). (a) I40 model without deflector (no cnotrol); (b) Concept model (new design); (c) I40 model with deflector.

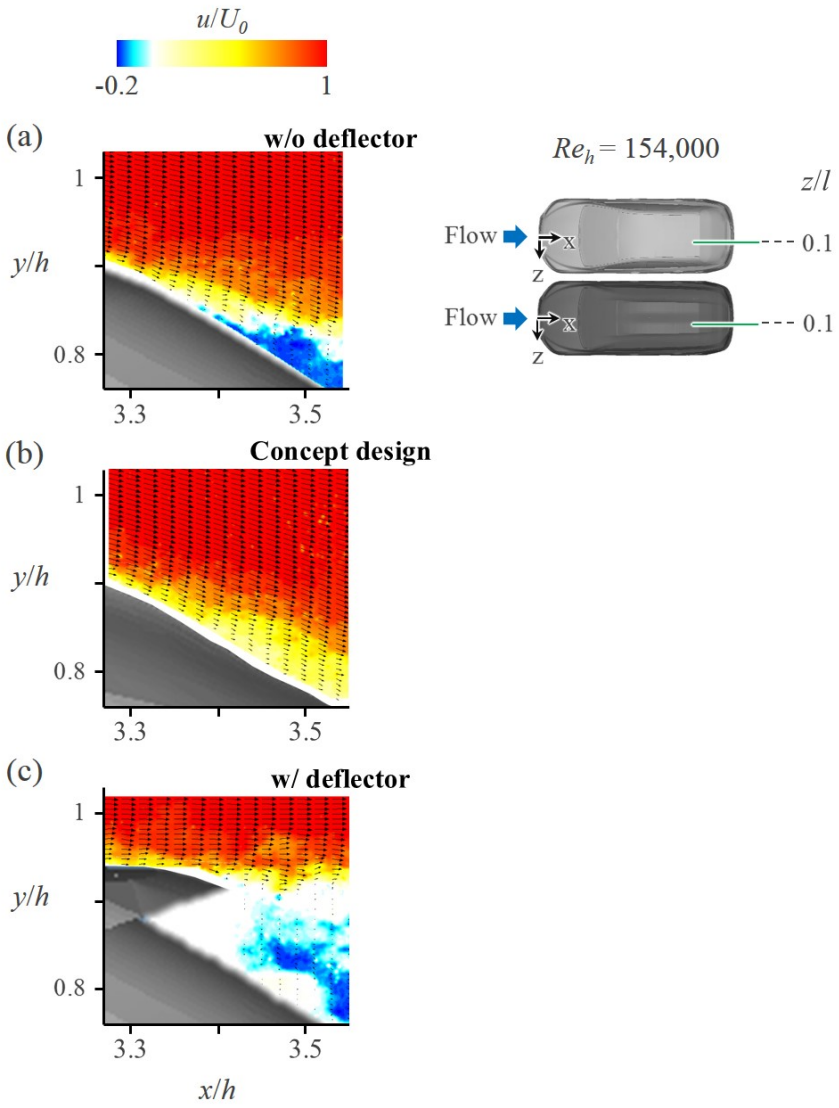

Figure 7.12. Contours of the instantaneous streamwise velocity (u) and velocity vectors at z/h=0.1, Re=154,000 (γ=0°). (a) I40 model without deflector (no cnotrol); (b) Concept model (new design); (c) I40 model with deflector.

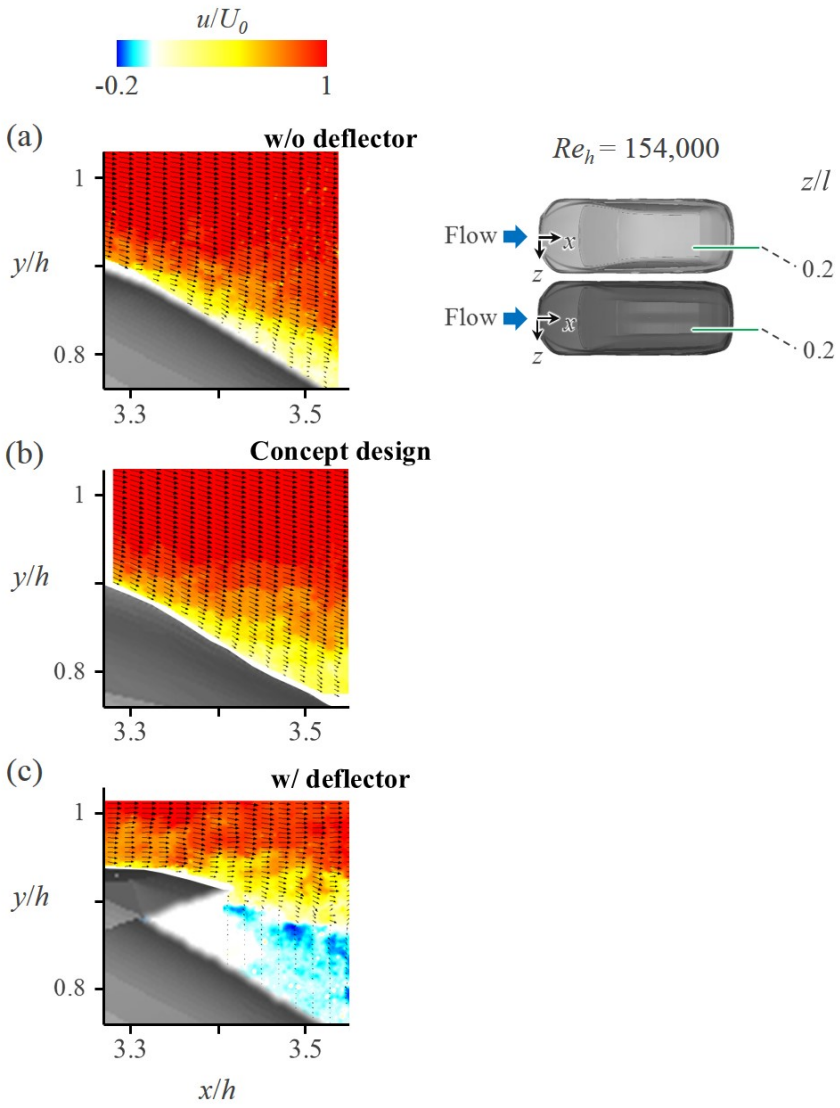

Figure 7.13. Contours of the instantaneous streamwise velocity (u) and velocity vectors at z/h=0.2, Re=154,000 (γ=0°). (a) I40 model without deflector (no cnotrol); (b) Concept model (new design); (c) I40 model with deflector.

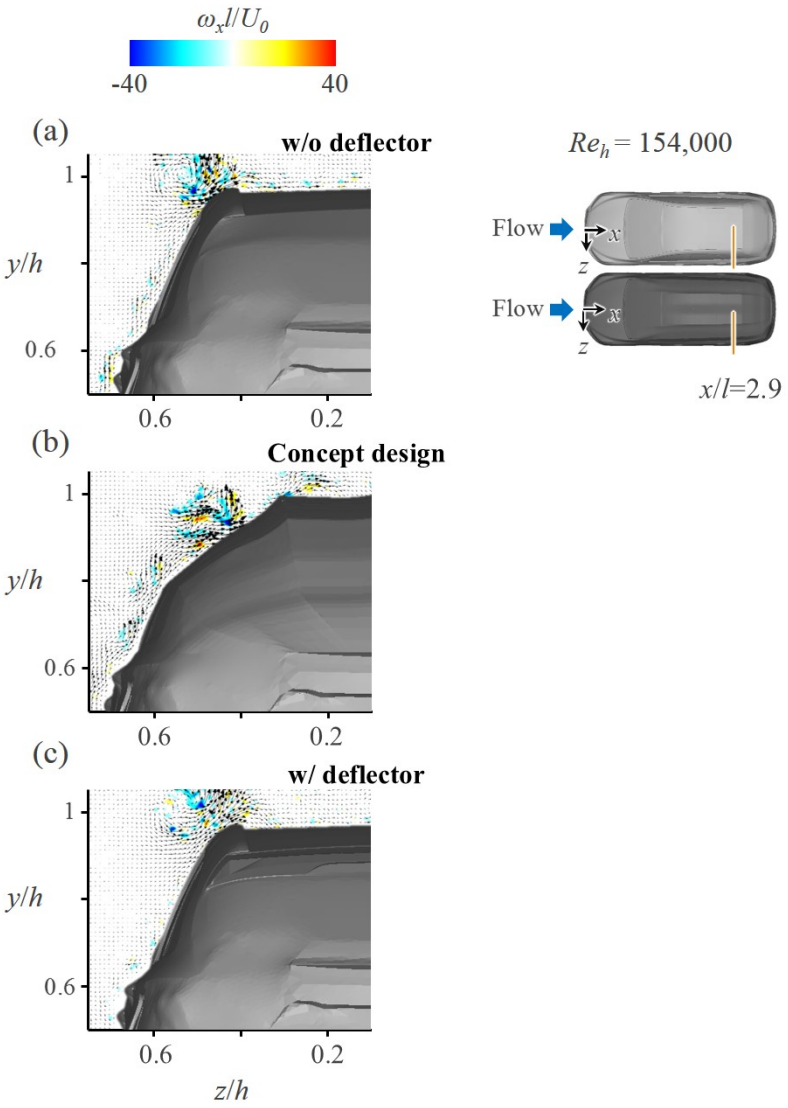

Figure 7.14. Contours of the instantaneous streamwise vorticity (ω_x) and velocity vectors at x/h=2.9, Re=154,000 (γ=0°). (a) I40 model without deflector (no cnotrol); (b) Concept model (new design); (c) I40 model with deflector.

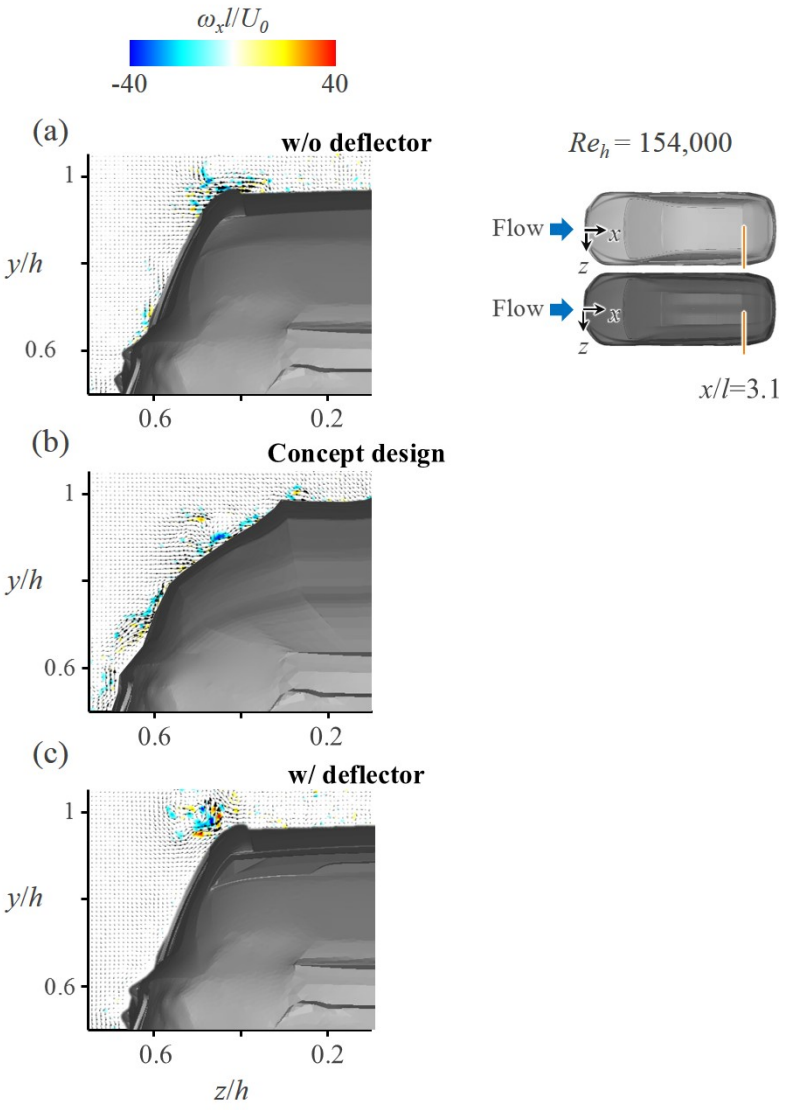

Figure 7.15. Contours of the instantaneous streamwise vorticity (ω_x) and velocity vectors at x/h=2.9, Re=154,000 (γ=0°). (a) I40 model without deflector (no cnotrol); (b) Concept model (new design); (c) I40 model with deflector.

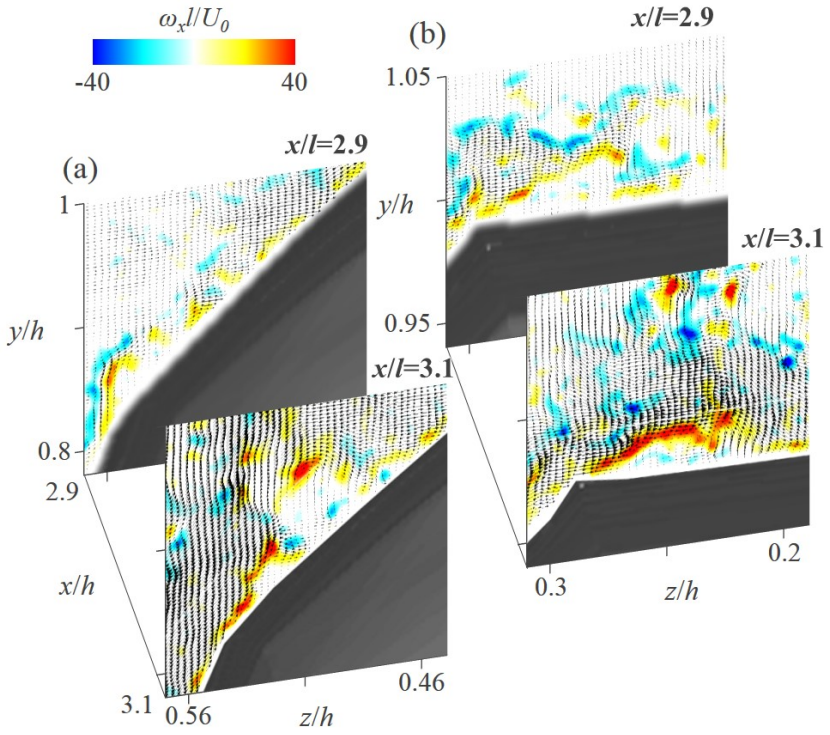

Figure 7.16. Contours of the instantaneous streamwise vorticity (ω_x) and velocity vectors on the concept model (new design) at two cross-flow planes (x/h=2.9, 3.1) with magnification (Re=154,000, γ=0°). (a) Flow-field near the second off-center ridge; (b) Flow-field near the first off-center ridge.

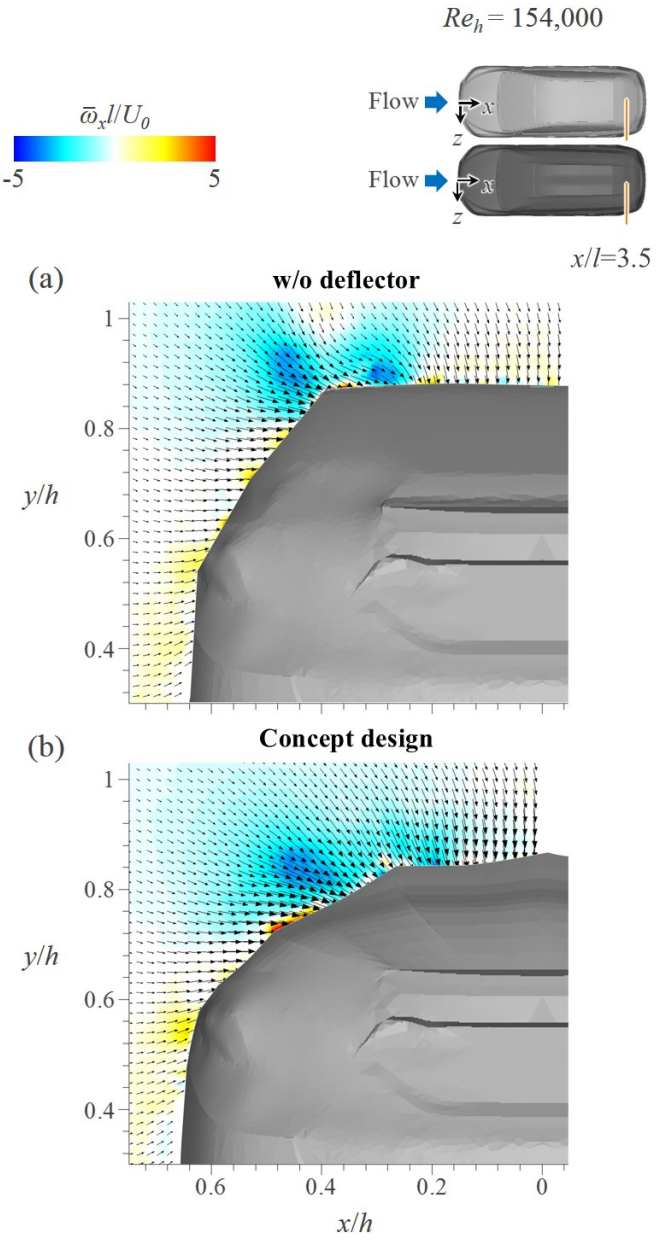

Figure 7.17. Contours of the time-averaged streamwise vorticity ($\overline{\omega_x}$) and velocity vectors at x/h=3.5, Re=154,000 (γ=0°). (a) I40 model without deflector (no cnotrol); (b) Concept model (new design).

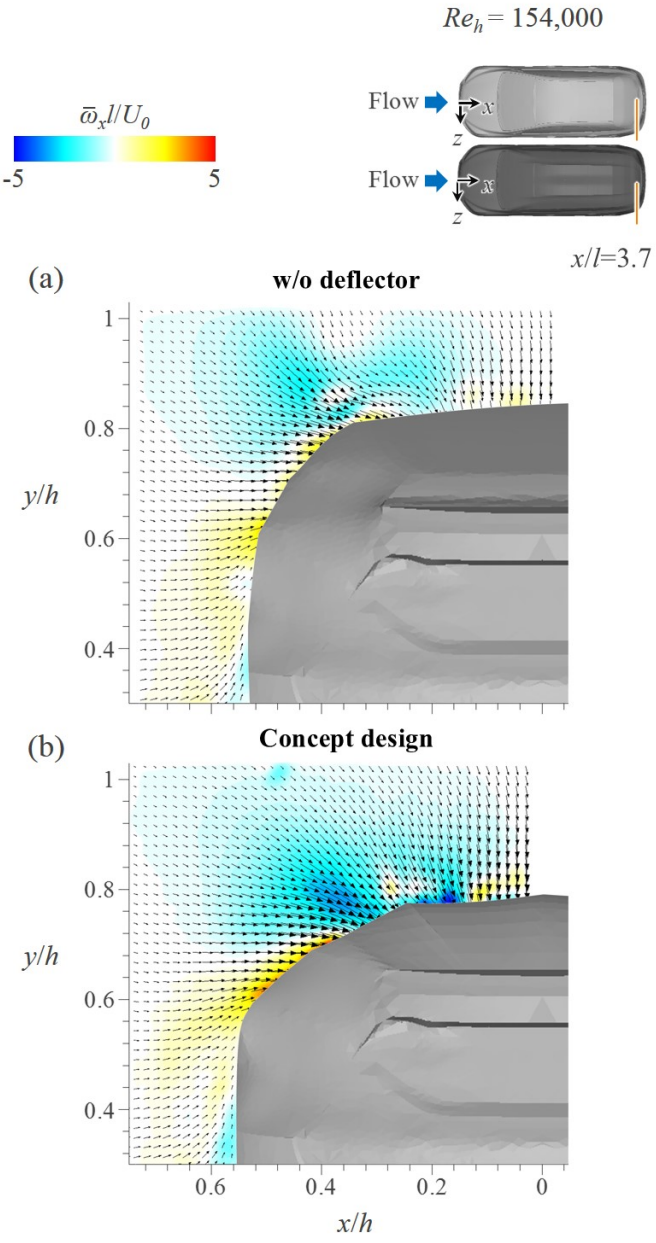

Figure 7.18. Contours of the time-averaged streamwise vorticity ($\overline{\omega_x}$) and velocity vectors at x/h=3.7, Re=154,000 (γ=0°). (a) I40 model without deflector (no cnotrol); (b) Concept model (new design).

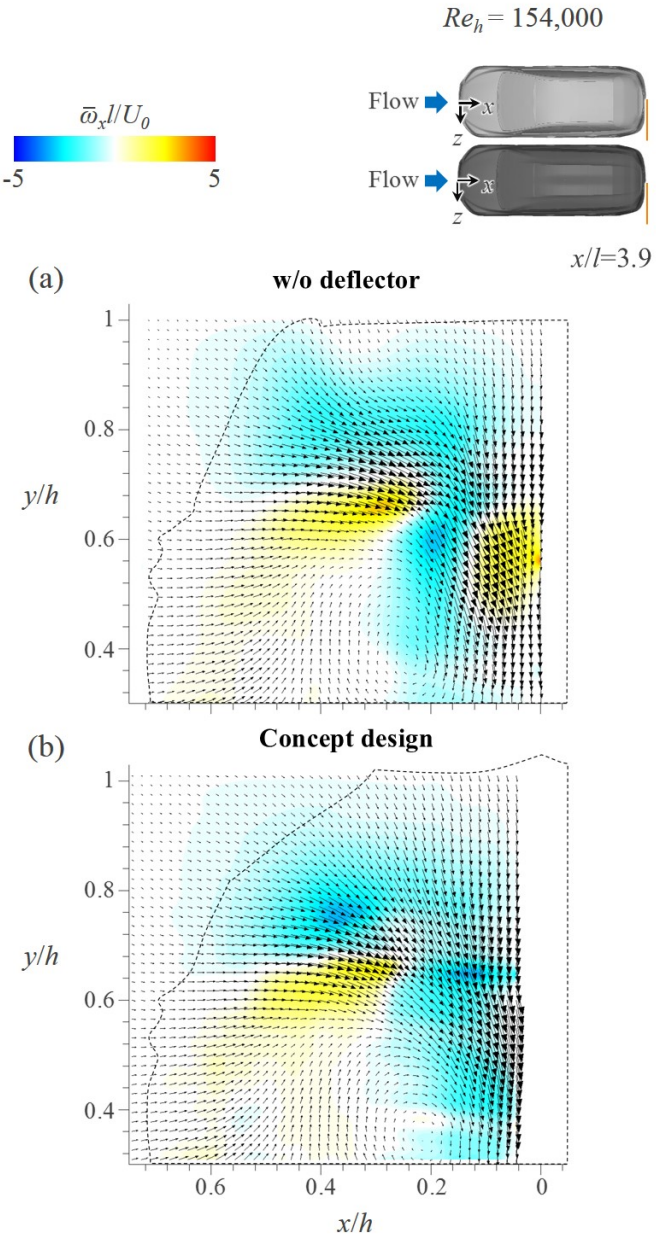

Figure 7.19. Contours of the time-averaged streamwise vorticity ($\overline{\omega_x}$) and velocity vectors at x/h=3.9, Re=154,000 (γ=0°). (a) I40 model without deflector (no cnotrol); (b) Concept model (new design).

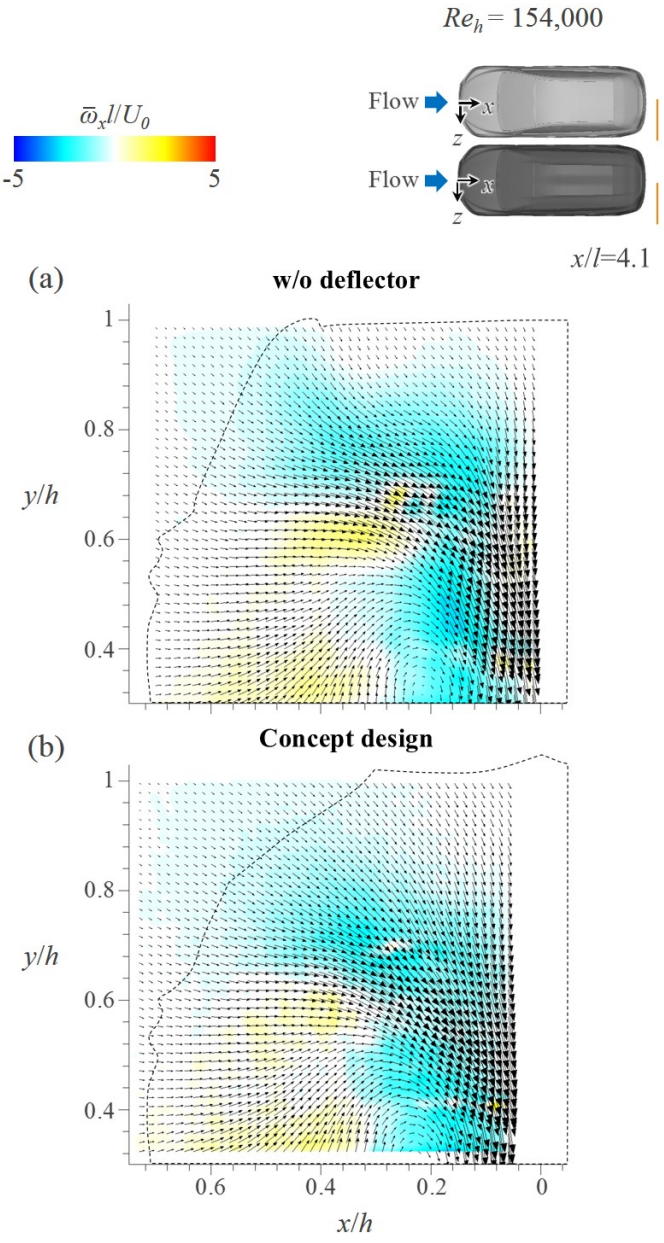

Figure 7.20. Contours of the time-averaged streamwise vorticity ($\overline{\omega_x}$) and velocity vectors at x/h=4.1, Re=154,000 (γ=0°). (a) I40 model without deflector (no cnotrol); (b) Concept model (new design).

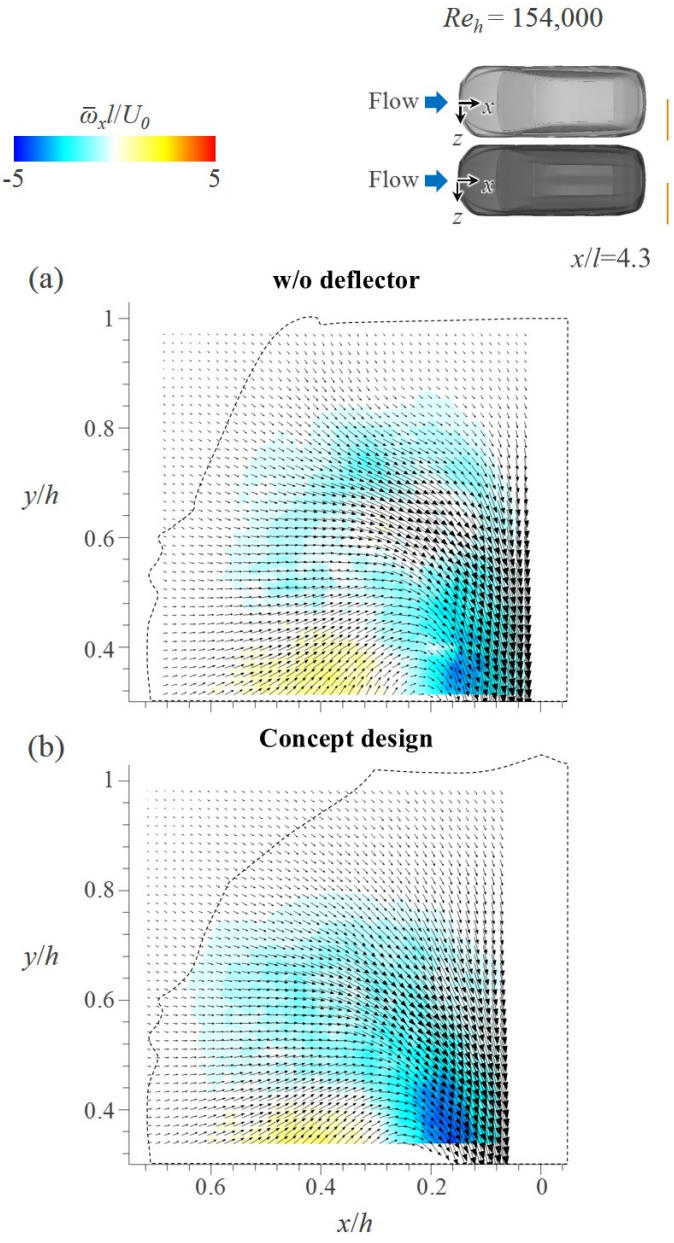

Figure 7.21. Contours of the time-averaged streamwise vorticity ($\overline{\omega_x}$) and velocity vectors at x/h=4.3, Re=154,000 (γ=0°). (a) I40 model without deflector (no cnotrol); (b) Concept model (new design).

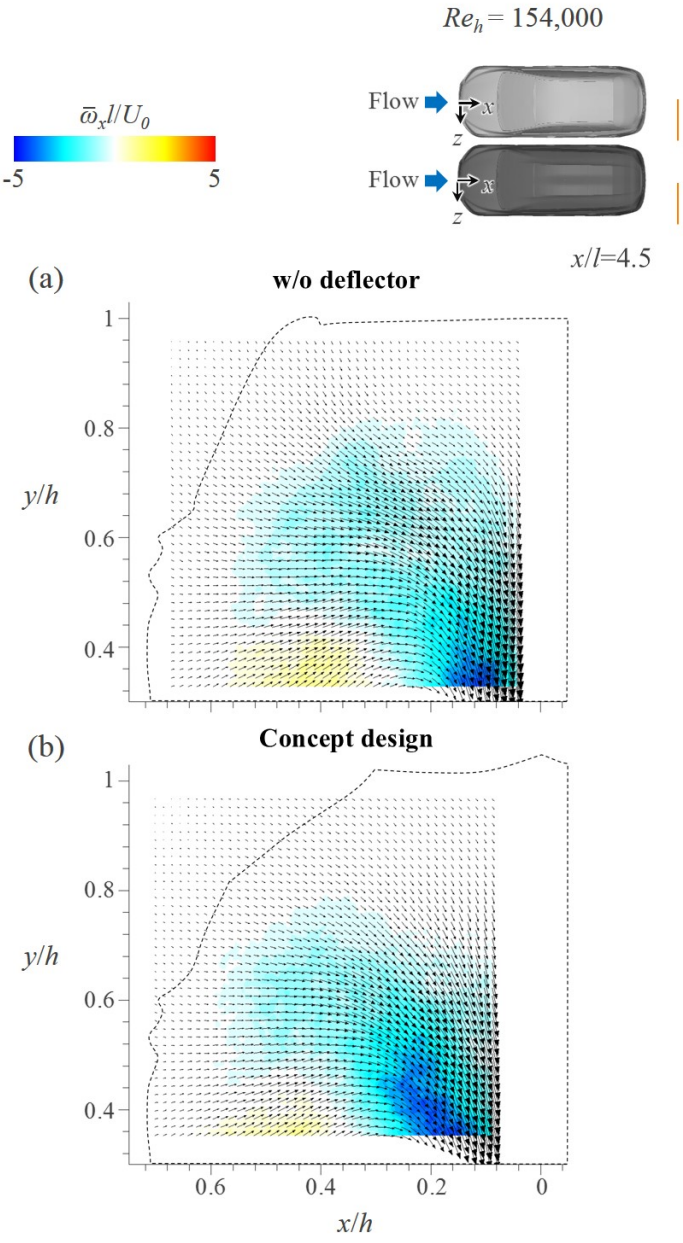

Figure 7.22. Contours of the time-averaged streamwise vorticity ($\overline{\omega_x}$) and velocity vectors at x/h=4.5, Re=154,000 (γ=0°). (a) I40 model without deflector (no cnotrol); (b) Concept model (new design).

Chapter 8

Summary and Concluding Remarks

In the present study, I have developed a newly-designed concept car model through bio-mimetic approach and evaluated the aerodynamic performances of the model through wind tunnel experiments. At zero yaw angle, the drag coefficient of the concept model showed lower value (5%) compared to that of the base model (I40, Hyundai motors). To understand the effect of a side wind on the aerodynamic characteristics of the model, I also considered non-zero yaw angles (γ=0°-30°) and measured the drag and side forces. At non-zero yaw angles, the drag and side forces on the concept model were both lower than those of the base model, and the drag and side force reduction rates were gradually increased with increment of the yaw angle. These results support that, unless the yaw angle is very large, the aerodynamic effects of the concept model in terms of drag and side force reduction are still similar to those of zero yaw angle.

To investigate the mechanism of drag reduction on the concept model, I conducted a flow visualization using oil-surface visualization and velocity measurement using DPIV, respectively. In the case of the base model, flow separation was occurred at the rear slanted surface of the model, resulting in the significant pressure drop at the slanted surface. On the other hand, in the case of the concept model, flow separation is almost suppressed and separation occurs only locally near the centerline of the slanted surface. Flow-field analysis on

cross-flow planes near the model surface showed that the ridges of the concept model generated streamwise vortices, which could supply higher momentum to the flow near the surface, might cause main separation delay. Therefore, this is the main reason of the drag reduction on the concept model which has the ridges on the surface.

References

Achenbach, E. 1974 The effects of surface roughness and tunnel blockage on the flow past spheres. *J. Fluid Mech.* **65**, 113–125.

Anders, J. B. 2000 Biomimetic flow control. AIAA Paper No. 2000-2543.

Bartol, I. K. *et al.* 2002 Flow patterns around the carapaces of rigid-bodied, multi-propulsor bixfishes. *Integ. Comp. Biol.* **42**, 971–980.

Bartol, I. K. *et al.* 2003 Hydrodynamic stability of swimming in ostraciid fishes: role of the carapace in the smooth trunkfish Lactophrys triqueter (Teleostei: Ostraciidae). *J. Exp. Biol.* **206**, 725–744.

Bartol, I. K., Gordon, M. S., Webb, P. W., Weihs, D. & Gharib, M. 2008 Evidence of self-correcting spiral flows in swimming boxfishes. *Bioinspir. Biomim.* **3**, 014001.

Bechert, D. W., Meyer, R. & Hage, W. 2000 Drag reduction of airfoils with miniflaps. Can we learn from dragonflies?. AIAA Paper No. 2000-2315.

Bjorndal, K. A., Bolten, A. B. & Chaloupka, M. Y. 2003 Survival probability estimates for immature green turtles *Chelonia mydas* in the Bahamas. *Mar. Ecol. Prog. Ser.* **252**, 273–281.

Block, B. A. *et al.* 2011 Tracking apex marine predator movements in a dynamic ocean. *Nature* **475**, 86–90.

Buchheim, R., Dobrzynski, W., Mankau, H. & Schwabe, D. 1982 Vehicle interior noise related to external aerodynamics. *Int. J. of Vehicle Design* **3**, 398–410.

Casey, J., Garner, J., Garner, S. & Williard, A. S. 2010 Diel foraging

behavior of gravid leatherback sea turtles in deep waters of the Caribbean Sea. *J. Exp. Biol.* **213**, 3961–3971.

Choi, H., Park, H., Sagong, W. & Lee, S. -I. 2012 Biomimetic flow control based on morphological features of living creatures. *Phys. Fluids* **24**, 121302.

Davenport, J. & Clough, W. 1986 Swimming and diving in young loggerhead sea turtles (*Caretta caretta* L.). *Copeia* **1986**, 53–57.

Davenport, J. 1987 Locomotion in hatchling leatherback turtles *Dermochelys coriacea*. *J. Zool.* **212**, 85–101.

Davenport, J., Munks, S. A. & Oxford, P. J. 1984 A comparison of the swimming of marine and freshwater turtles. *Proc. R. Soc. Lond.* B **220**, 447–475.

Davis, R. W. & Weihs, D. 2007 Locomotion in diving elephant seals: physical and physiological constraints. *Philos. Trans. R. Soc. London, Ser.* B **362**, 2141–2150.

Deraniyagala, P. E. P. 1936 Some postnatal changes in the leathery turtle, *Dermochelys coriacea*. *Ceylon J. Sci.* **19**, 225–239.

Eckert, S. A 2002 Swim speed and movement patterns of gravid leatherback sea turtles (*Dermochelys coriacea*) at St Croix, US Virgin Islands. *J. Exp. Biol.* **205**, 3689–3697.

Eckert, S. A., Eckert, K. L., Ponganis, P. & Kooyman, G. 1989 Diving and foraging behavior of leatherback sea turtles (*Dermochelys coriacea*). *Can. J. Zool.* **67**, 2834–2840.

El-Dessouky, H. T. & Ettouney, H. M. 2002 Fundamentals of salt water desalination. Elsevier.

Fish, F. E. & Lauder, G. V. 2006 Passive and active flow control by swimming fishes and mammals. *Annu. Rev. Fluid Mech.* **38**, 193–224.

Fossette, S. *et al.* 2010 Behaviour and buoyancy regulation in the deepest-diving reptile: the leatherback turtle. *J. Exp. Biol.* **213**, 4074–4083.

Hays, G. C., Houghton, J. D. R. & Myers, A. E. 2004 Endangered species: Pan-Atlantic leatherback turtle movements. *Nature* **429**, 522.

Hendrickson, J. R. 1980 The ecological strategies of sea turtles. *Am. Zool.* **20**, 597–608.

Hucho, W. H. & Sovran, G. 1993 Aerodynamics of road vehicles. *Ann. Rev. Fluid Mech.* **25**, 485–537.

Jones, T. T., Hastings, M. D., Bostrom, B. L., Pauly, D. & Jones, D. R. 2011 Growth of captive leatherback turtles, *Dermochelys coriacea*, with inferences on growth in the wild: Implications for population decline and recovery. *J. Exp. Mar. Biol. Ecol.* **399**, 84–92.

Keinath, J. A. & Musick, J. A. 1993 Movements and diving behavior of a leatherback turtle, *Dermochelys coriacea*. *Copeia* **1993**, 1010–1017.

Kerho, M., Hutcherson, S., Blackwelder, R. F. & Liebeck, R. H. 1993 Vortex generators used to control laminar separation bubbles. *J. Aircraft* **30**, 315–319.

Kim, D., Lee, H., Yi, W. & Choi, H. 2016 A bio-inspired device for drag reduction on a three-dimensional model vehicle. *Bioinspir. Biomim.* **11**, 026004.

Lee, S.-I., Kim, J., Park, H., Jaboski, P. G. & Choi, H. 2015 The function of the alula in avian flight. *Sci. Rep.* **5**, 9914.

Liebe, W. 1979 Der Auftrieb am Tragugel:Entstehung und Zusammenbruch. *Aerokurier* **12**, 1520-3.

Lissaman, P. B. S. 1983 Low-Reynolds-number airfoils. *Annu. Rev. Fluid Mech.* **15**, 223–239.

Lutcavage, M. E. & Lutz, P. L. 1996 in The Biology of Sea Turtles, Vol. 1 (eds Lutz, P. L. & Musick, J.) Ch. 10, 277-296. CRC Press.

Lutcavage, M. E., Bushnell, P. G. & Jones, D. R. 1992 Oxygen stores and aerobic metabolism in the leatherback sea turtle. *Can. J. Zool.* **70**, 348–351.

McCallen, R. *et al.* 1999 Progress in reducing aerodynamic drag for higher efficiency of heavy duty truck (class7-8). *SAE Technical Paper* 1999-01-2238.

Miklosovic, D. S., Murray, M. M., Howle, L. E. & Fish, F. E. 2004 Leading-edge tubercles delay stall on humpback whale (*Megaptera novaeangliae*) flippers. *Phys. Fluids* **16**, L39.

Oliver, L. J., Salmon, M., Wyneken, J., Hueter, R. & Cronin, T. W. 2000 Retinal anatomy of hatchling sea turtles: anatomical specializations and behavioral correlates. *Mar. Freshwater Behav. Physiol.* **33**, 233–248.

O'Meara, M. M. & Mueller, T. J. 1987 Laminar separation bubble characteristics on an airfoil at low Reynolds numbers. *AIAA J.* **25**, 1033–1041.

Pedro, H. T. & Kobayashi, M. H. 2008 Numerical study of stall delay on humpback whale flippers. *46th AIAA Aerospace Sciences Meeting and Exhibit*, 2008-0584.

Prange, H. D. 1976 Energetics of swimming of a sea turtle. *J. Exp. Biol.* **64**, 1–12.

Reina, R. D., Abernathy, K. J., Marshall, G. J. & Spotila, J. R. 2005 Respiratory frequency, dive behaviour and social interactions of

leatherback turtles, Dermochelys coriacea during the inter-nesting interval. *J. Exp. Mar. Biol. Ecol.* **316**, 1–16.

Renous, S., Bels, V. & Davenport, J. 2000 Locomotion in marine Chelonia: adaptation to the aquatic habitat. *Hist. Biol.* **14**, 1–13.

Salmon, M., Jones, T. T. & Horch, K. W. 2004 Ontogeny of diving and feeding behavior in juvenile seaturtles: leatherback seaturtles (*Dermochelys coriacea* L) and green seaturtles (*Chelonia mydas* L) in the Florida current. *J. Herpetol.* **38**, 36–43.

Shillinger, G. L. *et al.* 2011 Vertical and horizontal habitat preferences of post-nesting leatherback turtles in the South Pacific Ocean. *Mar. Ecol. Prog. Ser.* **422**, 275–289.

Watson, K. P. & Granger, R. A. 1998 Hydrodynamic effect of a satellite transmitter on a juvenile green turtle (*Chelonia mydas*). *J. Exp. Biol.* **201**, 2497–2505.

White, F. M. 2008 Fluid Mechanics. McGraw-Hill.

Wyneken, J. & Salmon, M. 1992 Frenzy and postfrenzy swimming activity in loggerhead, green, and leatherback hatchling sea turtles. *Copeia* **1992**, 478–484.

Wyneken, J. 1996 in The Biology of Sea Turtles, Vol. 1 (eds Lutz, P. L. & Musick, J. A.) Ch. 7, 165-198. CRC Press.

장수거북의 종방향 릿지:
유체역학적 역할과 컨셉카 디자인 응용

서울대학교 대학원
기계항공공학부
방경태

요 약

장수거북은 바다거북 중 가장 크고 빠른 거북으로 거북들 중 가장 뛰어난 유영능력을 가지고 있는 것으로 알려져 있다. 장수거북의 몸체를 보면 등갑 표면에 다른 바다거북의 등갑에는 존재하지 않는, 5개의 종방향 릿지가 있는 것을 볼 수 있는데, 종방향으로 등갑 전 영역에 분포하는 릿지의 형태적 특성 상 장수거북의 다양한 유영조건에 대응할 수 있는 유동제어 장치로서의 릿지의 유체역학적 역할을 예상할 수 있다. 따라서 본 연구의 1부에서는 장수거북의 종방향 릿지의 유체역학적 역할을 규명하고, 2부에서는 릿지의 형상을 바탕으로 낮은 공기저항을 갖는 새로운 컨셉카 디자인을 개발하는 것을 목적으로 하고 있다.

먼저 1부에서 실제 장수거북이 유영하는 조건에서 릿지의 유체역학적 역할에 대해 연구하기 위해 장수거북 박제를 스캔, 모델링하여 장수거북 모델을 제작하였으며, 이를 이용하여 풍동실험을 진행하였다. 그 결과 장수거북이 유영하는 조건에서 릿지가 모델의 유동저항을 최대 32% 감소시키는 것을 확인하였으며, 또한 장수거북이 호흡을 위해 수면으로 올라가는 경우에는 릿지가 장수거북의 양

력을 최대 16% 증대시키는 것을 확인하였다. 또한 입자영상유속계를 이용한 유동장 측정을 통해 이와 같은 유동제어 효과는 릿지에 의해 발생한 유선방향와류가 등갑 표면에서 유동박리 현상을 지연시킴에 의한 것임을 확인하였으며, 이는 등갑 표면 근처의 국지적인 유선 방향이 릿지의 돌출된 방향과 약간 어긋나면서 발생하는 현상임을 규명하였다.

2부에서는 장수거북의 형상 및 릿지의 유동제어 장치로서의 역할을 바탕으로 공기저항이 저감된 컨셉카 디자인을 개발하였다. 개발된 컨셉카 모델은 기존 모델 (현대자동차) 대비 공기저항이 약 5% 저감되었으며, 측풍에 의해 편주각이 30도까지 증가하는 경우에는 항력이 최대 약 13%, 그리고 측력이 최대 약 20% 저감되는 것을 확인하였다. 또한 입자영상유속계 및 표면 가시화를 이용한 유동장 분석을 통해 컨셉카 모델에 적용된 릿지 형상이 유선방향와류를 생성하여 모델 후면 경사면에서 유동박리를 억제하는 것을 확인하였다. 또한 종방향으로 형성된 릿지 형상에 의해 편주각이 크게 변하는 경우에도 릿지에 의한 유동제어 효과가 유지되는 것을 확인하였다.

주 요 어: 장수거북, 종방향 능선, 유선방향 와류, 생체모방 유동제어, 컨셉카, 양력, 항력

학 번: 2011-22888